Exosome Isolation: A Microfluidic TiO_2-Based Approach with Liposome Modeling

By

Zahra Motamedi

B.Sc., University of Tehran, Iran, 2021

A Thesis Submitted in Partial Fulfillment of the
Requirements for the Degree of

Master of Applied Science

in the Department of Mechanical Engineering

©Zahra Motamedi, 2023

University of Victoria

All rights reserved. This Thesis may not be reproduced in whole or in part, by photocopy or other means, without the permission of the author

Supervisory Committee

Exosome Isolation: A Microfluidic
TiO_2-Based Approach with Liposome Modeling

By

Zahra Motamedi

B.Sc., University of Tehran, Iran, 2021

Supervisory committee

Dr. Mina Hoorfar, Supervisor
Department of Mechanical Engineering

Dr. Stephanie Willerth, Departmental Member
Department of Mechanical Engineering,

Abstract

Exosome isolation is the first challenge for any exosome research, often limited by extended processing times, high costs, and potential impurities. In exosome isolations, preserving particle integrity, recovery, and size distribution is paramount for clinical applications. This study aims to overcome the limitations of conventional techniques by taking advantage of the specific affinity between titanium dioxide (TiO_2) particles and exosomal lipid bilayers. To emulate exosomes, liposomes with a size of 100 nm, composed of a mixture of 1,2-dioleoyl-sn-glycero-3-phosphocholine (DOPC) and cholesterol, were employed as exosome surrogates. These synthetic lipid vesicles closely replicate exosome attributes, rendering them suitable models for studying isolation methodologies due to their analogous size, density, and phospholipid bilayer composition. Using liposomes, which are more available and easier to work with, enables to explore the potential impact of our isolation method on exosome characteristics, offering insights into the adaptability of the developed approach for medical applications. We utilized TiO_2-based isolation for the attainment of efficient mixing and effective incubation with target particles to optimize their interaction. In assessing this methodology, we embraced two approaches: a conventional manual method and a microfluidic technique. We studied the effect of the incubation time and the amount of TiO_2 particles and the design and flowrate for the bulk and microfluidic approach respectively. A comprehensive evaluation incorporating dynamic light scattering (DLS), Zeta Potential Measurements, in conjunction with Fluorescence and Brightfield Imaging techniques, was conducted to carefully develop and evaluate the microfluidic TiO_2 based exosome isolation methodology using a liposome modeling. The analysis encompassed their effectiveness, recovery rates, and post-processed vesicle size distribution, affirming the method's reliability achieving capturing efficiency of 94.49% and recovery rate of 84.53%.

Table of Contents

List of Figures

List of Tables

Acknowledgements

I would like to express my sincere gratitude to my fellow lab mates for their invaluable support and help throughout my research journey. Their insights, discussions, and collaboration have been instrumental in shaping the direction of this work.

I extend my appreciation to my supervisor, Dr. Mina Hoorfar, for her encouragement, guidance, and for providing me with the opportunity to work in a field I am passionate about.

I am also thankful to Dr. Somayeh Fardindoost and Nishat Tasnim for their dedicated assistance and mentorship during this project. Their expertise and willingness to share their knowledge have been invaluable.

Dedication

I would like to dedicate my work to the passengers of flight PS752. Also, to all the people who have brutally been killed in the past 44 years and the ones who are still fighting for free Iran.

Chapter 1: Introduction

1.1 Exosomes and their significance in biomedicine

Exosomes are small membrane-bound vesicles with diameters ranging from 30 to 200 nanometers [1]–[4]. They belong to a larger family of extracellular vesicles, which includes microvesicles and apoptotic bodies, but exosomes stand out due to their unique composition and functions [5].

These vesicles were initially considered only carriers of cellular waste, responsible for transporting cellular debris. However, in 1983, Pan et al [6] identified a subtype of extracellular vesicles in sheep reticulocytes and named them exosomes [1]. Exosomes exhibit a distinctive cup-shaped or spherical morphology when observed under an electron microscope [7].

Exosomes are formed through a complex process involving the endosomal pathway[8]. It begins with the formation of early endosomes, which are derived from the inward budding of the cell membrane. These early endosomes then mature and develop into late endosomes, acquiring multiple depressions on their inner membrane, which enclose portions of the cytoplasm and various substances. These intraluminal vesicles (ILVs) are the building blocks of exosomes [9], [10].

Late endosomes with ILVs, known as multivesicular bodies (MVBs), have two possible fates: fusion with lysosomes for degradation or fusion with the cell membrane for secretion. The cholesterol content on MVBs is a critical factor determining this outcome [11]. When MVBs fuse with the cell membrane, they release their ILVs into the extracellular environment, and these vesicles are now designated as exosomes (Figure 1) [12].

1.1.1 Composition of exosomes

Exosomes not only carry a rich cargo of biological molecules, but also, they can maintain stability in bodily fluids even after the originating cells die, making them valuable in medical applications. Their contents reflect the nature of the cells they originate from, making them potential biomarkers for various diseases. Exosomes contain proteins, nucleic acids (RNA and DNA), and lipids (Figure 2).

Proteins: Exosomal proteins are a diverse group, and while some are common to all exosomes, others are cell-specific. Common proteins include those involved in membrane transport and fusion (Rab, GTPases, flotillin), synthesis of multivesicular bodies (Alix, TSG 101), tetraspanins (CD9, CD63, CD81, CD82), and cytoskeleton proteins (heat shock protein, actin, tubulin) [13], [14]. Specific proteins are derived from the cells of origin and can serve as diagnostic markers.

Lipids: Exosomes have a characteristic lipid bilayer composed of ceramide, cholesterol, sphingolipids, and phosphoglycerides. These lipids not only provide structural stability to exosomes but also make them promising candidates for drug delivery systems [15].

Nucleic Acids: Exosomes contain various nucleic acids, including DNA, messenger RNA (mRNA), microRNA (miRNA), and other non-coding RNAs. These nucleic acids can regulate gene expression and are indicative of the physiological state of the parent cells. They also have potential diagnostic and therapeutic applications [16], [17].

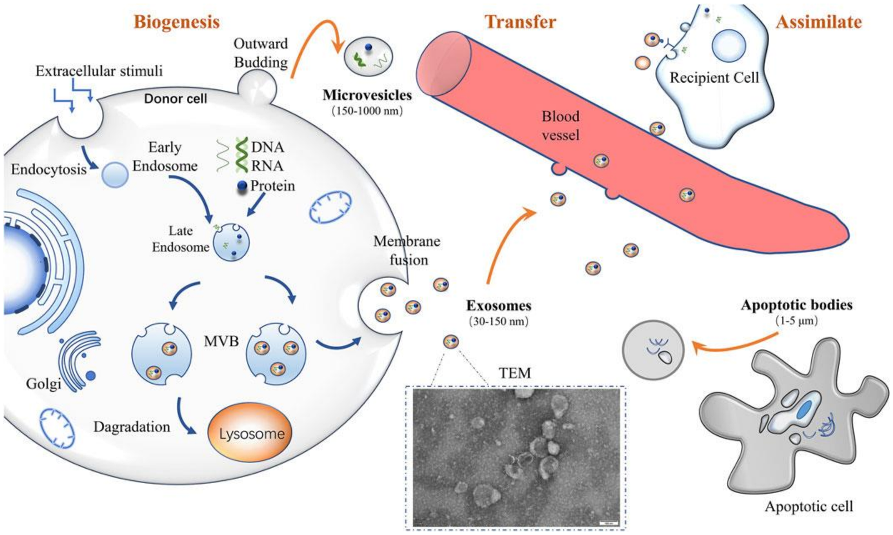

Figure 1- Biogenesis of exosomes and other vesicles, Reprinted with permission [18]

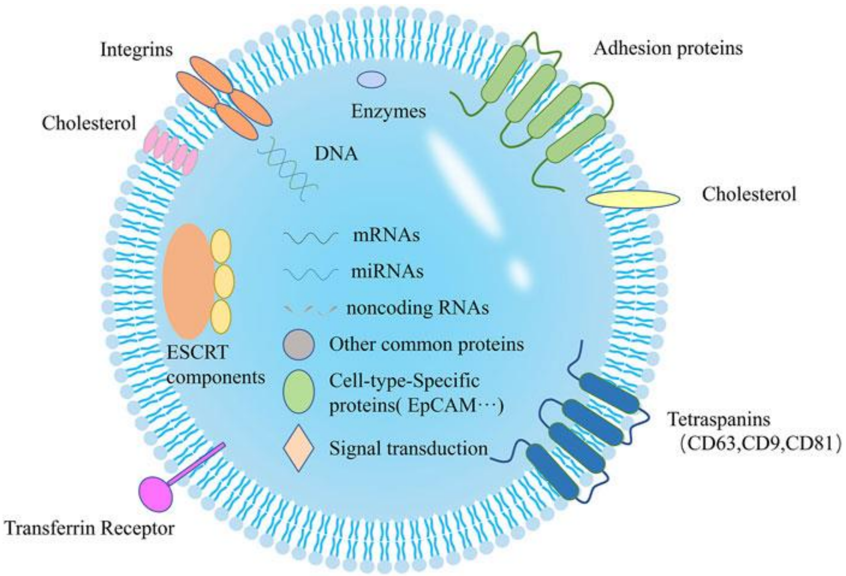

Figure 2- Schematic of exosomal molecular composition. Exosomes contain various important biomarkers, such as proteins, lipids, and miRNAs, Reprinted with permission [18]

1.1.2 Applications

1.1.2.1 Disease diagnosis

In the realm of medical diagnostics, exosomes have emerged as promising non-invasive or minimally invasive biomarkers for the early detection and prognosis of various diseases, most notably cancer. The potential of exosomes in this regard is rooted in their rich cargo of disease-specific biomolecules. They play pivotal roles in processes like the spread of tumor cells, facilitating the exchange of vital information among cells [19]. Moreover, exosomes have the ability to shield biomarkers, such as specific proteins and nucleic acids, from degradation in the harsh environment of bodily fluids [20]. This feature is invaluable for early disease detection, as it enables the preservation of crucial diagnostic indicators.

Building on this foundation, exosomal proteins have emerged as a novel approach in cancer diagnostics, demonstrating several potential advantages over traditional protein biomarker analysis with high level of false positive and negative results [21]. They are characterized by their stability within exosomes and a longer half-life, offering a more reliable alternative to traditional biomarkers that may degrade more rapidly. These proteins can directly influence target cells without the need for transcription or translation, providing a more immediate reflection of cancer cell states [22]. Advances in mass spectrometry-based detection technologies have enhanced the sensitivity and specificity of exosomal protein detection, offering more detailed insights into cancer pathogenesis. Furthermore, the ability to analyze posttranslational modifications in exosomal proteins using proteomic tools adds another layer of depth to cancer diagnostics, potentially surpassing the capabilities of traditional protein biomarker analysis [23]. These attributes position exosomal proteins as a promising tool in the early detection, diagnosis, and monitoring of cancer progression [24].

This diagnostic prowess extends to conditions such as cardiovascular diseases, tuberculosis, and central nervous system disorders [25]. In cardiovascular diseases, for example, specific exosomal microRNAs exhibit up-regulation in patients suffering from acute myocardial infarction and heart failure, making them valuable diagnostic markers[26], [27]. Based on diagnostic testsconducted using exosomes from Dysferlinopathy patients' serum and urine, it was found that Dysferlin was missing in these exosomes, providing a distinct marker for diagnosing Dysferlinopathy [28]. Additionally, in central nervous system diseases, the expression levels of specific molecules in exosomes vary, suggesting their potential as diagnostic markers [29]. These molecules include miR-21, isolated using a sucrose gradient [30]; miR-29 and miR-219, both isolated through ultracentrifugation methods [31], [32]; LRP6, extracted using a commercial reagent (ExoQuick) and immunochemical enrichment [33]; and caveolin1, also isolated via ultracentrifugation [34]. This variation in expression levels highlights their diagnostic significance for these conditions.

Liquid biopsy, a minimally invasive technique for sampling tumors, leverages tumor-derived exosomes to detect biomarkers closely associated with cancer. For instance, exosomal proteins like CD151 have shown significantly elevated expression in lung cancer patients. Additionally, specific miRNAs are highly enriched in exosomes derived from breast cancer cells. These markers contribute to the heightened specificity and sensitivity of early cancer diagnosis, establishing liquid biopsy as a promising approach for detecting tumors [35]–[37].

1.1.2.2 Drug delivery

Another application of exosomes is drug delivery with a promising future. Their small size enables them to bypass immune responses and navigate biological barriers efficiently[38]. With natural compatibility and low immunogenicity, exosomes transport various therapeutics, including Western medicines like doxorubicin for brain tumors, antioxidants like catalase for neurodegenerative diseases, and traditional Chinese medicines for anti-inflammatory and anti-cancer effects [39], [40]. They also deliver gene therapy agents, such as oligonucleotides, targeting disease-causing genes in conditions like Huntington's disease and neurodegenerative disorders

[41]. Exosomes offer a versatile and effective platform for precise drug delivery, enhancing treatment outcomes across a range of medical challenges.

1.2 Conventional exosome isolation methodologies

As mentioned earlier, exosomes, small vesicles ranging from 30 to 150 nm in size, have emerged as crucial players in early disease detection and therapeutic applications due to their unique ability to carry biomolecules and signaling molecules. However, isolating exosomes from complex biological fluids is a difficult challenge owing to their heterogeneity in size, content, function, and source, low density and the presence of similar components, such as cell fragments and proteins, that coexist with them [42], [43]. Most current isolation technologies struggle to completely separate exosomes from lipoproteins and extracellular vesicles with similar biophysical characteristics, leading to low exosomal purity. Additionally, the biological activity of exosomes can be significantly impacted by the isolation techniques employed [44]. Therefore, standardized and efficient methods for exosome separation and quantification are pivotal for advancing exosome research and its clinical applications. In the following paragraphs we will cover some conventional methodologies in the world of exosome isolation.

Ultracentrifugation

Ultracentrifugation is the most widely used technique for exosome separation. It relies on differences in density and size to separate exosomes from other components in the sample. The technique involves a series of centrifugation steps, starting with low-speed centrifugation to remove larger cells and debris, followed by high-speed ultracentrifugation to pellet exosomes. Despite its maturity and cost-effectiveness, ultracentrifugation has several drawbacks [45]. The entire separation process is time-consuming, taking more than four hours to complete.

Furthermore, repeatability is often poor and unstable. Impurities, including co-purifying protein aggregates and subcellular organelles, may persist even after several rounds of centrifugation. Most concerning, high-speed centrifugation may damage exosomes, compromising their biological activity [46], [47].

Density Gradient Centrifugation

Density gradient centrifugation is an improvement over standard ultracentrifugation. Density gradient centrifugation for exosome isolation is a technique that separates exosomes from other cellular components based on their distinct densities. A sucrose gradient is created in a centrifuge tube, with varying densities from top to bottom. When a sample containing exosomes is layered on this gradient and centrifuged, the exosomes migrate through the gradient until they reach a point where their density matches that of the gradient. This results in exosomes settling into a specific layer, which can then be isolated. This method effectively separates exosomes from other cellular materials, as it relies on the inherent physical property of density, allowing for relatively pure exosome preparation [48]. However, this method requires extensive preparation, involves complex operations, and has longer centrifugation times, often exceeding 16 hours, limiting its clinical applicability [49], [50].

Ultrafiltration

Ultrafiltration, based on molecular size, is a straightforward method for exosome separation. It relies on one or more filtering membranes with specific molecular weight cut-offs (MWCO) to retain larger contaminants while allowing exosomes to pass through [51]. While efficient for large sample volumes, ultrafiltration can be time-consuming (approximately 150 minutes), and certain implementations, like electric charge-based ultrafiltration, may require additional kits and may not be ideal for processing blood samples [52].

Size-Exclusion Chromatography

Size-exclusion chromatography (SEC) separates exosomes based on molecular size using porous beads. Unlike ultracentrifugation, SEC maintains exosomal biological function, making it appealing for studying exosome functionality. However, it relies on gravity or low-speed centrifugation, which may not efficiently isolate exosomes compared to ultracentrifugation. Combining SEC with other techniques, such as ultracentrifugation or ultrafiltration, can improve exosome purity [53].

Immunoaffinity

Immunoaffinity techniques leverage specific antigen-antibody interactions to isolate exosomes. By targeting exosomal surface proteins, such as tetraspanins or disease-specific markers such as CD63, CD81, and CD9, this method achieves high isolation purity [54]. However, it is time-consuming due to the need for antibody binding and can be costly with strict reagent and storage requirements [46]. Researchers who do not require high purity or specific exosome subclasses may find this method not ideal.

Polymer Precipitation

Polymer precipitation methods, particularly those using polyethylene glycol (PEG), have gained popularity for their simplicity and handling large samples. PEG reduces exosomal solubility, enabling easy precipitation via low-speed centrifugation. However, they are prone to contamination by lipoproteins or virus particles, which can affect downstream analyses [55]. Researchers often combine polymer precipitation with other techniques to mitigate these drawbacks which causes a more complex process.

Exosome Separation Kits

Commercial exosome separation kits offer convenience and accessibility but vary significantly in terms of exosome purity, quantity, and size distribution. It should be carefully select a kit based on the experimental goals. These kits tend to be expensive and may not be suitable for processing large sample volumes [56].

1.3 Membrane-based isolation as a novel strategy, review of bulk TiO_2 publications and motivation for microfluidic approach

Exosomes are small vesicles secreted by cells, and they are enclosed by a lipid bilayer membrane. This lipid bilayer is composed of phospholipids, which are inherently amphiphilic molecules. The hydrophilic portion of the phospholipids faces the aqueous (water-based) environment both inside and outside the vesicle, while the hydrophobic tails of the phospholipids are oriented toward the interior of the lipid bilayer, away from water. This amphiphilic property of the lipid bilayer allows exosomes to form stable vesicles in aqueous solutions and transport hydrophilic and hydrophobic molecules within their structure. It's a fundamental feature that enables exosomes to function as carriers for various biomolecules and to participate in cell-to-cell communication [57].

The lipid bilayer of exosomes is rich in a specific type of phospholipid called phosphatidylserine. This molecule has a negatively charged phosphate group in its head region, which is exposed on the outer surface of the bilayer [58]. The exposed phosphate groups play a crucial role in the specific binding to metal oxides, including TiO_2 [58]–[63] and zirconium oxide (ZrO2) [64]. among membrane based methodologies TiO_2 based ones have shown the best results.

Gao et al. aimed to investigate the mechanisms involved in the process of exosome adsorption onto TiO_2 particles. To do so, two kinetic models: the pseudo-first order equation and the pseudo-second order equation are considered [58]. These equations describe the rate at which exosomes adhere to TiO_2 particles over time.

Pseudo-First Order Equation (Equation 1 and 2) suggests that the rate of exosome adsorption is proportional to the difference between the equilibrium adsorption capacity (q_e) and the amount of exosomes adsorbed at any given time (q_t).

$$dq_t/_{dt} = k_1(q_e - q_t) \tag{1}$$

$$\ln(q_e - q_t) = \ln q_e - k_1 t \tag{2}$$

Pseudo-Second Order Equation (Equation 3 and 4) proposes that the rate of exosome adsorption is proportional to the square of the difference between q_e and q_t.

$$dq_t/_{dt} = 2(q_e - q_t)^2 \tag{3}$$

$$\frac{1}{(q_e - q_t)} = \frac{1}{q_e} + 2t \tag{4}$$

By performing experiments with different amounts of TiO_2 particles and various incubation times to determine and comparing the experimental data with the theoretical values calculated using each model, they found that the pseudo-second order model provided a better fit to the data (higher linear correlation coefficient, r2) and best described the exosome adsorption process onto TiO_2, indicating that a chemical-specific adsorption mechanism was at play, suggesting a strong binding between the phosphate groups in the exosome's phospholipid bilayer and the TiO_2 surface. It has also been shown that variations in sizes, crystal forms, and surface roughness does not significantly affect the isolation.

Eventually by optimizing the two main determining factors, the amount of $\mathrm{TiO_2}$ and the incubation time, they achieved a maximum efficiency of 93.4% with 2 mg and 10 minutes incubation time for $50\ \mu l$ of sample consisting of $2\ \mu g$ of exosomes [58]. In the Table 1 we can see a comparison of this innovative approach with previously mentioned conventional methodologies.

Table 1 - Comparison of exosome isolation methodologies

Methodology	Principle	Benefits	Disadvantages	Reference
Ultracentrifugation	Components with different size and density possess various sediment speed	Gold standard, affordable, appropriate for large-volume samples	Time-consuming (> 4 h), complicated process, low yield, may damage exosomes	[45]
Density Gradient	Particles in a density gradient migrate until their density matches the surrounding medium	High purity, avoiding exosomal damage	Time consuming (> 16 h) labor-intensive, preliminary preparation and complex operation, low yield	[48]
Ultrafiltration	Particles with various size and molecular weight	East, without specialized tools or materials	Time consuming (> 2 h),	[52]

			clogging on filtering membrane, loss of small exosomes	
SEC (Size Exclusion Chromatography)	Particles with various size and molecular weight	Simple, affordable, and effectively preserve the structure and function of biology, high purity	Time consuming (1-2 h), special columns and packing are required, lipoprotein contamination, low yield	[53]
Immunoaffinity	Based on interaction between antibodies and specific membrane proteins of exosomes	High specificity for isolating exosome subtypes, high purity	Time consuming (> 4 h), Expensive, complicated, depending on specificity of the antibody	[54]
Polymer precipitation	The influence of exosomal the solubility or dispersibility under	Easy to use and appropriate for huge quantities of samples	Potential contaminants (co-purifying protein	[55]

	the high hydrophilic polymers		aggregates or residuary polymers), low purity	
Exosome separation kits	Various principles depending on the kit (e.g., immunoaffinity, size exclusion)	Convenient, pre-optimized protocols	Can be expensive, potential for batch-to-batch variability, low purity	[52]
TiO_2 based	Affinity of TiO2 particles and the phosphate groups on the surface of exosomal lipid membranes	Low assay time, ease of use, relative high purity, high yield	Non-specificity	[58]

Building on the findings of the previously discussed study, several other publications have explored $\mathrm{TiO_2}$-based exosome isolation in more detail.

Pang and Shi developed a method for capturing and analyzing exosomal PD-L1 from serum, which could serve as a predictor for responses to anti-PD-1/PD-L1 therapy [61]. They utilized Fe3O4@$\mathrm{TiO_2}$ nanoparticles to enrich exosomes within 5 minutes, achieving a capture efficiency of 96.5%. Anti-PD-L1 antibody-modified Au@Ag@MBA SERS tags were used for quantification.

A hydrophilic probe is employed in Li et al. work, to enrich exosomes from different cancer cells by exploiting $\mathrm{TiO_2}$-phosphate interactions and hydrophilic interactions with exosomal glycoproteins. This dual-affinity probe separated exosomes and glycopeptides, allowing the identification of N-glycoproteins in exosomes from various cell types [62]. These glycoproteins distinguished exosomes from different sources and their potential roles in different signaling pathways.

Urine is another biofluid that has been used for $\mathrm{TiO_2}$-based exosome isolation in several studies offering a noninvasive and convenient method. It is worth mentioning that isolation methodologies for urine samples can be a challenging task and they usually do not offer high capturing efficiency due to the fact that the concentration of exosomes in urine is significantly less than in serum[65]. On average, around $1-3 \times 10^{12}$ exosomes were extracted from 1 ml of serum, whereas about $3-8 \times 10^{9}$ exosomes were obtained from 1 ml of urine[65].

An approach called ultrafiltration–$\mathrm{TiO_2}$ was introduced in [60]. It addressed the challenge of isolating urinary exosomes, caused by low concentration of exosomes in this type of samples, quickly and efficiently. They introduced a strategy based on ultrafiltration and the specific interaction of TiO_2 with exosome lipid bilayers, resulting in the capture of 91.5% intact exosomes within 20 minutes. LC-MS analysis identified 1874 protein groups, which was 23% higher than conventional methods validating higher intactness of particles achieved by TiO_2 based isolation compared to conventional methods. However, the additional step of ultrafiltration might be considered less straightforward and more time-consuming, with 10 minutes increase in time compared to [66].

In [59], they developed a novel material called Fe3O4@TiO_2-CD63 aptamer, designed for rapid exosome isolation. This material relies on double interactions with TiO_2 and aptamers specific to exosome proteins. With an assay time of 10 minutes, they achieved a capture rate of 92.6% intact exosomes from urine. but may be costlier, less specific, and less readily applicable. Complex aptamer synthesis and complicate the process and

Although Using Fe3O4@TiO_2-CD63 aptamers for exosome isolation offers relative speed and efficiency, with a urine sample possessing low concentration of exosomes, the complex, costly and time consuming (over 50h) synthesis of Fe3O4@TiO_2-CD63 aptamer on one side and potential off-target binding could make it a less applicable approach [61]. Besides, using affinity for specific proteins on the surface of extracellular vesicles (EVs) limit its wide-ranging utility and broad EV studies; because it can lead to unreliable analysis results if EVs lacking the targeted proteins are excluded [67].

Lou et al. proposed a method combining ultrafiltration (UF) and phospholipid affinity to collect high-purity EVs from a 30 mL urine sample. This method isolated more than 10^10 EV particles and maintained the typical characteristics of EVs. Comparing this method to the gold standard of ultracentrifugation (UC), they found it comparable in terms of EV quality and the number of identified metabolites [63].

Comparing the use of TiO_2 in the isolation of exosomes to traditional methods such as ultracentrifugation and coprecipitation kits, TiO_2-based methodology is stated to yield a higher number of protein groups identified in the exosomes, suggesting a more efficient isolation method with higher purity. Moreover, it shows an improved enrichment of exosome markers, a reduction in non-specific protein adsorption and the reliability of the strategy to preserve the chemical properties and cargos of the vesicles [58]–[63]. A more comprehensive comparison is shown in the Table.

Despite the promising interaction between TiO_2 and exosomes, most studies on TiO_2-based exosome isolation have been conducted using bulk experiments. In contrast, microfluidic devices have emerged as an effective platform to overcome the limitations of conventional isolation methods [68]. There has been many studies investigating the effect of employing microfluidic systems, specifically micromixers, compared to conventional methods of bulk mixing such as using shakers in many areas of studies. In [69] a microfluidic system utilizing a four-membrane-type micromixer is introduced for rapid serological analysis of dengue virus antibodies. This micromixer significantly outperformed traditional large-scale shakers. It achieved a saturated fluorescent intensity in just 20 minutes, while shakers took over 40 minutes. Furthermore, the microfluidic system substantially reduced incubation times for critical steps: mixing virus-bound magnetic beads with serum samples took only 5 minutes, and mixing immunoglobulin-bound bead complexes with antibodies was shortened to 2 minutes. As a result, the entire diagnostic protocol, which would traditionally take over 4 hours using ELISA, was condensed to a mere 30 minutes using the micromixer, offering significant promise for detecting dengue and other infectious diseases. Taking advantage of micromixers has also shown great improvement even in the field of chemical engineering. [70] emphasizes the potential of micromixers as effective tools for metal extraction, presenting a marked improvement over conventional techniques It has been shown that using an interdigital micromixer substantially improved the extraction and separation of copper from its impurity elements, iron and zinc, compared to conventional shaker-based methods. Notably, the micromixer achieved a remarkable 99% extraction efficiency for copper in just a single stage. In contrast, the traditional batch extraction required two stages to attain similar efficiency. Even more impressive was the extremely short residence time of 1.6 seconds in the micromixer, at which an 84.05% copper extraction efficiency was realized. The traditional method lagged, reaching only 77.72% extraction at a much longer residence time of 60 seconds. Additionally, the micromixer exhibited enhanced separation factors, significantly outperforming the batch extraction.

Microfluidics allows for precise control and manipulation of fluids within microscale channels, leading to reduced sample and reagent consumption, improved detection sensitivity, and integration of multi-functional operations onto a single chip. On the other hand, they offer precise control over fluid flow and are able to do manipulation at the microscale. In biomedical applications, including exosome isolation, the methodologies employed must be gentle to protect the integrity of delicate samples and maintain accuracy. At the same time, achieving optimal performance, such as efficient mixing, is essential. This dual need suggests that micromixers might be a potentially superior choice over manual mixing.

1.4 Adopting microfluidic approach

Mixing in microscale is challenging due to the dominance of viscous forces and molecular diffusion over convective flow. In small channels, laminar flow dominates, limiting the natural chaotic mixing seen in macroscale systems. This slow mixing can obstruct reaction efficiency and uniformity. Consequently, special designs are necessary to overcome these hurdles. Innovative microscale mixers often employ chaotic advection, hydrodynamic focusing, or geometric structures to enhance mixing efficiency. These designs exploit the unique fluid behavior at the microscale, promoting molecular diffusion and ensuring uniform mixing, enabling advancements in fields like pharmaceuticals, lab-on-a-chip devices, and chemical synthesis [71], [72].

Microfluidic devices based on type of control or driving force they use can be divided into two categories: passive and active devices. Active microfluidic devices use external energy sources for mixing, separation, etc. In contract, passive micromixers utilize inherent fluidic properties, such as diffusion and convection and channel geometry, to facilitate mixing without the need for external energy sources or actuators, making them suitable for applications where simplicity and low power consumption are critical considerations [73].

Active Micromixers:

Active micromixers differ from their passive counterparts by exploiting external energy sources to disrupt laminar flow inducing chaotic advection, increase contact areas between fluids [73], [74].

The foundation for micromixers driven by acoustic fields lies in the disruption of micro streams caused by acoustic waves. Various technologies have been employed to achieve this, including ultrasonic transducers, thin-film piezoelectric devices, and surface acoustic waves that propagate along the surface of a solid. One notable example is the work of Luong et al [75], who deposited focused interdigitated electrodes on a piezoelectric substrate to generate surface acoustic waves, resulting in the concentration of acoustic energy.

Pressure-driven micromixers, initially proposed by Deshmukh et al. [76], often feature simple designs with just two cross channels or a main channel and one or more side channels. Niu and Lee [77] created a pressure-driven micromixer that induced chaotic mixing through fluid stretching and folding, optimizing their design using the Lyapunov exponent. In contrast, Electric-field-driven micromixers utilize electrohydrodynamic disturbance (EHD) and electrokinetic instability (EKI) to enhance mixing. EHD micromixers employ alternating current (AC) and direct current (DC) electric fields to charge fluids, disrupting their interface and improving mixing [78]. Magnetic field-driven micromixers rely on magneto-hydrodynamics but can also be activated by various means such as permanent magnets, electromagnets, magnetic stirring, or integrated electrodes. Nouri et al. [79] used a permanent magnet to study the mixing of deionized water and Fe3O4 ferrofluid in a rectangular Y-mixer channel, where the ferrofluid traveled from the bottom to the top of the channel under the magnetic field, causing the two fluids to mix.

Finally, thermal-field-driven micromixers take advantage of thermal energy to improve mixing. This can involve increasing the diffusion coefficient, utilizing thermal bubbles, or leveraging electrothermal effects. For instance, Tan [80] simulated mixing in a Y-mixer with an embedded microheater, where thermal bubbles acted as micropumps to drive streams and induce mixing.

Passive micromixers

Passive micromixers have become a critical component in the field of microfluidics, offering efficient mixing without the need for external energy sources. The foundation of passive micromixers relies on the mechanisms of molecular diffusion and chaotic advection, utilizing the unique geometry of microchannels, the contact area between the fluids is increase, resulting in enhancement of both diffusion and chaotic advection [81], [82].

Delving deeper into their designs, passive micromixers can be broadly categorized into three-dimensional (3D) and two-dimensional (2D) configurations. The 3D micromixers, despite their fabrication challenges, provide a plethora of mixing possibilities due to their complex structures. Among the 3D varieties:

Lamination Based Micromixers: Known for multilayer structures, these excel in quick and effective mixing. The aclinic multi-lamination-based micromixer, for instance, boasts of up to 90% mixing efficiency in a mere 0.64 milliseconds, making it suitable for proton exchange reactions [83][84]. Another variant, the crossing manifold micromixer, rearranges fluids in both vertical and horizontal orientations, achieving a 90% mixing rate [85].

Chamber-Based 3D Micromixers: These integrate specific structures like convergence-divergence and recirculation to heighten efficiency. For instance, the H-shaped version, by splitting and recombining fluids, achieves an impressive 0.98 mixing efficiency at a Re = 0.083 [85]–[87].

Overbridge Based Micromixers: These micromixers depend on splitting and recombination, with one model showing over 90% efficiency for various Reynolds numbers [86].

3D Spiral-Based Micromixers: Utilizing spiral microchannels, these can reach up to 90% efficiency for certain Reynolds numbers. A unique design incorporating double helical channels can even achieve 99% efficiency for a spectrum of Reynolds numbers [88].

Shifting focus to 2D micromixers, one prominent category is obstacle-based micromixers. These leverage in-channel obstacles to boost mixing. For example, the design with straight grooves instigates secondary flows, resulting in effective mixing across a range of Reynolds numbers [89][90].

Another approach employs barriers, where height and shape modifications can significantly influence efficiency [91].

Curved channel-based micromixers, even without obstacles, have shown potential, especially with the incorporation of radial barriers, which result in around 72% efficiency at Re=81 [92].

Unbalanced Collision-Based Micromixers stand out in the 2D domain. They exploit asymmetric channel structures or fluid flow rate differences. Examples include Ansari et al.'s micromixer, which uses unbalanced collisions and Dean vortices, and Xia et al.'s design with fan-shaped cavities, achieving 78% to 86% efficiency [93][94].

The spiral-based designs have been revolutionized since Schönfeld et al.'s introduction [95]. Further advancements combined them with unbalanced collisions, utilizing Dean vortices in curved channels, proving effective in mixing [96].

The principle of convergence-divergence also finds applications in micromixers. For instance, designs with sinusoidal walls or meandering channels have achieved up to 92% and 80% efficiency respectively [97][98]. Moreover, innovations combining split-and-recombine structures with convergence-divergence walls have reported efficiencies of around 95% [99].

Here, we are aiming to develop an available and low-cost method, while reducing the complexities and time consumption in exosome studies. It makes it more likely to be portable, bringing it closer to the concept of a fully integrated lab-on-a-chip device. Furthermore, among the passive micromixers, despite the fact that 3D micromixers has widely been used to enhance mixing. they are not favorable for us due to their complex fabrication processes, which often involve time-consuming and costly techniques, making them less practical for widespread applications. Thus, we instead opt to use passive micromixers in order to examine their effect on improving interaction and isolation of vesicles through their incubation with TiO_2 particles.

1.5 Liposomes as a model for exosomes

A key challenge in exosome research is the difficulty in characterizing exosomes in heterogeneous biological fluids prior to isolation [44]. This makes it difficult to determine whether observed differences in exosomes are inherent characteristics of the vesicles themselves or artifacts resulting from the isolation process. Key features of exosomes such as their size, density, and shape can provide valuable insights into their origin within the body[99], and whether they indicate a healthy or diseased state. Generally, exosomes are spherical in shape, with a size typically ranging from 30-200 nm [1]–[4], and a density of around 1.1-1.2 g/ml [100], [101].

In many applications of exosome studies their size plays an important role, for instance, there are studies suggesting that tumor cells might produce exosomes of different sizes compared to those produced by normal cells, even though both types fall within the typical size range.

One study indicates that plasmatic exosomes, particularly their size and concentration, can be powerful indicators in distinguishing prostate cancer patients from healthy individuals. The study reveals that prostate cancer patients have notably smaller and more numerous plasmatic exosomes compared to healthy subjects. This difference in exosome size and concentration offers a potential non-invasive diagnostic tool. While specific biomarkers, like PSA-expressing exosomes, have higher predictive accuracy, the non-specific metric based on exosome size and concentration remains significant in diagnostics. The Receiver Operating Characteristic (ROC) analysis, which combined the size and number of plasmatic exosomes, showed high sensitivity (89%) and specificity (71%) for distinguishing between prostate cancer and control group [102].

In a comparative study [103] of exosomes derived from various cell lines, more details of distinguishing features of exosomes were studied. HOSEPiC, a normal ovarian epithelial cell line, produced exosomes with the broadest size range, peaking at 267 nm as observed with EM.

Conversely, IGROV1, an ovarian cancer cell line, displayed the smallest mean diameter across all measurement methods. Concentration-wise, the differences among cell lines are subtle, with ES-2 cells edging out with the highest production of exosomes per million cells. However, the most significant contrast emerges in the protein biomarker EpCAM's presence. While OVCAR3-derived exosomes lead with the highest EpCAM labeling, potentially indicating a robust epithelial origin or its potential as a tumor marker, HOSEPiC, despite being non-cancerous, also showcases a notable EpCAM presence. This highlights the correlation of the biomarkers of exosomes derived from different cell lines to their size distributions.

Size distribution of exosomes has also been reported to be a potential marker for oral cancer detection and monitoring [104]. The study revealed that the vesicles derived from oral fluids (OF) of oral cancer (OC) patients exhibited significant size differences when compared to those from healthy individuals (HI). Specifically, exosomes from OC patients had a broader size distribution, with some reaching up to 400 nm in diameter, while those from HI peaked at 300 nm. This size difference indicates the presence of potentially unique tumor-derived extracellular vesicles in OC patients. These larger vesicles in OC samples may serve as potential biomarkers for oral cancer detection or monitoring.

On the other hand, it has been reported that the isolation method used for exosomes from biofluids significantly influences their yield, purity, content, and integrity [44]. Alvarez et al. investigated explored six different protocols for isolating exosomes from urine, aiming to identify the best methods for proteomic analysis and RNA profiling for biomarker discovery. The first set of methodologies they implemented are ultracentrifugation-based method including standard differential centrifugation, then incorporating an additional ultracentrifugation step with a 30% sucrose cushion to increase purity and lastly involving passing preprocessed urine through a 0.22-

micrometer filter just before ultracentrifugation. The next category in their study is nanomembrane concentrator-based utilizing vivaspin 20 nanomembrane ultrafiltration concentrator. And the last category is commercial exosome precipitation reagent-based methods, employing ExoQuick-TC, a reagent specific for the isolation of exosomes from urine and cell.

It has been shown that the isolation methods directly impact the quality of subsequent proteomic and RNA analyses [105], [106]. As a result, ensuring exosomes are intact post-isolation is crucial, as their morphology, content, and biological function can be compromised, leading to inaccurate research findings or diagnostic results. To do so pre isolation characterizations are crucial. As a result, to ensure the reliability of our methodology and its minimal impact on the integrity of vesicles, we employed liposomes as a model system for study. Liposomes, synthetic lipid vesicles, serve as an excellent model system due to their structural and compositional similarities to exosomes. Both share common physical properties [107], such as density (typically ranging from 1.00 to 1.15 g/mL[107]–[109]) and similar chemical properties due to their lipid bilayer composition [109].

Furthermore, the size of liposomes can be precisely controlled due to their synthetic nature. Like exosomes, liposomes are enclosed by a bilayer of amphiphilic phospholipids, consisting of hydrophilic phosphate heads facing the aqueous environment and hydrophobic fatty acid tails oriented inward. The presence of phosphate groups in the outer surface of the liposome bilayer allows them to interact similarly with TiO_2 particles, as observed in exosome isolation[109]–[111] (Figure 3). This bilayer structure closely resembles that of exosomes, making it possible to isolate liposomes using the same techniques as exosomes. Furthermore, by utilizing liposomes as a model system in research scenarios offers numerous advantages. Researchers can formulate liposomes with specific properties, (like labeling them with fluorescence, their composition and size), making it easier to track, analyze, and assess their behavior in various experimental setups. Such tailored studies can provide invaluable insights into vesicle recovery rates post-isolation and shed light on the impact of purification processes on vesicle size distribution [112]. This can then be translated to refine exosome isolation techniques, making them more efficient and reducing potential artifacts introduced during the process.

In following sections in cases where the working material is referred to in a general form, we have referred to exosomes and liposomes as vesicles.

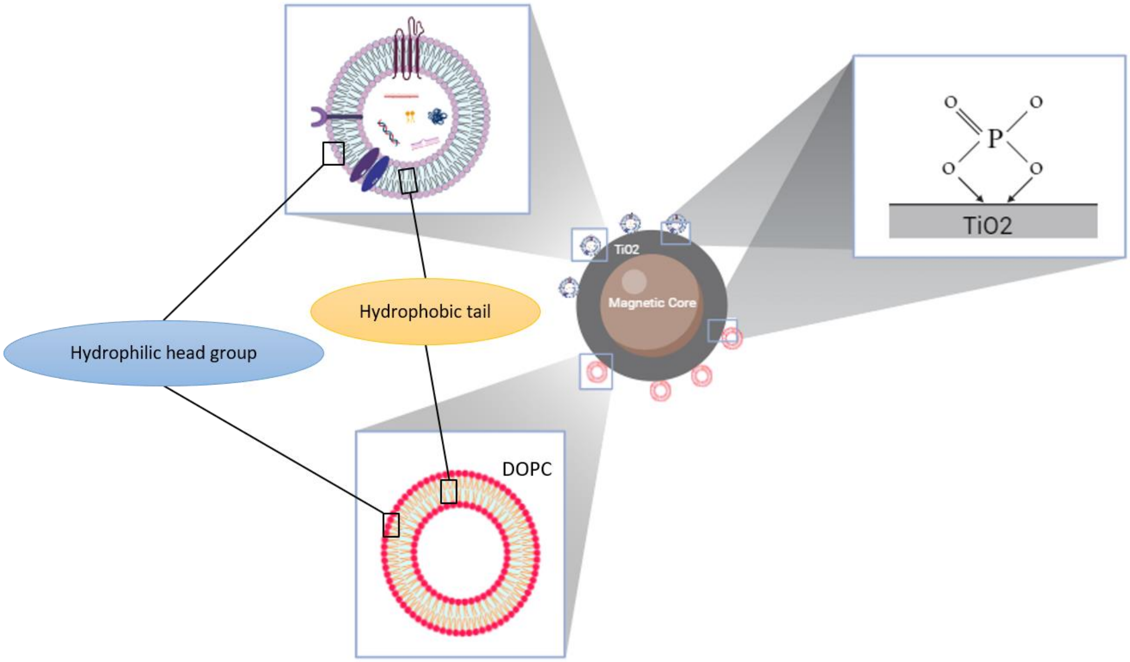

Figure 3 - Graphical abstract of working principle: mechanism of TiO_2-based isolation. Top right: chemical interaction between TiO_2 and phosphate groups of vesicles. Top left: exosome containing diverse biological cargo enclosed by phospholipid bilayer membrane. Bottom left: DOPC liposome, a spherical vesicle composed of a phospholipid bilayer made primarily of dioleoylphosphatidylcholine (DOPC).

1.6 Objectives

The aim of this study is to explore the effectiveness of a microfluidic platform for TiO_2-based exosome isolation. We aim to address the challenges and limitations of conventional isolation techniques by harnessing the specific interaction between TiO_2 and exosomal lipid bilayers to achieve high purity, recovery, and yield. We also seek to investigate the use of liposomes as a model system to understand the potential impact of isolation methods on the physical attributes of exosomes. By using liposomes as a model for exosomes, we aim to assess the integrity and recovery of isolated vesicles and gain insights into the advantages of using a microfluidic platform for exosome research. By mixing TiO_2 beads and exosomes in a microfluidic micromixer, we aim to improve isolation efficiency and assay times, facilitating on-chip characterization for potential clinical applications and personalized medicine.

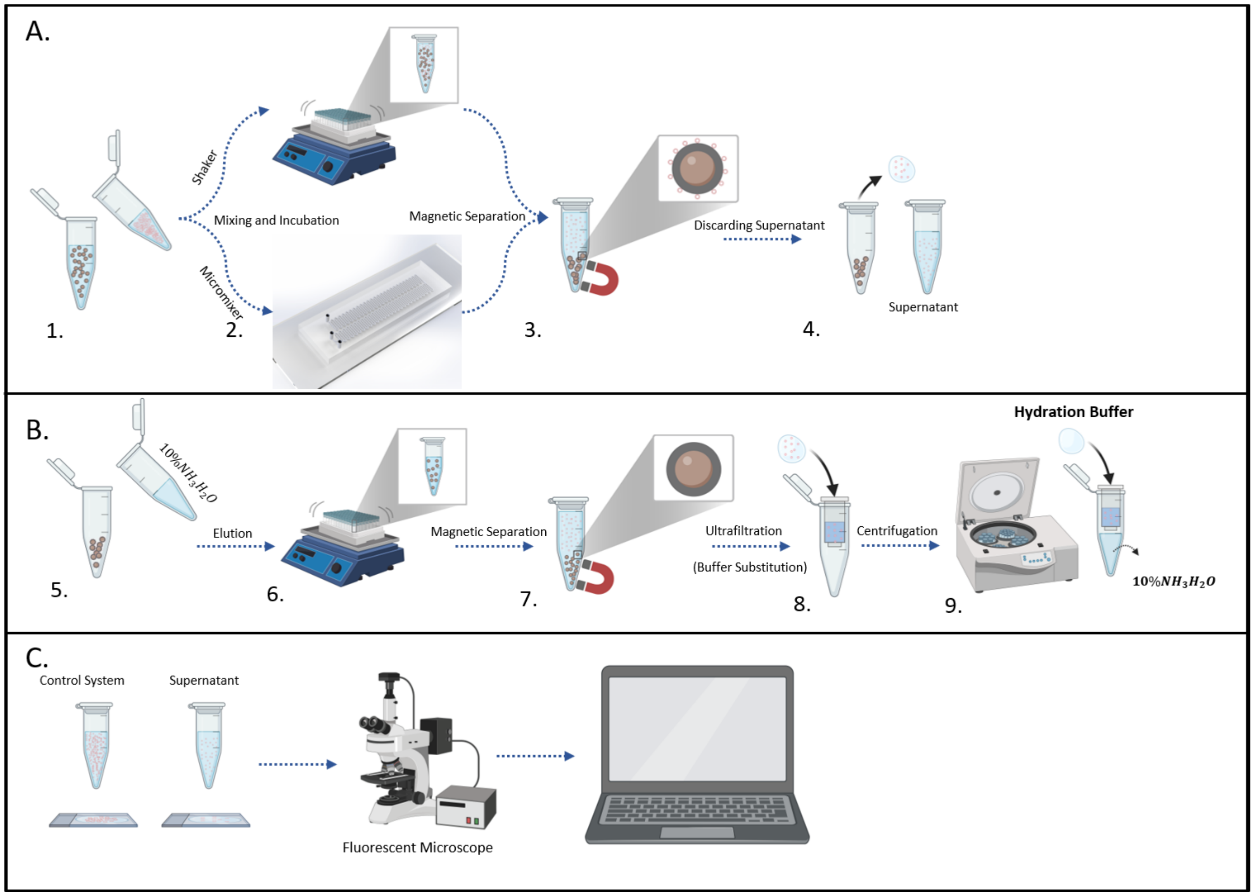

Figure 4 - Graphical abstract of experimental process A. Mixing and incubation step. B. Elution step. C. Efficiency calculation method.

Chapter 2: Microfluidic setup development and evaluation

2.1 Micromixer selection

To achieve the optimum isolation efficiency, ensuring an effective incubation of TiO_2 and vesicles are required as well as having an efficient mixing which is a prerequisite. Proper mixing ensures that the particles come into adequate contact with the vesicles, allowing for the intended interactions to occur efficiently. Without sufficient mixing, the incubation may not be effective, leading to suboptimal isolation efficiency.

As mentioned in previous sections, micromixers provide numerous advantages over conventional mixing methods including the precise control both of small-scale particles and the flow and affordability [113]. Notably, microfluidic devices significantly shorten analysis times compared to their macro-scale counterparts Consequently, incorporating these devices with laboratory equipment not only accelerates analysis but also conserves space. As we discussed earlier micromixers are found in various types out of which we picked 2D passive micromixers as our ideal candidates, in order to avoid the complexity of their active counterparts and the difficulty of the fabrication of 3D passive micromixers. In this chapter we elaborate on the steps of developing our final optimum micromixer.

2.1.1 Initial designs

According to the proposed goals, 3 initial designs were put into test named design 1,2 and 3.

As shown in Figure 5, the design 1 is a Zigzag micromixer that employs serpentine channels with sharp bends to induce chaotic advection and enhance mixing in microfluidic devices. The repeated folding of fluid streams leads to efficient mixing [114].

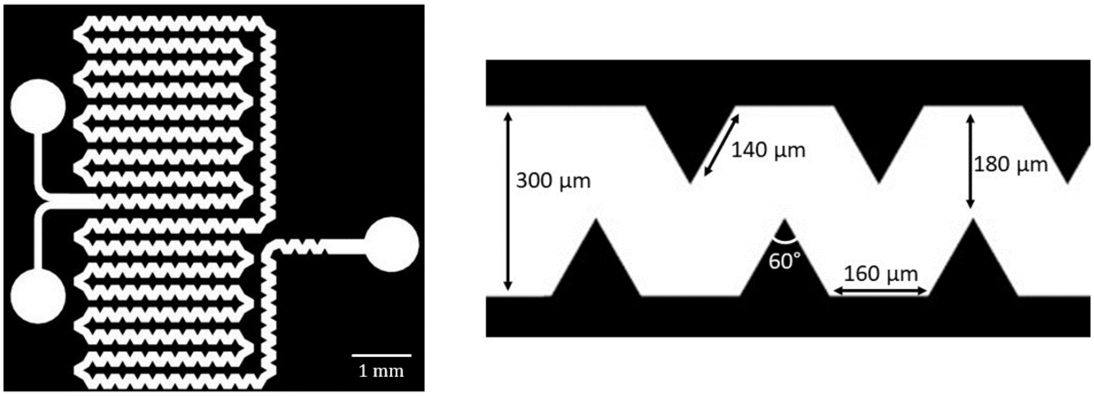

Figure 5 - Design 1: schematic and its dimensions

Multi-curve mixers are advantageous due to their ability to take advantage of Dean vortices in addition to diffusion for improved fluid mixing [115]. When fluids flow through channels with multiple curves, such as serpentine or helical geometries, at sufficiently high Reynolds numbers, centrifugal forces drive the formation of Dean vortices. These swirling vortices cause fluid elements to follow complex, helical paths, enhancing their interaction and promoting thorough mixing. This phenomenon significantly accelerates mixing compared to straight channels, where molecular diffusion is the primary mixing mechanism. In [115] the interlocked semi-circle (ILSC) was investigated. Their simulation covers the results at different Reynolds numbers (Re = 0.01, 0.1, 1, 5, 10, 20, 30, 40, 50), analyzing how the flow pattern of a fluid changes under varying conditions. The Reynolds number is a dimensionless quantity used to predict the flow regime of fluids. It is calculated as the ratio of inertial forces to viscous forces and is given by the formula Re = $^{\rho VL}/_{\mu}$, where ρ is the fluid density, V is the fluid velocity, L is a characteristic length, and μ is the dynamic viscosity of the fluid. Each of these values represents a different flow regime. Lower Reynolds numbers (like 0.01 or 0.1) usually correspond to laminar flow, where the fluid flows in smooth, orderly layers. Higher Reynolds numbers (such as 30, 40, 50) are indicative of when it becomes chaotic and disordered. By adding a greater number of modules, they have achieved high efficiency in low flow rates as well. We employed their design as our second micromixer, design 2 (Figure 6).

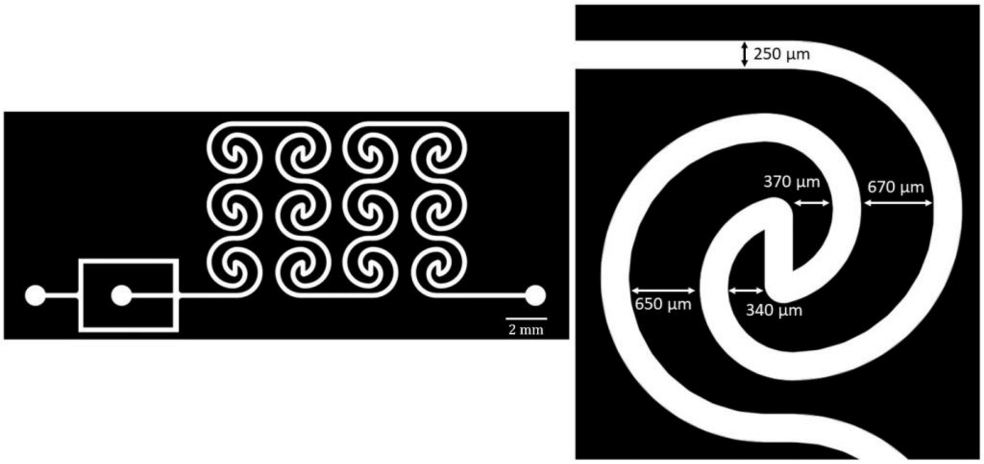

Figure 6 - Design 2: schematic and dimensions

The serpentine design was a previously investigated micromixers by other co-researchers inspired by the work carried out by Karthikeyan, K. & Sujatha, L. [116]. They suggested that their design is suitable for applications requiring small input energy and is adaptable to various research applications due to the high mixing efficiency in wide range of flow rates (both low and high flow rates). A few modifications were made to their design as our third design, and the detailed dimensions are shown in Figure 7.

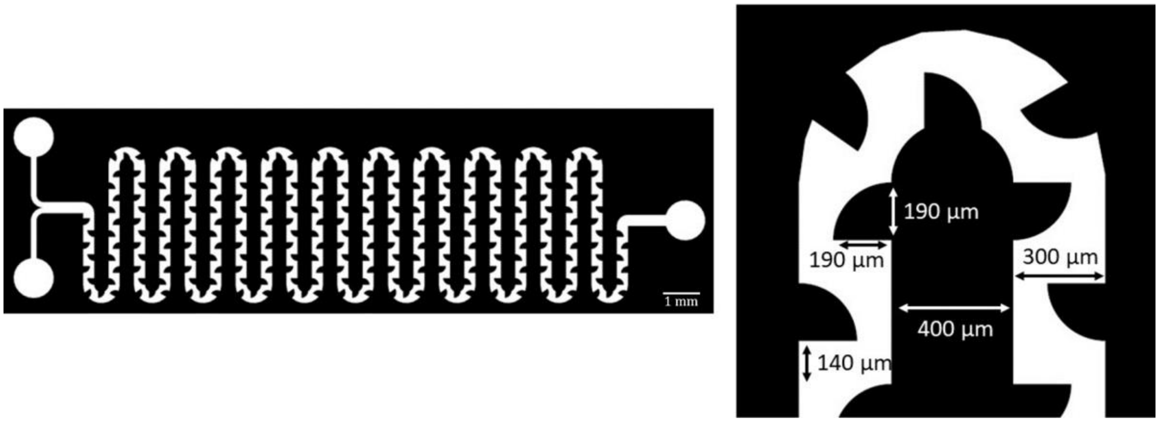

Figure 7 - Design 3: schematic and dimensions

2.1.2 Evaluation of initial micromixer designs

The main desirable objective of designing an optimum micromixer is to achieve a highest possible capturing efficiency. The first step to have a high capture rate is to have a high mixing efficiency. One of the primary determinants influencing mixing efficiency is the Re number, defined earlier. For each micromixer design, optimal mixing efficiency is achievable within a specific range of Re numbers. In general, the two primary mechanisms contributing to the mixing process are diffusion and convection, which are dominate at low and high flow rates, respectively. When we introduce particles into the working samples, assuming these particles move within the flow at the same velocity as the fluid, we can anticipate no significant alteration in the flow regime compared to using only fluids. Exosomes, tiny vesicles measuring approximately 100 nm in size, and TiO_2 particles, which are substantially larger at around 1.5 microns, exhibit notably different behaviors when introduced into a fluidic environment. Exosomes can be reasonably assumed to move at a velocity similar to that of fluid molecules due to their minute size and mass. Conversely, TiO_2 particles, with their significantly larger size and mass, do not share the same velocity as the surrounding fluid within the channel, resulting in distinct transport characteristics resulting a change in the efficiency obtained in each flow rate. As a result, to better understand these behaviors and optimize mixing efficiency, the investigation of each micromixers' performance was done in two steps starting with a series of preliminary experiments were conducted using water and ink. These experiments were crucial in providing valuable insights into the ranges of flow rates at which optimal mixing efficiency can be achieved. Subsequently, the TiO_2 particles dispersed in PBS were introduced to the inlet of the micromixer instead of ink.

2.1.2.1 Mixing Performance Evaluation Step 1: Water and Ink

By introducing water and ink (Club House, food color) to our micromixers, we observed that when we operate at low and high flow rates, where diffusion and convection play significant roles in mixing respectively, we achieve high mixing efficiencies. Conversely, at medium flow rates, our expectations for achieving high mixing rates are lower. Our primary objective is to determine the upper limit of the low flow rate range, where we can achieve efficient mixing, as well as the lower limit of the high flow rate range, where proper mixing remains elusive. Essentially, we aim to identify the boundaries within which optimal mixing is not attained.

To investigate this, we conducted tests for each design at flow rates of 5,7, 10, 20, 40, 50, 70, 100, and 150 using imaging under microscopic Echo Revolve. Our findings, illustrated in the Figure 8 (provided as an example from design 3, but consistent across all designs), reveal that even at medium flow rates in the outlet, we achieve fully mixed fluids. However, at both low and high flow rates, we observe that complete mixing occurs earlier along the channel (Figure 8). This not only implies a higher likelihood of achieving good mixing for particle-added working samples but also extends the incubation time after the samples are uniformly mixed, which is a significant advantage. Our metric in this context was to achieve complete mixing before reaching the final quarter of the channel. The transition points from low flow rates with efficient mixing to medium flow rates with reduced mixing quality, and the subsequent transition from medium to high flow rates (the first point at which efficient mixing is achieved again) are recorded in Table 2 for each design. As obtained, the design 3 exhibiting low mixing efficiency within a narrow flow rate range of 10-50 meaning a broad range with a high efficiency.

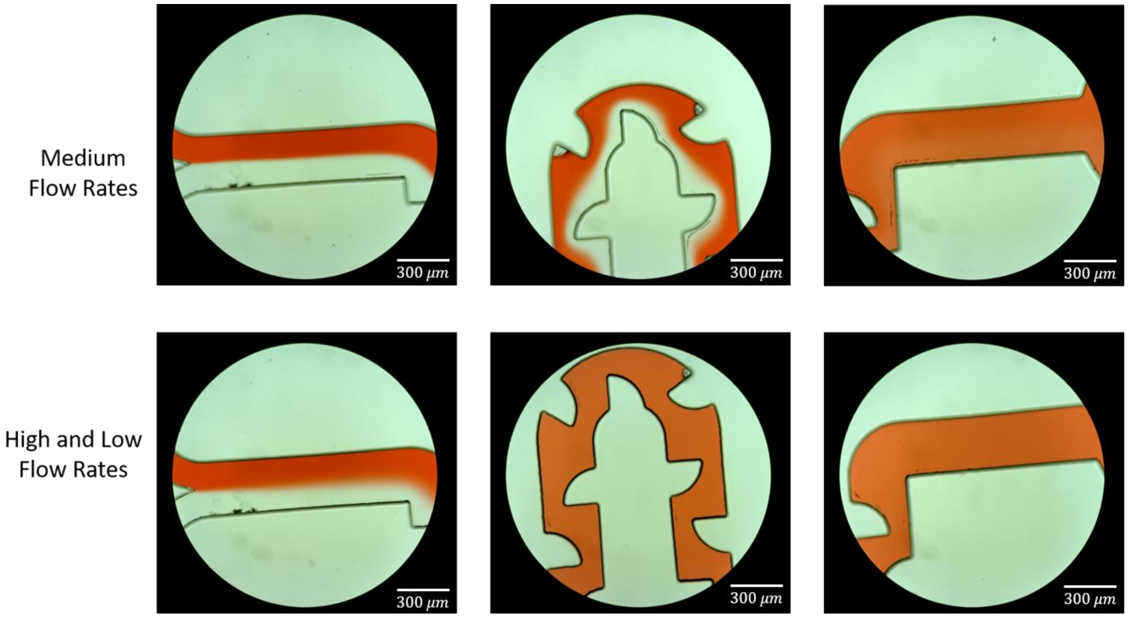

Figure 8 - Mixing performance using water and ink: high efficiency of mixing for a wide range of flow rates

Table 2 – Flow rate transition points of mixing efficiency for water and ink inlet samples across micromixer designs

	Design 1	Design 2	Design 3
Low flow rate limit ($^{\mu l}/_{min}$)	7 ± 2	5 ± 2	10 ± 2

High flow rate limit $^{\mu l}/_{min}$	70 ± 5	70 ± 5	50 ± 5

2.1.2.2 Mixing performance evaluation step 2: water and TiO_2 particles dispersed in water

As the second step of evaluation of the micromixers' performance in terms of the mixing effectiveness, we improved our working samples from water and ink to water and TiO_2 particles dispersed in water. The TiO_2 coated silica magnetic particles (SMP-UM26, CD-Bioparticles) with a broad size distribution and average of the $1.5\ \mu m$ were utilized. The original concertation was $50\ mg/ml$ (Approximately $1.14\ \times\ 10^{10}$ $patricles/ml$). As anticipated, the introduction of TiO_2 particles led to notable alterations in the previously mentioned limits. Specifically, the maximum low flow rate required to attain a fully mixed sample at the outlet decreased to a mere 1 μl/min. For the flow rate of 1 μl/min a high mixing efficiency is achieved early in the channel (Figure 9) but various problems have been observed. Due to the low momentum at low flow rates, particles often become trapped at the inlet (Figure 10). This can lead to unpredictable scenarios: sometimes the channel gets completely clogged, stopping the flow, while at other times, particles gradually enter the channel over time in a random and sporadic manner. Such irregularities result in inconsistent concentrations of TiO_2 in the flow, causing a loss of control over the incubation process (Figure 11).

Consequently, when a significant portion of TiO_2 particles get trapped at the inlet and does not enter the channel, it results in the loss of exosome samples. This is because, during their presence in the channel, there isn't enough available surface area of TiO_2 for liposomes or exosomes to attach. In essence, the limited interaction opportunity in the channel leads to the underutilization of $\mathrm{TiO_2}$ and exosome sample. On the other hand, during high-concentration flows of $\mathrm{TiO_2}$, these particles can accumulate within the channel. This accumulation can be substantial enough to create a barrier that interferes with the movement of other particles, including liposomes/exosomes. As a result, the close proximity of titanium particles may prevent them from coming into contact with liposomes/exosomes, reducing the likelihood of necessary interactions.

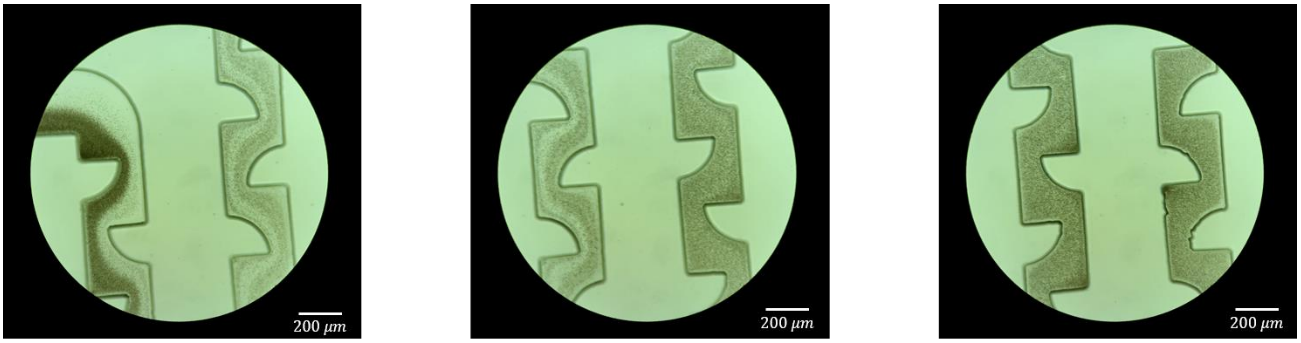

Figure 9 - Mixing in low flow rates

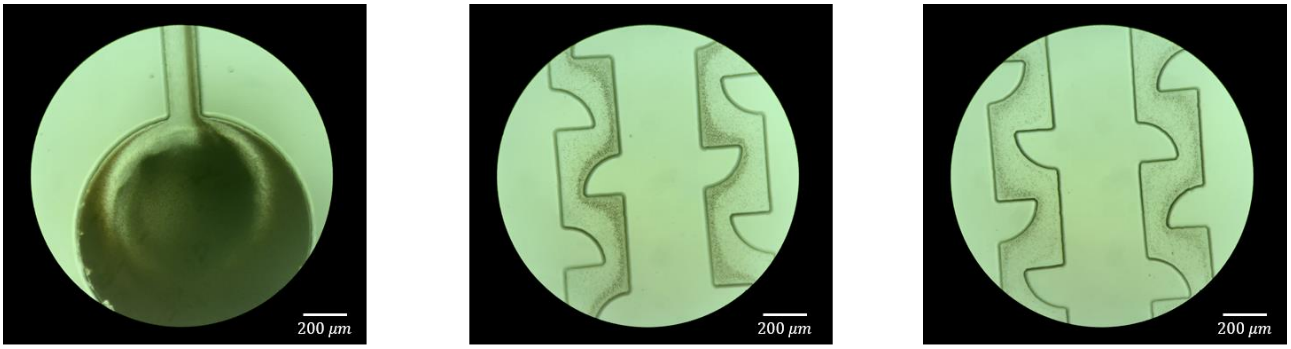

Figure 10 - Channel blockage at the inlet and adhesion to the walls along the flow path for low flow rates

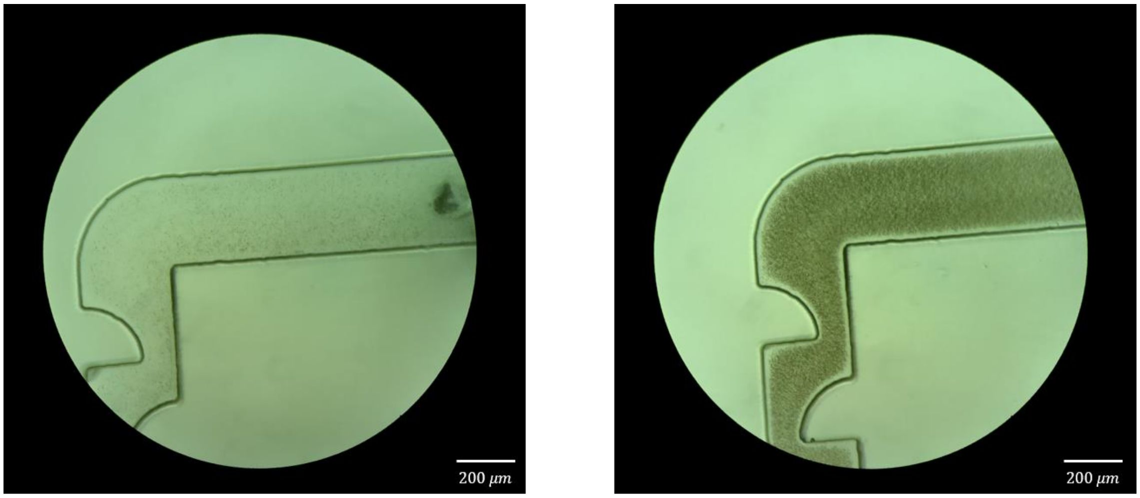

Figure 11 - Inconsistency of concentration due to the accumulation of particles in the inlet

Within the flow rate range of 1 to 70 (three replicates for each flow rate were done), we continuously observed low mixing efficiency (Figure 12). However, in the range of 70 to 100, achieving a well-mixed sample proved to be still challenging task, with the desired level of mixing being achieved only towards the very end of the channel (Figure 13). In contrast, for the other two designs, we encountered challenges for low flow rates and effective mixing did not occur. Additionally, the upper limit for medium flow rates, having relatively weaker mixing efficiency, increased to 90 for design 1 and 100 for design 2. The summary of these transition points for all their designs are documented in Table 3.

Table 3 - Flow rate transition points of mixing efficiency for water and inlet TiO_2 particles dispersed in water samples across micromixer designs

	Design 1	Design 2	Design 3
Low flow rate limit ($^{\mu l}/_{min}$)	-	-	1

High flow rate limit $^{\mu l}/_{min}$	90 ± 5	100 ± 10	70 ± 10

They underscore the pivotal role of channel design when dealing with samples containing larger particles like our TiO_2 particles. It highlights a significant contrast compared to our previous experiments with two fluid working samples, where we consistently achieved satisfactory mixing efficiencies at the channel's end across various flow rates. These findings emphasize the complexity and sensitivity of the mixing process, particularly when dealing with larger particles, and emphasize the importance of tailored channel designs for specific applications.

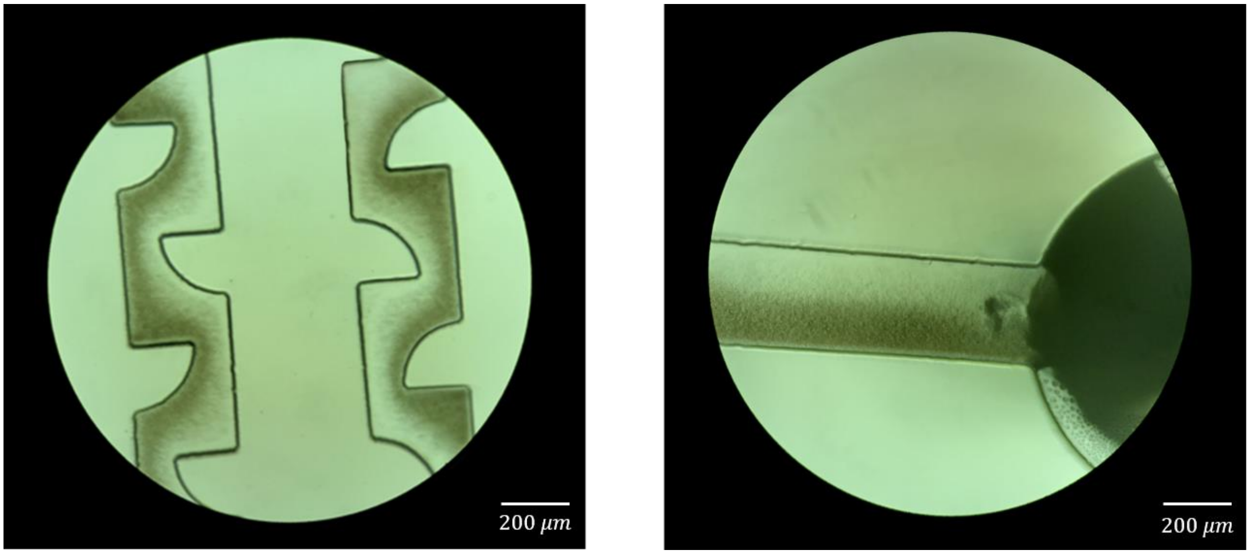

Figure 12 - Low efficiency mixing

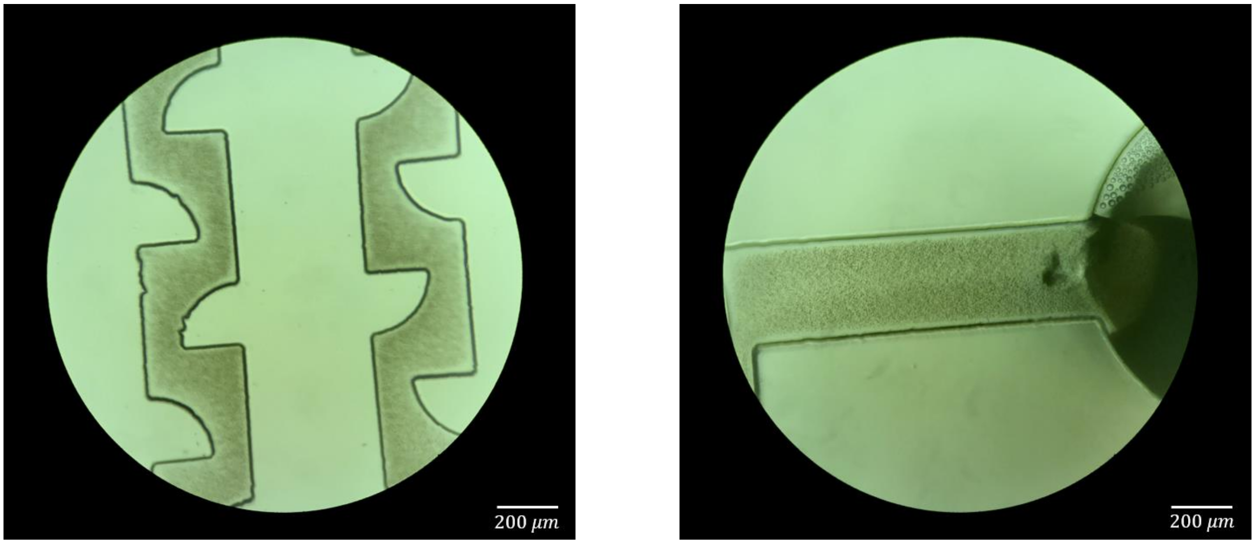

Figure 13 - High efficiency mixing

2.1.2.3 Incubation Evaluation: sodium dodecyl sulfate (SDS) and TiO_2 dispersed in water

Principles and motivation of using SDS

Achieving efficient capture of exosomes/liposomes by TiO_2 particles is a crucial aspect of our research, and this relies directly on effective incubation. While high mixing efficiency is undeniably essential for satisfactory incubation, several other critical factors come into play. Among these factors, one of the most pivotal is ensuring an adequate incubation time, as it significantly enhances the probability of effective interactions between liposomes and TiO_2 particles. In these series of experiments, we chose to work with SDS (sodium dodecyl sulfate) micelles as a model system in the process of design the micromixers requiring high number of trials and repetitions. SDS is a simple amphiphilic molecule with well-known properties. Notably, it is a cost-effective and widely available substance, making it an ideal candidate for preliminary tests during the design and evaluation of the micromixer.

Nano and micron-sized particles, such as TiO_2 particles, inherently possess a high tendency to agglomerate due to their small size and large surface area. A surfactant, short for surface-active agent, is a molecule or compound designed to reduce the surface tension between two phases, typically a liquid and a solid or a liquid and a gas. Surfactants typically consist of a hydrophilic (water-attracting) head and a hydrophobic (water-repelling) tail. These characteristics allow surfactants to stabilize dispersions of particles in a liquid medium, effectively forming colloidal suspensions. SDS is an anionic surfactant commonly used in chemistry and biology. When SDS is added to a system containing nanoparticles or microparticles, the hydrophobic tails of the SDS molecules surround the particles' surfaces, while the hydrophilic heads extend into the surrounding aqueous solution.

The SDS molecules create a repulsive force between particles by maintaining a barrier of charged hydrophilic heads. This repulsion counteracts the attractive forces, such as Van der Waals forces, between the particles (Figure 14). As more SDS is added, once a critical concentration of SDS is reached in the solution, known as the critical micelle concentration (CMC), the hydrophobic tails of multiple SDS molecules aggregate together into a spherical (micelle), with the hydrophilic heads facing outward and the hydrophobic tails shielded inside in a self-assembly process. Micelles being formed in the solution, reduces the interfacial tension and further provide this steric stabilization the dispersion [117], [118]. Given the significance incubation and mixing in the stabilization mechanism using SDS and the working principle explained, we employed a dynamic light scattering technique to evaluate the effectiveness of our incubation in each the micromixer and subsequent successful interaction.

Characterization

Dynamic Light Scattering (DLS), also known as Photon Correlation Spectroscopy or Quasi-Elastic Light Scattering, is a technique used in physics and chemistry to determine the size and size distribution of particles or molecules in a suspension or solution. DLS works by analyzing the fluctuations in the intensity of scattered light caused by the Brownian motion of particles suspended in a medium. Brownian motion is the random movement of particles suspended in a fluid due to thermal energy. Smaller particles experience faster and more intense Brownian motion than larger ones because the force of thermal collisions is proportionally stronger for smaller particles. When a laser or monochromatic light is directed at a sample containing these particles, the light interacts with the particles and gets scattered in various directions. The scattered light intensity is not constant but fluctuates over time due to the continuous Brownian motion of particles. A detector placed at a specific angle from the incident light collects the scattered light. DLS measures the fluctuations in the scattered light intensity over time. These fluctuations are caused by the particles moving in and out of the laser beam's path, resulting in variations in the scattered light intensity. The key to correlating these fluctuations to particle size is the autocorrelation function. Autocorrelation in DLS is a technique that measures how similar the intensity of scattered light is at different time intervals. In DLS, snapshots of light scattering are rapidly captured and compared to the initial signal. When comparing closely spaced snapshots, the signals are highly correlated, representing consistent particle motion. As the time lag between snapshots increases, the correlation decreases, indicating changing particle behavior. Eventually, the signal loses all correlation, signifying significant particle motion. Larger particles in DLS diffuse slowly, taking more time for the correlation signal to decay with increasing time lag. Smaller particles undergo rapid diffusion, leading to a quicker decay in correlation. The autocorrelation function provides peaks that reflect particle size and diffusion rate. Wider peaks suggest size diversity, while peak position indicates particle mobility in DLS analysis.

Eventually, DLS utilizes the Stokes-Einstein equation to relate the diffusion coefficient (D) of particles to their size (a), temperature (T), and the dynamic viscosity of the fluid (η):

$$a = \frac{6\pi\eta}{kT}$$

Where:

a is the hydrodynamic size of the particles.

k is the Boltzmann constant.

T is the absolute temperature of the fluid.

η is the dynamic viscosity of the fluid.

D is the diffusion coefficient.

By knowing the temperature, viscosity of the fluid, and the measured diffusion coefficient, DLS calculates the hydrodynamic size of the particles in the sample [119], [120].

Measurements for both DLS were carried out using a Zetasizer Pro DLS (Malvern Panalytical). For consistent results, samples were prepared by diluting them 1:50 in a 10% sucrose (Sigma-Aldrich), 20 mM HEPES (Sigma-Aldrich) buffer, with a total volume of 1.5 ml. Each sample was replicated and characterized three times to ensure precision.

Evaluation

Using this powerful and straight forward characterization technique we can compare the size distribution of TiO_2 particles before and after incubation with SDS micelles, quantifying the effectiveness of the incubation process. A shift towards smaller particle sizes observed in the DLS data indicates improved incubation and successful prevention of agglomeration [117].

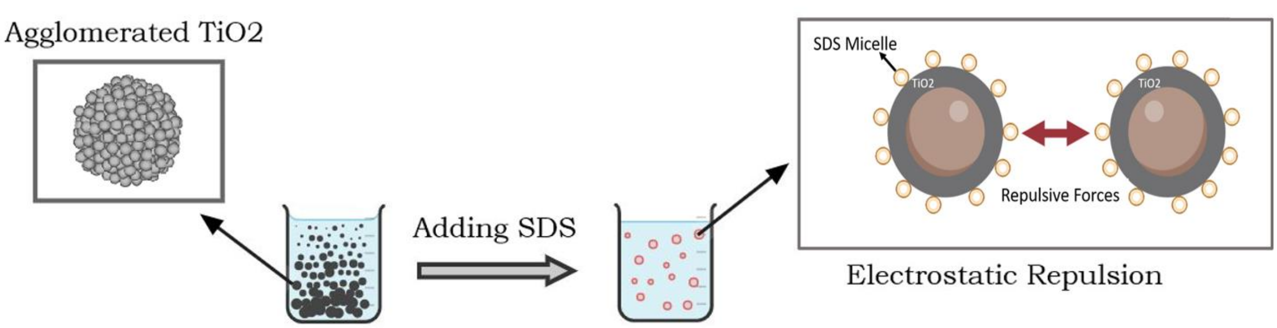

Figure 14 - Illustration of surfactant action: stabilizing nano and micron-sized particles with SDS

In order to determine the maximum achievable reduction in particle size distribution, we conducted initial experiments using a vortexer for 7 minutes, a robust mixing method suitable for non-biological and non-fragile samples. This allowed us to investigate the impact of different concentrations of SDS on our TiO_2 sample before sonicating. The critical micelle concentration (CMC) for SDS is known to be 8.2 mM. ([121]) Thus, we tested SDS concentrations of 8, 10, 50, 100, 200, and 300 mM for a sample containing TiO_2 particles/m. The average of three replicates of these tests are shown in Figure 15. The modal and mean diameter for each experiment (these are the average from 3 replicates) and the change of them from pre-processed particle are summarized in Table 4.

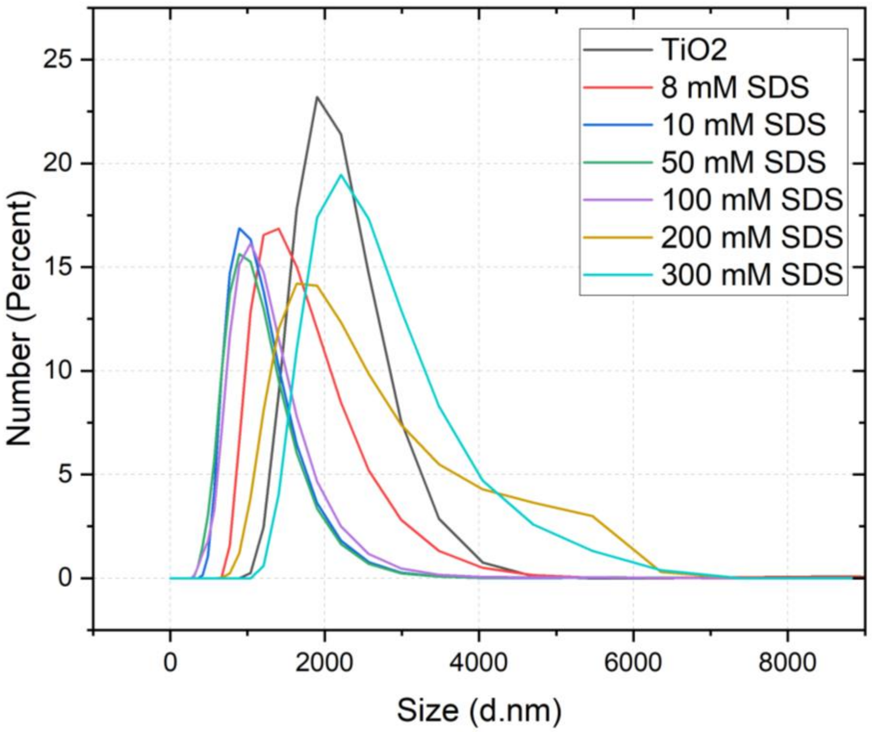

Figure 15 - Size distribution shift by introducing different concentrations of SDS

Table 4 - Size distribution shift by introducing different concentrations of SDS

	Pure TiO_2	TiO_2 /8 mM SDS	TiO_2 /10 mM SDS	TiO_2 /50 mM SDS	TiO_2/100 mM SDS	TiO_2/200 mM SDS	TiO_2/300 mM SDS
Modal Diameter	1644.25 ± 91.57	1215.75 ± 37.1	898.78 ± 72.34	867.45± 72.34	1045.2 ± 38.4	1644.25 ± 41.65	21.46 ± 43.73
Mean Diameter	1815.09± 143.8	1603.4 ± 27	1084.74 ± 102.9	1047.18 ± 87.36	1141.99 ± 63.25	2284.87 ± 51.34	2532.59 ± 42.59
Change in Modal	-	--26.06 ± 3.7	-45.34 ± 0.77	-47.24 ± 1.2	-36.43 ± 3.61	0 ± 4.8	30.52 ± 5.1
Change in Mean	-	−11.66 ± 3.81	-40.24 ± 0.87	-42.31 ± 3.54	-37.08 ± 4.3	25.88 ± 7.1	39.53 ± 3.61

The most favorable results, characterized by the maximum reduction in TiO_2 particle size following the addition of the surfactant, were achieved using a concentration of 50 mM SDS, resulting in a remarkable 47% reduction in modal diameter and a 42% reduction in mean diameter (Figure 16). Based on these promising results from our bulk experiments, we chose the 50 mM SDS concentration for our microfluidic tests. These tests were specifically conducted within Micromixer design 3, which demonstrated superior mixing performance across a wide range of flow rates. Our objective was to assess the performance of the micromixer in terms of providing an effective incubation as well as good mixing by examining how closely we could replicate the results obtained through vortexer mixing, a known high-rate mixing control system.

During experimentation with medium flow rates, we observed only minor changes in size distribution. This minimal alteration can be attributed to the fact that although a weak mixing is observed, SDS and TiO_2 are introduced to the inlets are poured to the same vial at the end of the channel layer by layer. As a result, downstream of the channel, where both inlet samples are combined in the same vial, certain SDS molecules have the chance to access the surfaces of TiO_2 particles, providing some mitigation of agglomeration, albeit to a limited degree.

At high flow rates while we achieved thorough mixing along the channel resulting in a homogenous sample, the rapid flow rate prevented particles from spending sufficient time in the channel to undergo effective incubation. Consequently, we observed minimal differences in size distribution, indicative of the surfactant, SDS, not performing optimally due to inadequate incubation in these conditions.

Regarding low flow rates, it is important to note that preparing 1 ml, the minimum sample volume required for DLS characterization, of sample at a total flow rate of 2 μl/min takes an extensive 8-hour duration. This extended timeframe presents challenges such as TiO_2 particle sedimentation in the syringe potential for channel clogging, which was previously discussed. These issues arise due to the low momentum associated with low flow rates and have the potential to introduce inaccuracies into the results. Despite these challenges, we have presented all our findings in the accompanying Figure 17. The modal and mean diameter for each experiment (these are the average from 3 replicates) and the change of them from pre-processed particle are summarized in Table 5.

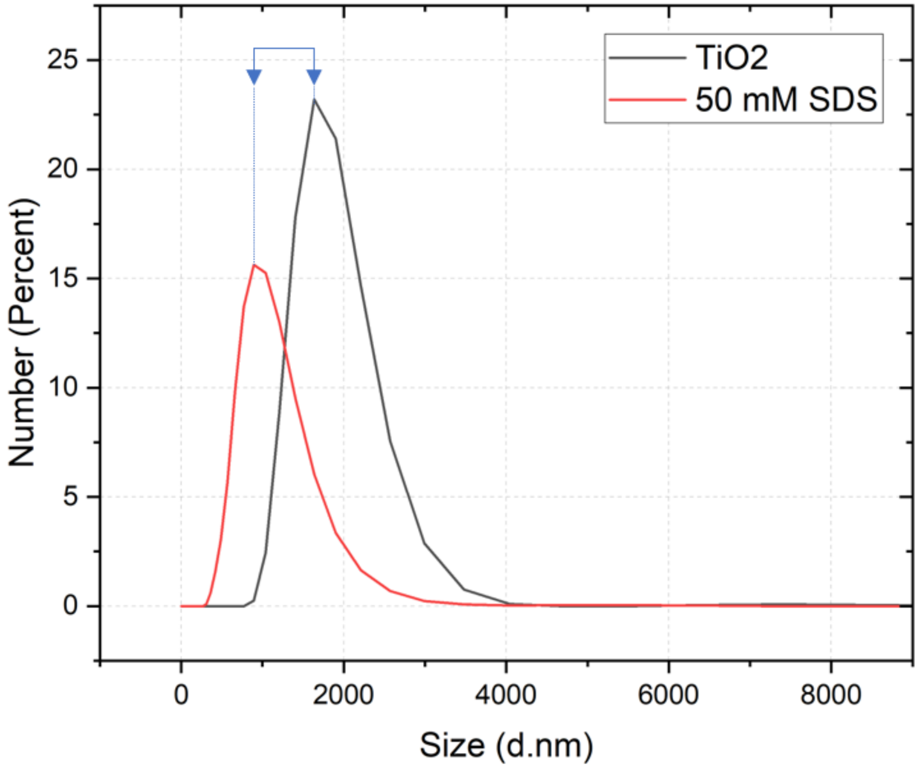

Figure 16 - Size Distribution shift by introducing 50 mM SDS through bulk experiments

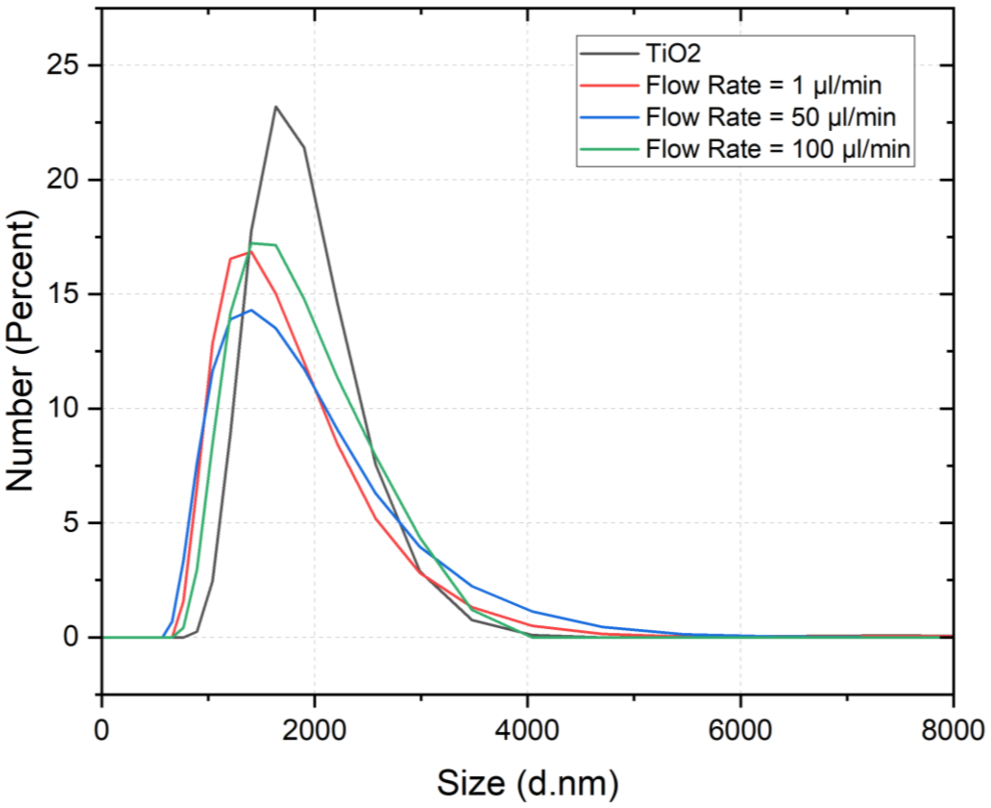

Figure 17 - Shift in size distributions across flow rates in design 3

Table 5 - Size distribution shift across flow rates in design 3

	Pure TiO_2	Flow rate = $1\,{}^{\mu l}/_{min}$	Flow rate = $50\,{}^{\mu l}/_{min}$	Flow rate = $100\,{}^{\mu l}/_{min}$
Modal diameter	1644.25 ± 97.57	1218 ± 10.2	1437.33 ± 101.35	1402.21 ± 100.6
Mean diameter	1815.09 ± 143.8	1378.74 ± 51.41	1665.81 ± 61.72	1478.42 ± 98.76
Change in modal	-	-25.92 ± 4.9	-12.58 ± 1.36	-14.72 ± 0.93

Change in mean	-	-24.04 ± 3.93	-8.22 ± 4.06	-18.55 ± 3.56

2.1.3 Enhanced micromixer designs

To address the challenges encountered in the initial three designs, we recognized the need for substantial improvements. These issues included limited flow rate range for achieving effective mixing (only the third micromixer achieved good mixing at flow rates below 1), frequent clogging and high assay time at low flow rates, and inadequate incubation time at higher flow rates (above 100), due to both the high velocity of flow and the fact that complete mixing only occurred at the very end of the channel. In response to these challenges, we designed three new micromixers (named as design 4, 5, and 6), each tailored to potentially overcome these limitations. To reduce the possibility of clogging in the channel which occurs due to the low momentum at low flow rates, we used a micromixer with less barriers in the channel. Low momentum flow means that the fluid velocity is relatively slow. When a fluid with a flow rate of 1 has particles moving at a velocity of 0.000833333 m/s, each particle has a momentum of approximately 3.65×10^{-18} kg·m/s, whereas at a flow rate of 70, with particles moving at a velocity of 0.058333333 m/s, the momentum of each particle increases to approximately 2.56×10^{-16} kg·m/s.

When the fluid moves slowly, it may not have enough kinetic energy to carry the particles effectively through the micromixer channels. As a result, particles may settle or get stuck within the channels. The rounded-corner secondary fractal micromixer (RCSM) design (Figure 18) [128], introduced in our design 4 significantly reduces the pressure-drop preventing clogging by reducing the force pushing particles into the channels.

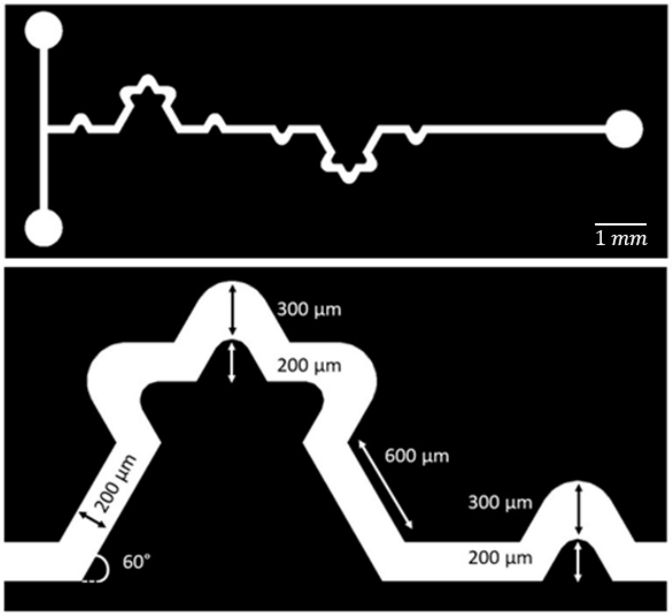

Figure 18 - Design 4 (RCSM) schematic and dimensions

To address the problem of insufficient incubation time associated in high flow rates we devised two additional designs of 5 and 6. The design 5 incorporates dedicated incubation sections (Figure 19), while the design 6 extends the length of the original configuration (Figure 20).

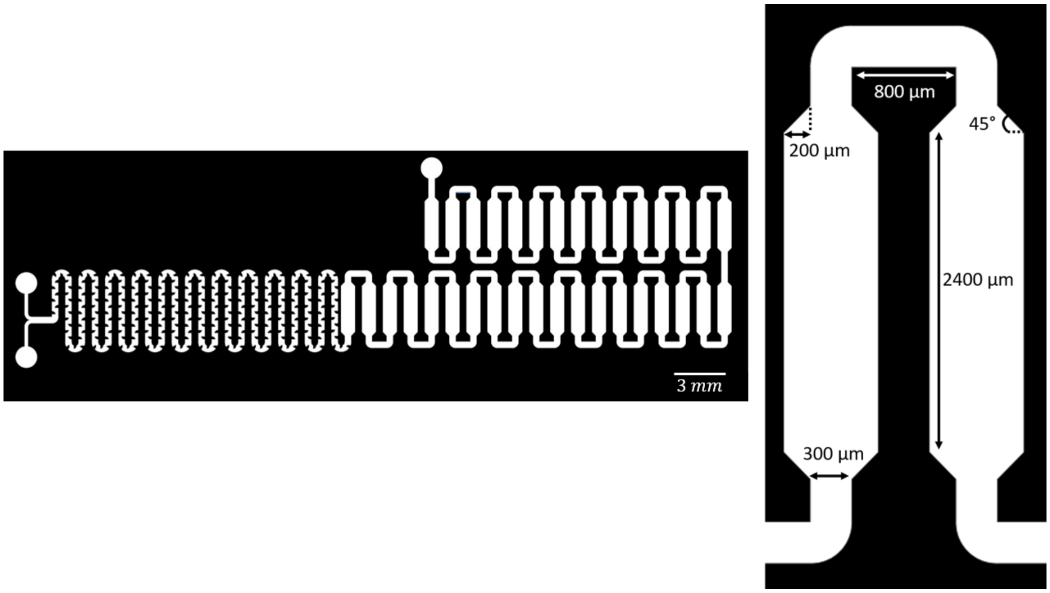

Figure 19 - Design 5 schematic and dimensions

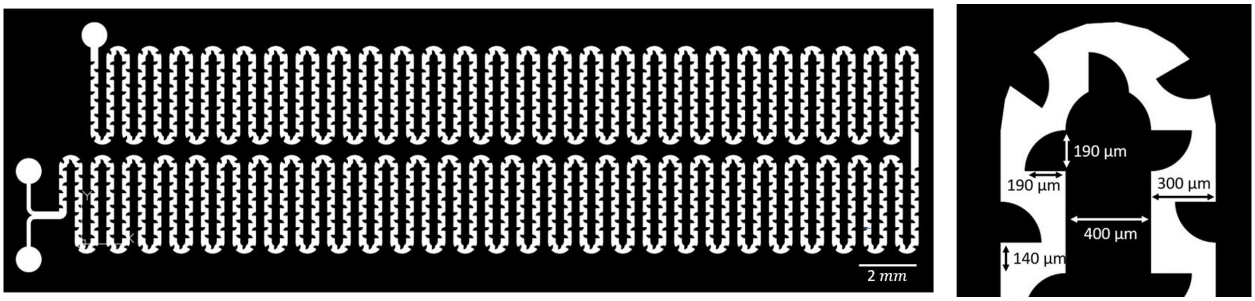

Figure 20 - Design 6 schematic and dimensions

2.1.4 Evaluation of optimized designs

As mentioned above, when the pressure drop is high, it can force particles into narrow passages or dead-end zones, increasing the likelihood of blockages. Lowering the pressure drop, introduced in design 4, minimizes this force, making it less likely for particles to become lodged and ensuring smoother flow through the channels. For this design we observed although the limit of low flow rate remained 1 µl/min, clogging does not occur in the RCSM design (Shown in Figure 21).

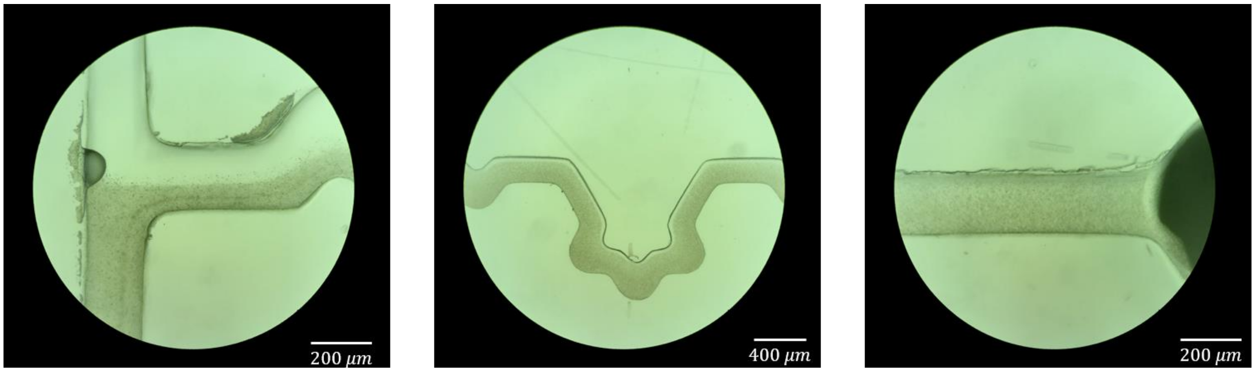

Figure 21 - Mixing in RCSM design at 1 µl/min

In the incubation-focused design (design 5), where mixing primarily takes place in the initial section (mixer), once the unmixed flows enter the incubation segment (between 1-100 $^{\mu l}/_{min}$), we did not observe any substantial changes (Figure 22).

Hence, as shown in Figure 23 , showing the average data of 3 replicates, we observed no significant alteration in size distribution shifts, accordingly in the flow rate ranges with satisfactory mixing compared to the original design (design 3). However, based on resultant mixing in the elongated design (Figure 24), a broader range of flow rates demonstrated complete mixing. Based on the DLS results of this micromixer that for both low flow rates (between 5-10 $^{\mu l}/_{min}$) and high flow rates (above 70 $^{\mu l}/_{min}$), extended length of the micromixer contributed to effective mixing and provided a somewhat adequate incubation and mixing period (Substantial changes in the size distribution is observed between before preprocessed particles and after incubation with SDS Figure 25), simultaneously, ensuring favorable results in both scenarios. The summarized results from DLS characterization of design 6 are reported Table 6.

The optimum size was achieved in the micromixer design 6 with a flow rate of $70\,^{\mu l}/_{min}$ with 36.21% modal diameter reduction which is comparable to the results from bulk incubation.

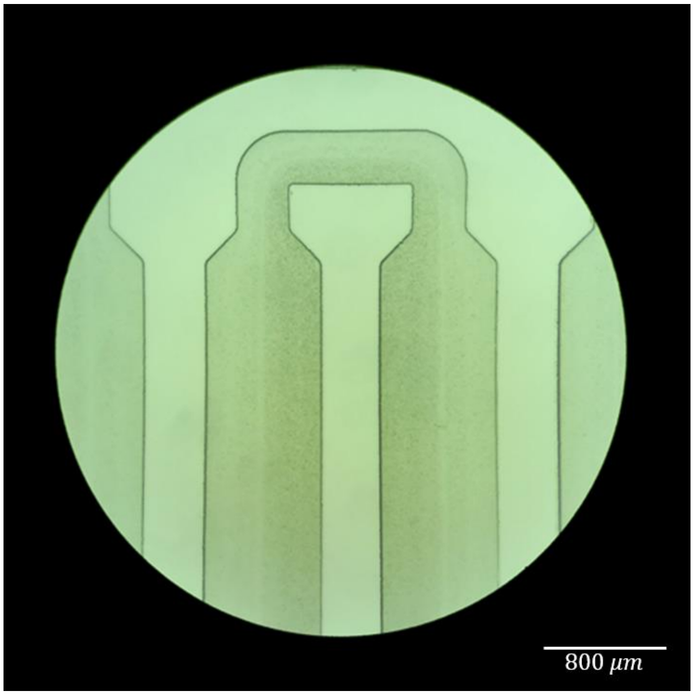

Figure 22 - Design 5 - Incubation section

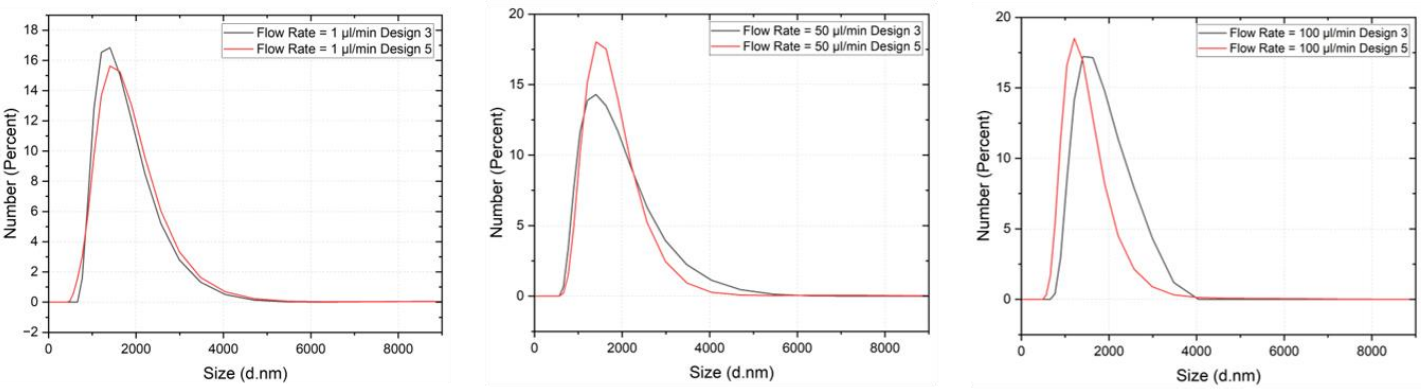

Figure 23 - Size distribution comparison design 3 and design 5

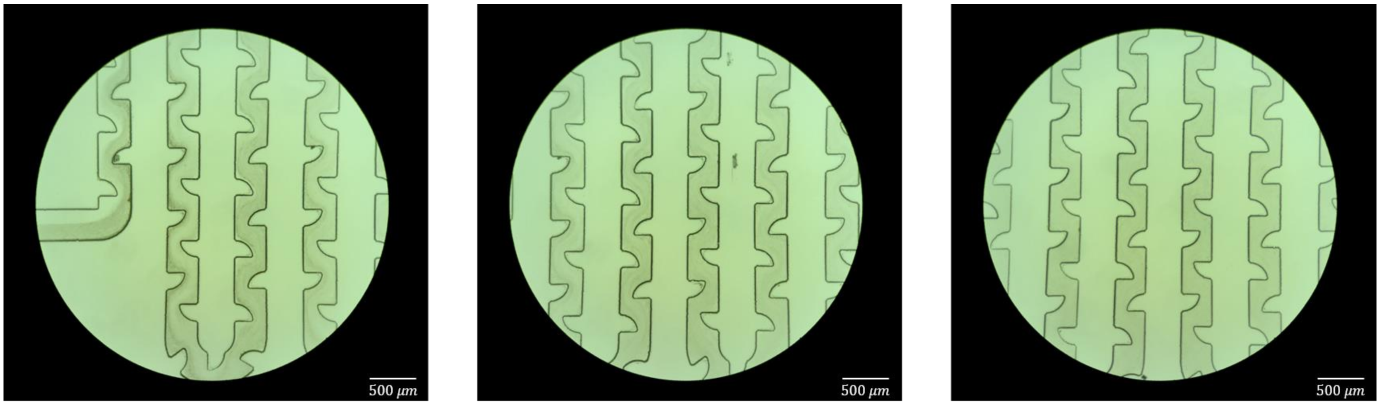

Figure 24 - Mixing in design 6

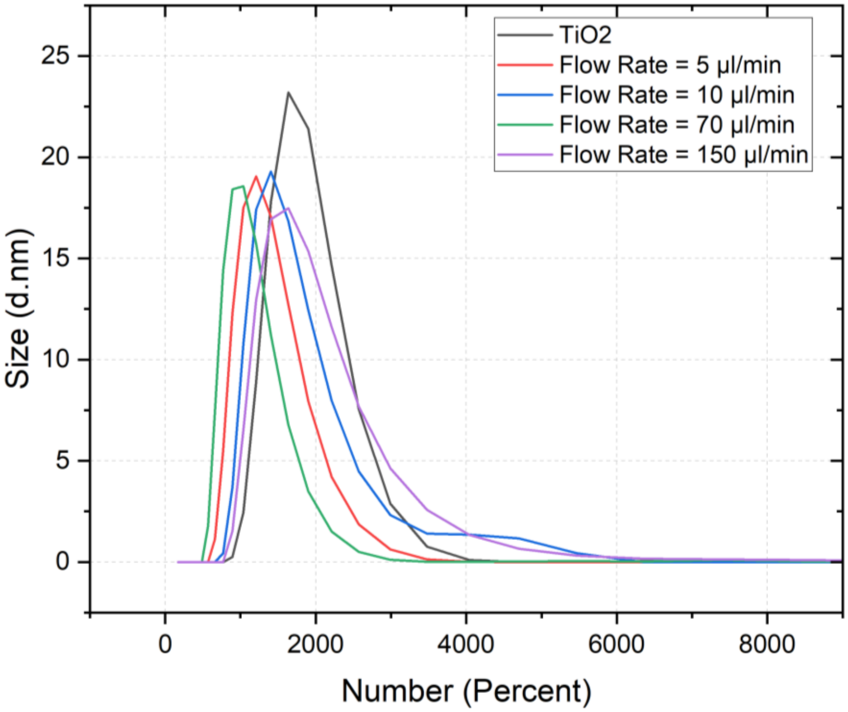

Figure 25 - Shift in size distributions across flow rates in design 6

Table 6 - Shift in size distribution across flow rates design 6

	Pure TiO_2	Flow rate = $5\ ^{\mu l}/_{min}$	Flow rate = $10\ ^{\mu l}/_{min}$	Flow rate = $70\ ^{\mu l}/_{min}$	Flow rate = $150\ ^{\mu l}/_{min}$

Modal Diameter (unit)	1644.25 ± 97.57	1219.8 ± 12.02	1418.8 ± 73.09	1048.92 ± 23.4	1438 ± 56.51
Mean Diameter (unit)	1815.09± 143.8	1334.67 ± 23.02	1683.76 ± 42.13	1119.59 ± 42.9	1608.02 ± 39.87
Change in Modal	-	-25.81 ± 1.9	-13.71 ± 3.31	-36.21 ± 3.43	-12.54 ± 1.01
Change in Mean	-	-26.47 ± 2.64	-7.23 ± 2.86	-38.32 ± 4.5	-11.41 ± 0.86

2.2 Fabrication of micromixer

For micromixers with larger dimensions of 100 microns, we initiated the fabrication process using cost-effective and readily available 3D-printed resin molds. To achieve precise results in our final micromixer molds, we opted for photolithography.

The fabrication of a 3D-printed resin mold begins with the creation of an STL file based on the 3D model, having a base no more than 2.5 mm in height and channel walls no wider than 2 mm, utilizing Computer-Aided Design (CAD) software. Subsequently, we employed Lychee Slicer as our slicing software to generate a. ctb (Customized Toolpath Binary) file. This file contains precise instructions for the 3D printer, guiding it on how to construct the part layer by layer.

Once the 3D printing process is complete (we used Phrozen Mini Sonic 8k Printer with a xy pixel resolution of 22 µm Figure 26). The post-processing phase starts. It begins with delicately removing the part from the build plate and eliminating any remaining supports using snipping tools or manual techniques, if necessary. A sonicator and a two-step washing procedure is used to clean the part thoroughly. It is first placed a zip lock bag with Isopropyl alcohol for the initial wash. Then, it is placed in the sonicator for 2 minutes. This process is repeated with a cleaning fluid for the second wash. After washing, the mold is dried, either with pressurized air or by allowing it to air-dry naturally. To render the part safe for handling and ready for use, it undergoes a curing process in a machine equipped with UV lights for a duration of 5 minutes. Ultimately, the molds are placed onto a 120 ºC hot plate and allowed to sit for 2 hours. After undergoing heat treatment, the molds are cleansed using acetone, making them prepared to be filled with PDMS (one example of completed printed molds is shown in Figure 27).

To fabricate the PDMS chips within the master mold, we start by blending the PDMS prepolymer and curing agent (specifically, Sylgard 184 Silicone Elastomer Base and Curing Agent from Dow Corning) at 10:1 ratio. Subsequently, this mixture is carefully poured into the treated resin mold. Following this, the filled resin mold undergoes a degassing process within a benchtop vacuum chamber and is covered with aluminum foil. It is then placed on a hot plate for curing at 105 ºC for a duration of 1 hour and 15 minutes.

Once the PDMS has fully cured, it is meticulously peeled away from the master mold. Inlet and outlet holes are created in the chip using a 1 mm biopsy punch (Miltex) surface cleaned using a 3M tape. Finally, the prepared chips are securely bonded to glass slides using plasma treatment, which involves subjecting them to a 40-second exposure to oxygen at a rate of 18 cc per minute. To reinforce the bonding, the assembled chips are left on a hot plate at 85 ºC overnight.

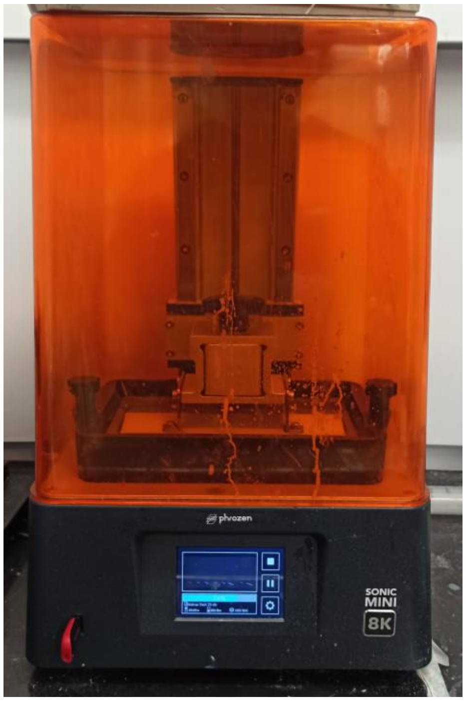

Figure 26 - Phrozen Mini Sonic 8k printer

Figure 27 - 3D-printed resin mold

The final optimized and channels with small dimensions were fabricated using PDMS based on SU8 molds developed on a 3-inch silicon wafers (WaferPro). Initially, a silicon wafer was spin-coated with SU-8 2050 (Kayaku Advanced Materials, Inc.) followed by a two-phase spin coating, Initially, the substrate was spun at 500 rpm for 10 seconds to ensure uniform coverage. For the second step, to deposit a thicker layer, the wafer was spun at of 1750 rpm for 30 seconds, to ensure an even 100 µm thickness.

The wafer underwent a soft bake for 5 minutes at 65 °C and 15 minutes at 95 °C, followed by UV exposure using a photolithography mask (CAD/Art Services) to form the desired pattern for 13 seconds. This UV exposure was succeeded by a post-exposure bake for 4 minutes at 65 °C and 10 minutes at 95 °C. The wafer was then developed in SU8 developer (Kayaku Advanced Materials, Inc.) for approximately 8 minutes, followed by a wash in isopropanol and a hard-bake at 150 °C for 30 minutes to repair surface irregularities (one example of completed Photolithography made molds is shown in Figure 28).

Next, a mixture of PDMS and its curing agent was prepared at a 10:1 weight ratio and poured into the mold. After degassing, this mixture was cured at 85 °C for four hours. The resulting PDMS was then carefully removed, inlet and outlet holes were added and the surface cleaned.

For bonding the channel to a glass slide, after cleaning the slide, the PDMS channel and the glass slide were then exposed to a plasma treatment (PE-50, PLASMA ETCH). The channel was attached to the glass substrate, and the entire chip was placed on a hotplate set at 85 °C overnight to ensure strong bonding and to produce hydrophobic channel walls.

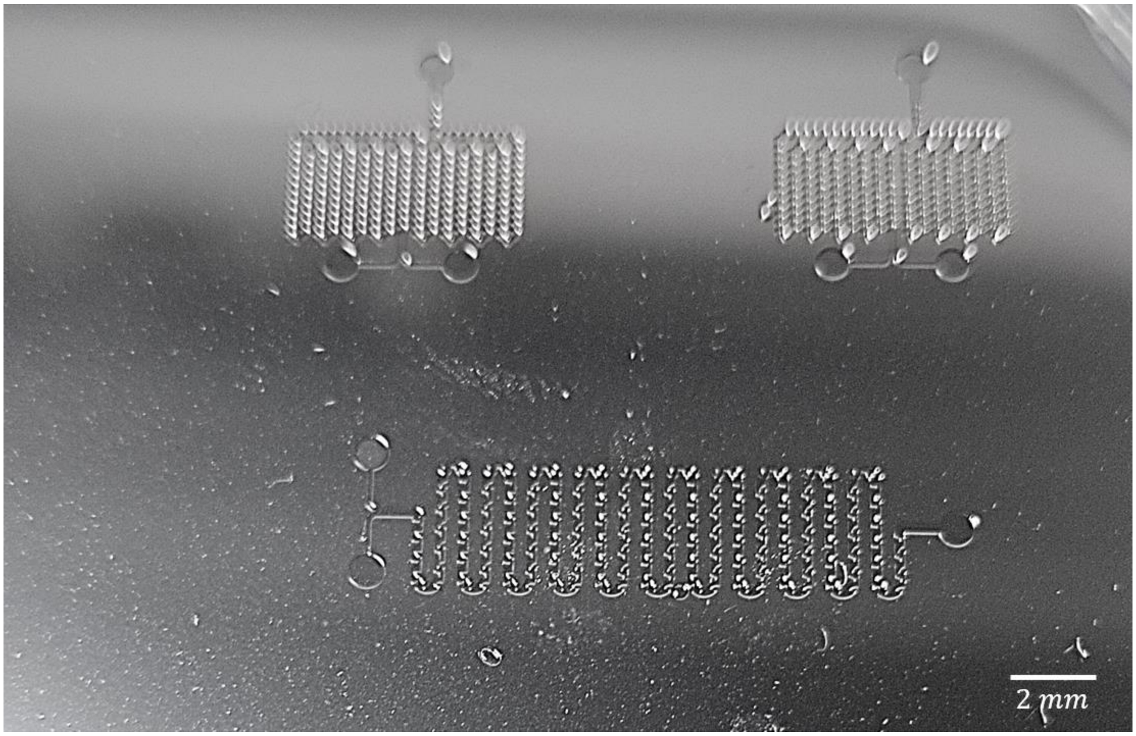

Figure 28 - Photolithography made mold

Chapter 3: Examination of TiO_2-liposome interaction

To assess the feasibility of our methodology, we initiated our investigation by examining the interaction between TiO_2 particles and liposomes. The liposomes used, are composed of DOPC/CHOL/Rh-DHPE at a molar ratio of 54:45:1. Their lipid concentration was approximately 50-55 mM, with a specific Rh-DHPE concentration of 0.5 mM (equivalent to 0.67 mg/mL). These Rh-DHPE-labeled liposomes were prepared by FormuMax through the extrusion method, resulting in a 100 nm size with minimal size distribution. Rh-DHPE is a phospholipid labeled with the red-fluorescent rhodamine B fluorophore, exhibiting excitation/emission maxima at approximately 560/580 nm.

3.1 Fluorescence and bright field imaging

In here, we air-dried a thin layer of TiO_2 particles on a glass slide. Subsequently, liposomes were applied to the slide's surface and gently dispersed, followed by a 15-second gentle manual shaking. Afterward, we conducted three rounds of washing in DI water to remove unbound liposomes. In the Figure 29a (all imaging examinations were conducted with Echo Revolve) and b we compared the TiO_2 particles dried on a slide before and after introduction of liposomes on the surface. As expected, the absence of fluorescence yielded a completely dark image in the case of TiO_2 particles (Figure 29a); however, fluorescence emission was detected in the sample after addition and wash of unbound liposomes (Figure 29b), indicating successful binding of liposomes to the TiO_2 particles, facilitated by chemical interactions involving the phosphate groups of liposomes [58].

Further investigation involved comparing the bright-field image with the corresponding fluorescence image from the sample (Figure 29c, d). This comparison shows similarity in the distribution pattern of titanium particles and the fluorescent spots, which represent areas covered by liposomes. Considering the thorough washing process which has removed the unbound liposomes effectively, leaving behind only those liposome particles firmly adhered to the TiO_2 surface, this similarity suggests the strong bonding of liposomes to TiO_2 particles in only 15 seconds of interaction time.

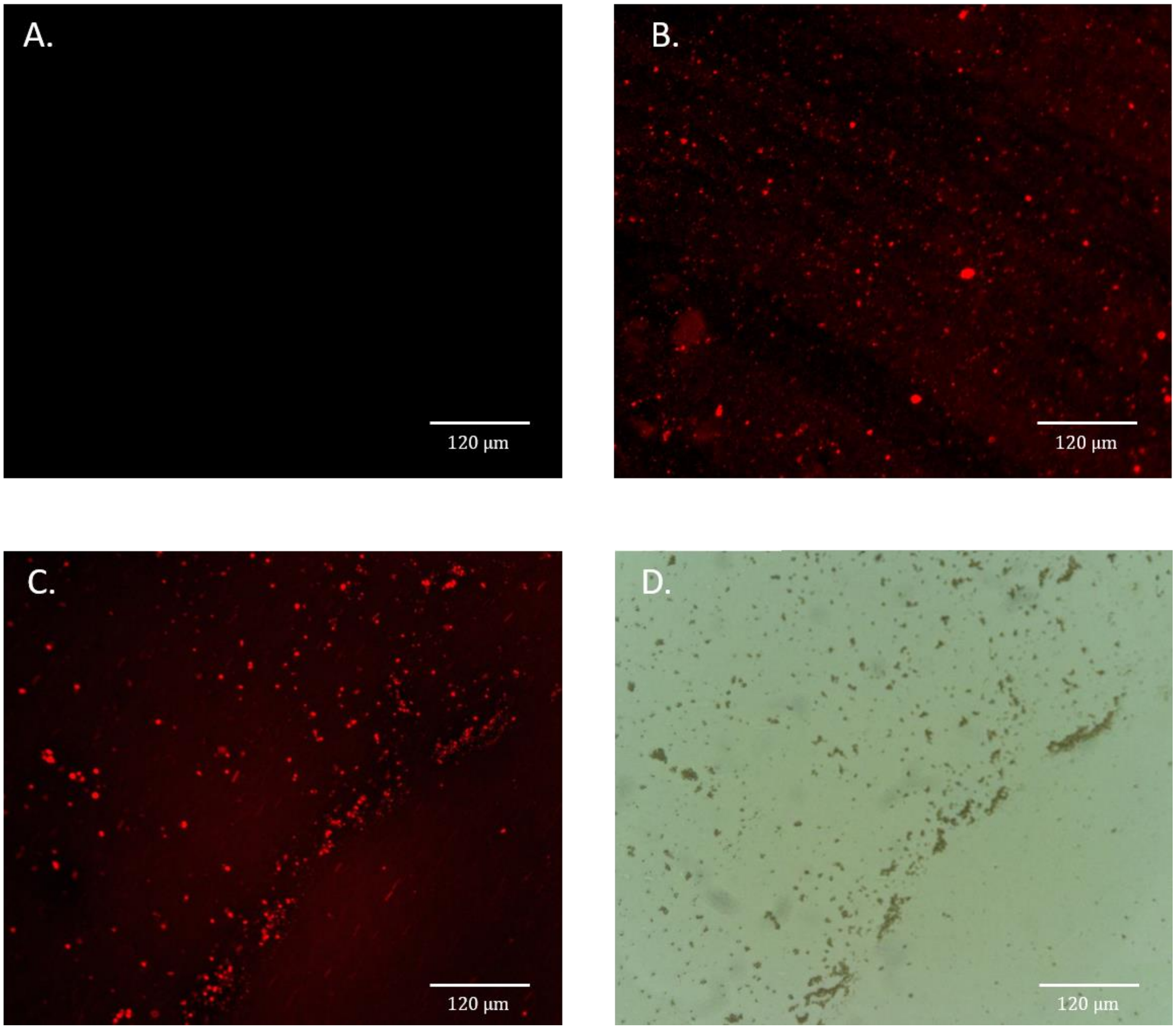

Figure 29 - Visualization of liposome binding to TiO_2 particles on a glass slide surface. (a) Comparison of TiO_2 particles before and (b) after introduction and wash of unbound liposomes. (c, d) Corresponding bright-field and fluorescence images reveal similar distribution patterns of TiO_2 particles and liposomes.

3.2 Size distribution and zeta potential

In the next step, to further verify the interaction between titanium dioxide and liposome particles, we conducted measurements of both the size distribution and zeta potential of the pre-processed $\mathrm{TiO_2}$ particles and liposomes. In previous chapter the mechanism of DLS was explained. Zeta potential of particles are measured with the same device. DLS instruments utilize a special cuvette with electrodes to induce an electric field in the sample solution. When an electric field is applied, charged particles in the suspension experience electrophoresis, which causes them to move through the solution. Particles with a net electric charge will move in response to the applied electric field. As these charged particles move, they create fluctuations in the intensity of scattered light, similar to how Brownian motion causes intensity fluctuations in standard DLS measurements. DLS equipment employs correlation analysis, similar to standard DLS, to measure the fluctuations in the intensity of scattered light caused by the electrophoretic movement of charged particles. These fluctuations are recorded over time and are used to calculate the electrophoretic mobility of the particles. The Zeta potential is not directly measured but rather calculated from the electrophoretic mobility using Henry's equation. Henry's equation relates the Zeta potential (ζ), the electrophoretic mobility (μ), and the properties of the fluid and electric field. The equation is as follows:

$$\zeta = \frac{\mu\eta}{\varepsilon E}$$

Where:

ζ is the Zeta potential.

μ is the electrophoretic mobility obtained from DLS measurements.

η is the dynamic viscosity of the fluid.

ε is the dielectric constant of the fluid.

E is the electric field strength [122].

Having the result of these measurements in hand, we then compared these measurements with those obtained from TiO_2 particles bonded with liposomes. The liposome-bonded TiO_2 particles were collected by employing magnetic settling. This process included the separation of the particles from the supernatant, effectively removing any unbound liposomes that remained after the incubation process.

A shift in zeta potential serves as a potential indicator of interactions occurring on the surface of particles or colloids in a solution. Zeta potential quantifies surface charge, and when binding partners are introduced, which interact with the charged groups on the particle's surface, they can disrupt this electrostatic balance. Consequently, the alteration in zeta potential can signify the presence of these interactions [123], [124]. As shown in Figure 30a, the zeta potential measurements revealed a shift in the surface charge of TiO_2 particles from an initial value of -39.05 mV to -49.71 mV after the magnetic separation of unbound liposomes (summarized in Table 7). This change in zeta potential suggests the presence of liposomes on the TiO_2 surface, as the addition of negatively charged liposomes appears to have further increased the overall negative charge of the TiO_2 particles.

The size distribution analysis of TiO_2 particles before and after the incubation is shown in Figure 30b. For TiO_2 microparticles, the modal size, indicating the most prevalent size within the distribution, was 1644.25 nm. However, the mean size was slightly larger at 1815.09 nm, demonstrating the presence of larger particles contributing to the overall average. TiO_2 particles exhibited a broad size distribution with a full width of half-max (FWHM) of 1096 nm. On the other hand, the liposome-bonded TiO_2 displayed a distinct size distribution with a modal size of 1912 nm, mean size of 2196 nm and FWHM of 1547 nm, indicative of lager particles as well as wider range of sizes compared to TiO_2 particles alone (summarized in Table 8).

The observed difference in size measurements obtained using DLS implies a change in the characteristics of the samples. Specifically, the larger modal diameter in the liposome-bonded TiO_2 compared to pre-processed TiO_2 strongly indicates the formation of a complex resulting from the binding of liposomes to the surface of TiO_2 during their interaction. Additionally, the larger mean size and FWHM for the complex compared to TiO_2 alone suggest that the complex comprises a diverse range of sizes, likely due to variations in the degree of liposome binding or complex aggregation.

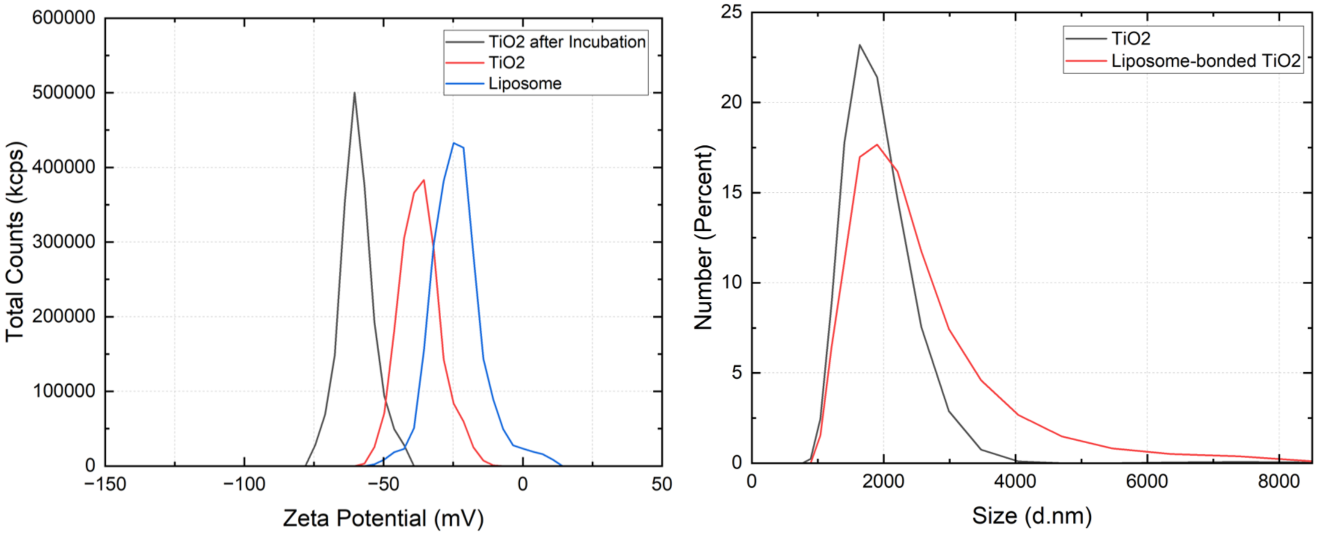

Figure 30 - Characterization of TiO_2-Liposome Interactions: Size Distribution and Zeta Potential Analysis

Table 7 - Zeta Potential of the Samples

	Liposome	TiO_2	Liposome-bonded TiO_2
Zeta Potential (mV)	-60.38 ± 0.68	-39.05 ± 2.31	-49.71 ± 3.09

Table 8 – Size distribution characteristics of the sample

	TiO_2	Liposome-bonded TiO_2
Modal Size (nm)	1644.25 ± 97.57	$1912. \pm 43.03$
Mean Size (nm)	1815.09 ± 143.8	2196 ± 74.3

3.3 Scanning Electron Microscopy (SEM) analysis

In this section, we show the results of scanning electron microscopy (SEM) analysis conducted to elucidate the surface morphology and structural characteristics of TiO_2 particles before and after incubation with exosomes. SEM is a powerful imaging technique used to view the surface topography and composition of materials at high resolution. It operates by scanning a focused electron beam over a sample surface, causing the emission of secondary electrons which are then detected to form an image. This method allows for the detailed observation of surface structures at the micro and nanoscale [125]. For SEM analysis of TiO_2

particles, the following preparation steps were undertaken. TiO_2 microspheres were initially fixed with 1 mL of 2.5% glutaraldehyde (Sigma-Aldrich) in phosphate buffered saline (PBS) (the PBS tablets were purchased from ThermoFisher), for 2 hours. For post fixation, the samples were washed three times with PBS to remove any unbound glutaraldehyde and other residues. The samples underwent a graded dehydration process using ethanol (Sigma-Aldrich) solutions of increasing concentrations (30%, 50%, 75%, 90%, 95%, and two changes of 100%). Each dehydration step lasted for 15 minutes, ensuring gradual removal of water to prevent structural damage to the TiO_2 particles. After dehydration, the samples were vacuum-dried overnight. This step is critical for removing any remaining ethanol, thus preventing interference during SEM imaging. The dried samples were then mounted on double-sided conductive carbon tape. They were subsequently coated with gold using the Anatech Hummer VI sputter device (Au/Pd) for 60 seconds. Gold coating enhances the electrical conductivity of the samples, reducing charging effects and improving image quality. Finally, SEM images of the TiO_2 particles were obtained using a Hitachi HF-3300V STEHM.

Figure 31 shows TiO_2 particles alone, highlighting their size and the wide range of particle sizes. Figure 32 A and B compare the TiO_2 particles before and after incubation with the vesicles. Notably, in both images, clusters of smaller particles are observed on the surface of the TiO_2 particles. These clusters may be attributed to the dehydration process or the vesicles sitting on the surface of the particles. Since these clusters of smaller particles are observed in both pre- and post-incubation SEM images, their presence does not conclusively indicate the binding of vesicles. Consequently, we cannot ascertain their origin with certainty from these images alone. Therefore, these SEM images, while informative about the morphology and size distribution of the TiO_2 particles, do not serve as definitive proof of vesicle binding.

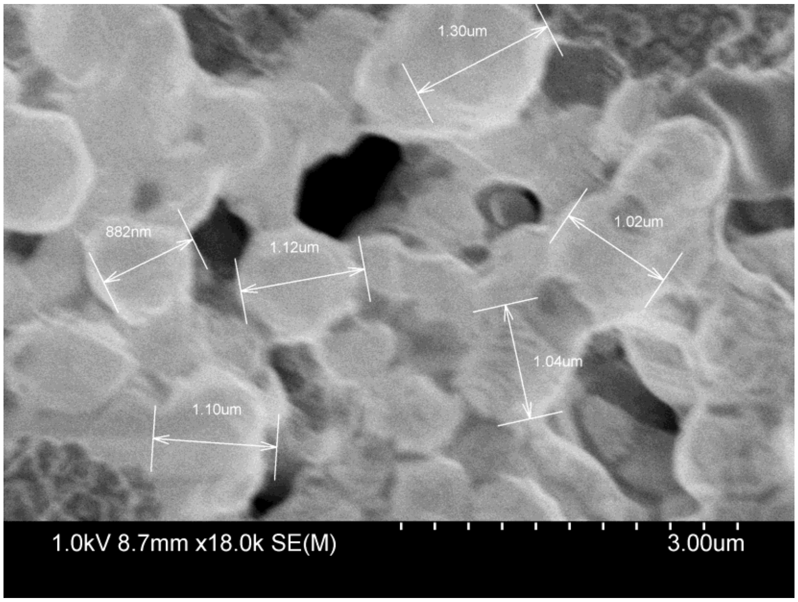

Figure 31 - SEM image of TiO_2 particles

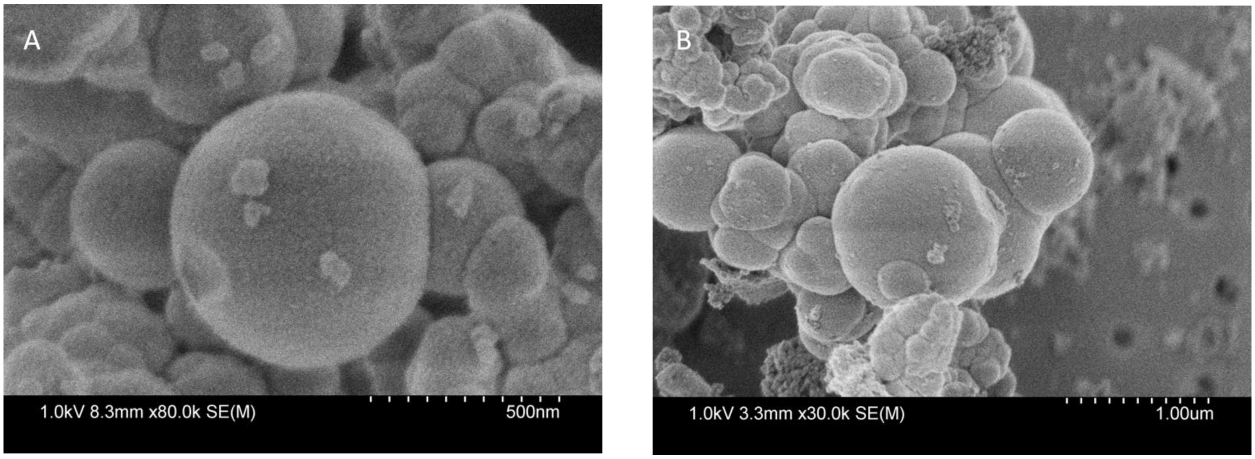

Figure 32 - SEM images comparing TiO_2 particles before and after incubation with liposomes, A: particles before incubation, B: particles after incubation

Chapter 4: Isolation of vesicles and efficiency evaluation

4.1 Isolation methodology

4.1.1 Preparation

In order to run experiments for the isolation strategy, the first step is to determine the right concentration of TiO_2 and Liposomes. Since here the liposomes are used as a surrogate for exosomes, their concentrations should be realistic to ensure the reliability of the studies. As mentioned earlier, these vesicles can be found in various body fluids, making them a valuable source of potential biomarkers for various applications. Researchers have isolated exosomes from several body fluids for studies: Blood (Plasma/Serum): One of the most commonly studied fluids because it can provide a systemic overview of what might be happening in the body. Exosomes from blood can offer insights into various conditions like cancers, cardiovascular diseases, etc. Plasma has a high exosome concentration (approximately 1–3 × 10^{12}/ml exosomes were recovered) due to its interaction with diverse cell types, its central role in signaling, and its volume. Additionally, immune responses and certain diseases can elevate exosome release into the bloodstream, further increasing their concentration in plasma [126]. Urine is the second most used source for exosome studies. Studying exosomes in urine can be particularly useful for understanding diseases related to the urinary tract, kidneys, and potentially prostate with a concentration of approximately 3–8 × 10^9 exosomes. Other sources of exosomes including saliva, which is favorable due to being non-invasive, Cerebrospinal fluid (CSF), providing information about neurological diseases and disorders, breast milk, semen, tears, etc, have a concentration falling in this range or sometimes lower concentrations. The differences in exosome concentrations across these fluids stem from the inherent nature and function of the source cells, the metabolic activities associated with each fluid type, and the roles they play in physiological processes. For example, the urinary system's primary role in waste filtration might lead to a relatively higher exosome concentration in urine, whereas the CSF, which cushions and protects the brain and spinal cord, might have a different concentration due to its specialized role in the central nervous system. The physiological status of an individual, alongside collection and processing techniques, can also influence these values [126]–[128]. As a result, the liposome sample's concentration was consistently set at 5×10^{10} throughout all experiments, to mimic the exosome concentration found in commonly used body fluids in exosome studies.

When studying the isolation of liposomes using $\mathrm{TiO_2}$ particles, the amount of $\mathrm{TiO_2}$ is crucial for several reasons, especially when considering the surface interaction between the liposomes and the $\mathrm{TiO_2}$ particles.

The amount of $\mathrm{TiO_2}$ determines the total surface area available for binding with liposomes. If there are too few $\mathrm{TiO_2}$ particles, insufficient liposomes might be captured, leading to inefficient isolation. Conversely, an excess of $\mathrm{TiO_2}$ particles might lead to other non-specific interactions or challenges in subsequent processing steps. The surface interactions between liposomes and $\mathrm{TiO_2}$ particles depend on their relative proportions. The surface ratio dictates how efficiently liposomes can interact and bind with $\mathrm{TiO_2}$. An optimal ratio ensures maximum interaction surface, leading to efficient binding and isolation. The range ratios of the surface area of titanium to liposome studied in this work was 5 to 18, these values were based on the information collected from previous publications on exosome isolation by titanium, which is given in the following paragraphs along with their calculation method [58]–[63].

Assumptions:

- $\mathrm{TiO_2}$, exosome and liposomes are spherical with $V = \frac{\pi d^3}{6}$ and $Mass = \rho V$

- Density of $\mathrm{TiO_2}$ = 4.23 g/ml for $\mathrm{TiO_2}$ density and 2.49 g/ml for magnetic $\mathrm{TiO_2}$ (based on our working particles) ((Gao et al., 2019b; Pang et al., 2020; N. Zhang, Sun, et al., 2021) have used magnetic particles)
- Density of exosome and liposome = 1.13 g/ml
- $Surafce\ concentration\ = \frac{mass\ concentration\ \times surface\ area\ of\ one\ particle}{mass\ of\ one\ particle}$
- $Number\ of\ particles\ per\ ml = \frac{mass\ concentration}{density\ \times Volume\ of\ one\ particle}$

Table 9 - Concentration of $\mathrm{TiO_2}$ and exosomes previously reported

Reference	Exosome mass or count	Sample Volume (mL)	$\mathrm{TiO_2}$ mass (mg)	$\mathrm{TiO_2}$ mass concentration (mg/mL)	Exosomes concentration (mg/mL)
[58]	2 µg	50×10^{-3}	2	40	0.04
[59]	112.5 µg	1.5	5	3.33	0.075
[60]	15 µg	10	20	2	0.0015
[61]	4×10^6	4×10^{-3}	0.8	200	10×10^9 1/ml
[62]	40 µg	1	2.5	2.5	0.04
[63]	2 µg	1	2	2.0	0.002

Table 10 The calculated surface ratio of $\mathrm{TiO_2}$ particles to exosomes based on previous reports

Reference	TiO_2 diameter (μm)	TiO_2 number concentration (1/mL)	Exosomes number concentration (1/mL)	TiO_2 concentration (cm^2/mL)	Exosomes concentration (cm^2/mL)	TiO_2/Exosomes
[58]	1.5	9.09×10^9	6.76×10^{10}	6.43×10^2	21.2	30.2
[59]	0.32	7.72×10^{10}	1.27×10^{11}	2.25×10^2	39.8	6.31
[60]	5	7.22×10^6	2.54×10^9	5.67	79.6	7.12
[61]	0.315	4.91×10^{12}	1×10^{10}	6.12×10^4	1.25	47.6
[62]	0.3	7.12×10^{10}	6.76×10^{10}	2×10^2	21.2	9.47
[63]	2	1.13×10^8	3.38×10^9	14.2	1.06	16.7

Due to the above charts, we can see that the surface concentration ratio of TiO_2 to exosomes range is 6.31-47.6 and the liposome concentration should be 2.54×10^9– 1.27×10^{11}. TiO_2 particles were prepared at concentrations ranging $1.11 \times 10^9 - 4.89 \times 10^9\ particles/ml$ (equivalent to approximately $5 - 21.5\ mg/ml$). This was achieved by diluting the purchased TiO_2 particles in DI water at room temperature, followed by thorough mixing using a vortexer. These specific concentrations were chosen to achieve a surface ratio of TiO_2 to liposomes between 5 to 22 (5,10,15,18,20 and 22).

To match the liposomes' hydration buffer, sucrose and HEPES were added to the TiO_2 solution to achieve final concentrations of 10% sucrose and 20 mM HEPES. The pH was then maintained at 7.5 ± 0.2 and adjusted using a KOH solution. Once the desired buffer conditions were set, liposomes were gently introduced to each sample, ensuring a consistent concentration of 5×10^{10} liposomes/ml down from their original concentration of approximately 4.8×10^{13} particles/ml.

Given the above values, the following equations are used to calculate the $\mathrm{TiO_2}$ and exosome sample volume required for each experiment:

- Lipid composition: DOPC/CHOL/F-DHPE (54:45:1 mol/mol) (MW of DOPC = 734.039 g/mol, CHOL =386.65 g/mol, MW of DHPE: 706.03 g/mol →MW of the lipid composition = 577.434)
- Lipid concentration: 50 mM (50-55 mM ($50^{-6}\frac{mol}{ml}$)))
- Mean particle size: 100 nm (90-120 nm)

Number of particles in 1 ml = $\text{lipid concentration} \times \text{sample volume} \times \text{MW} \times \frac{1}{\text{mass of one particle}} = 50 \times 10^{-6}\,\frac{\text{mol}}{\text{ml}} \times 1\text{ ml} \times 577.434\,\frac{\text{g}}{\text{mol}} \times \frac{1}{5.9 \times 10^{-16}} = 4.8 \times 10^{13}$

Table 11 - Properties of working particles

Particle	Mass per particle (mg)	Surface area per particle (cm^2)	Number of particles per ml	Surface area (cm^2)
1.5 um $\mathrm{TiO_2}$ (50 mg/ml)	4.39×10^{-9}	7.07×10^{-8}	1.14×10^{10}	805.866

100 nm Exosome/ Liposome (50 mM)	5.9×10^{-13}	3.14×10^{-10}	4.8×10^{13}	15072

Using the following equations, the volume required for each experiment was calculated:

Total sample Volume = $500\ \mu l$ (Constant)

Number of liposomes in each sample = $0.5\ ml \times 5 \times 10^{10}\ particles/ml$

Surface ratio of TiO_2 particles to liposomes (SR) = 5 to 18

$\text{Number of liposomes in each sample} =$

$$\text{Concentration}\left(\frac{\text{Particles}}{\text{ml}}\right) \times \text{Volume extracted from the original sample of liposome}$$

$\text{Surface area of liposomes} = \text{Number of liposomes} \times \pi \times \text{Diameter}^2$

$\text{Surface area of TiO}_2\text{ particles} = \text{SR} \times \text{Surface area of liposomes}$

$\text{Surface area of TiO}_2\text{ particles} = \text{Number of TiO}_2\text{ particles} \times \pi \times \text{Diameter}^2$

$\text{Number of TiO}_2\text{ in the experiment} =$

$$\text{Concentration}\left(\frac{\text{Particles}}{\text{ml}}\right) \times \text{Volume extracted from the original sample of TiO}_2$$

4.1.2 TiO$_2$- liposome mixing and incubation

Using the $TiO_2 -$ liposome Sample prepared in a 10% sucrose, 20 mM HEPES buffer, two methodologies of bulk and microfluidic incubation were explored and compared to ensure effective bonding between liposomes and TiO_2 particles Figure 35.

4.1.2.1 Bulk approach

In the initial series of experiments aimed at determining the initial approximate optimal concentration and incubation time range, we varied the ratio of TiO_2 particle surface area to liposome surface area, specifically exploring ratios of 5, 10, 15, and 20. As shown in Figure 5, each prepared sample was then incubated on a shaker at room temperature and 200 rpm for durations of 1, 5, 10, and 20 minutes.

These initial values were selected based on findings from our literature review, as documented in the Table 12. The stabilization time is the incubation time after which no significant change in the efficiency was observed. Subsequently, while keeping the selected incubation time and surface area ratio constant, we investigated variations in concentration to achieve surface ratios of 5, 10, 15, 18, 20, and 22. Additionally, we explored incubation times of 1, 2, 3, 5, 7, 10, 15, 20, and 25 minutes while maintaining a fixed surface area ratio. All experiments were conducted under consistent conditions on a shaker at 200 rpm.

Table 12 - Concentration of TiO_2 and incubation time previously reported

Reference	TiO_2/Exosomes	Range of Incubation Time (min)	Stabilization time	TiO_2/Exosomes
[58]	3.02E+01	1-10	5	3.02E+01
[59]	6.31E+00	1-60	10	6.31E+00
[60]	7.12E+00	1-30	-	7.12E+00
[61]	4.76E+01	1-6	5	4.76E+01

[62]	9.47E+00	-	-	9.47E+00
[63]	1.67E+01	5-20	10	1.67E+01

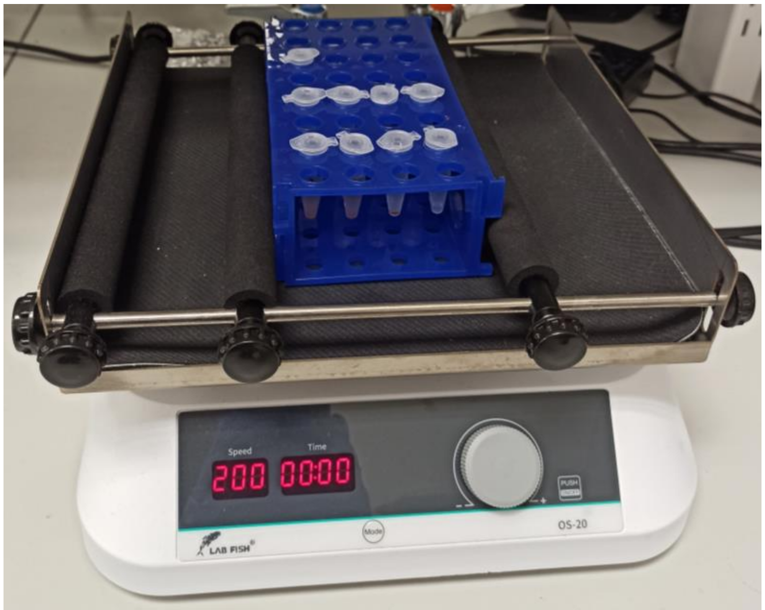

Figure 33 - Bulk Setup, mixing samples on a shaker with 200rpm

2.2.2.1.1. Microfluidic procedure

The micromixer with design 6, achieving the satisfactory mixing and incubation, was selected for the main tests. After above explained preparation of the TiO_2 and liposome mixture sample, it was introduced into two inlets of a micromixer via a dual syringe pump (Cole-Parmer®), utilizing 1 ml BD syringes. The flow rates tested included 5, 10, 20, 40, 50, 70, 100, and 1500 µl/min.

Each procedure was replicated three times to validate the reproducibility and reliability of the results. Following the incubation, the liposome-bonded TiO_2 particles were settled at the vial's bottom using a disc magnet. The supernatant, which contained any unbound liposomes, was then separated and set aside for subsequent efficiency evaluations.

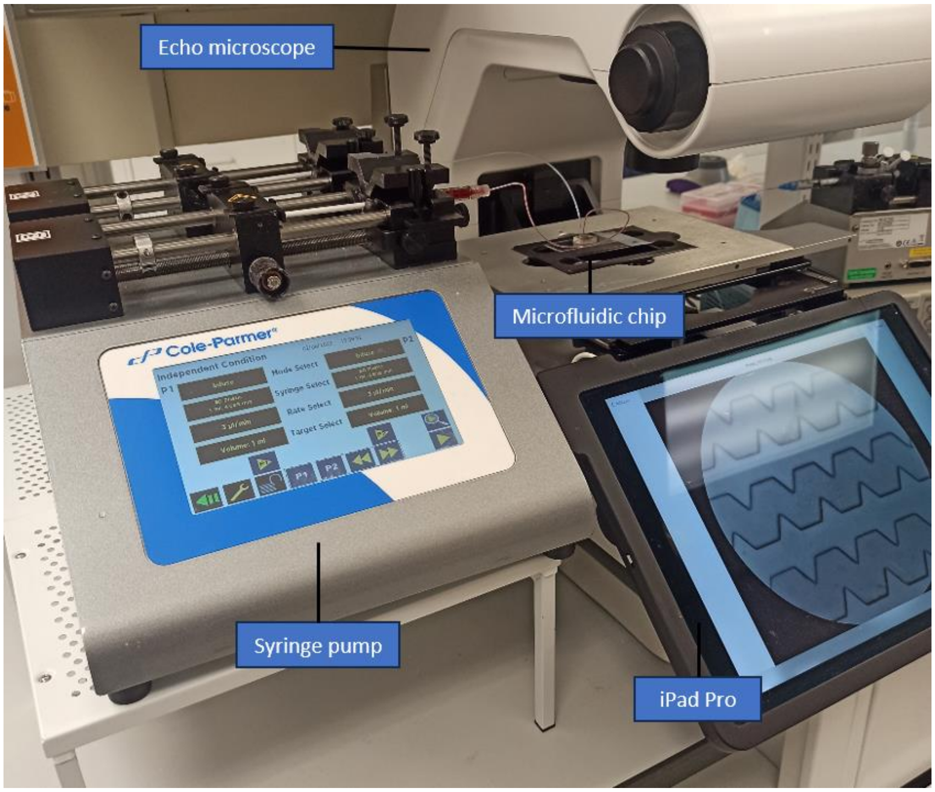

Figure 34 - Microfluidic Setup

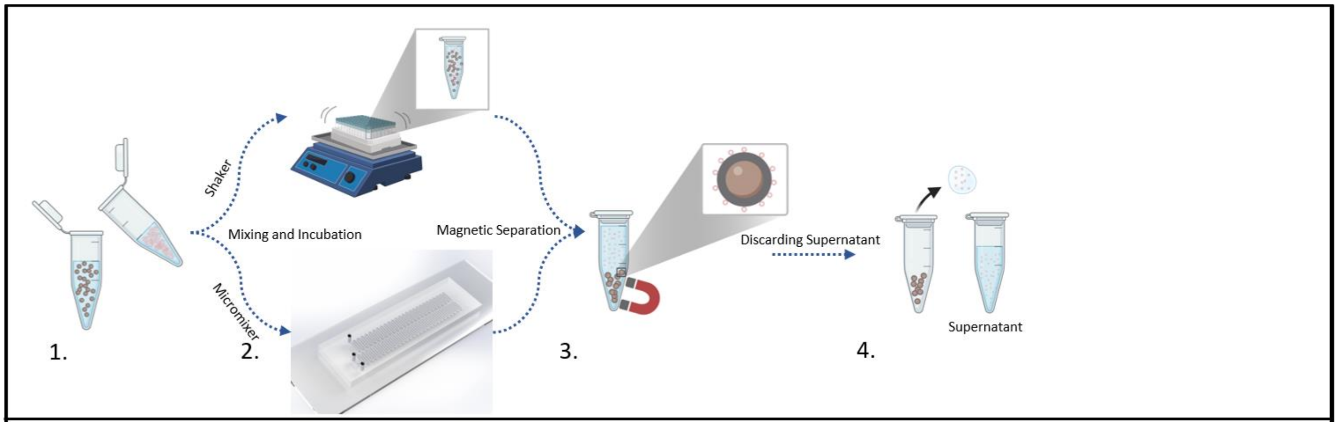

Figure 35 - Isolation experimental procedure

4.2 Efficiency evaluation

4.2.1 Methodology

Fluorescence imaging was the primary tool for determining efficiency. We determined the degree of attachment to the TiO_2 particles by comparing the initial fluorescence of the pre-processed liposome sample with the fluorescence observed in the post-processing supernatant (Figure 36).

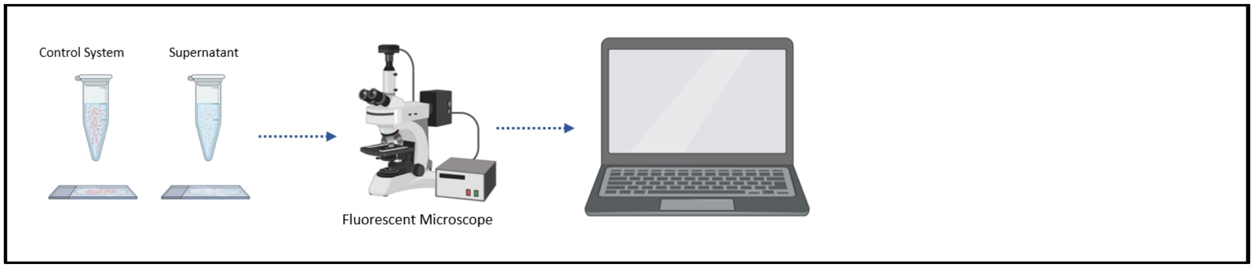

Figure 36 - Efficiency measurement

According to the literature review covering publications on TiO_2-based exosome isolation (summarized in Table 13) fluorescence imaging was used in 50% of the studies to explore exosome-TiO_2 interactions and in 33% for efficiency calculations. Also, this method is adaptable for both exosomes and liposomes, making it a suitable analytical tool for our research.

Table 13 - Review on efficiency measurement methods of TiO_2-based exosome isolation

Reference	Interaction investigation	Efficiency measurement

[58]	TEM/Fluorescence imaging	Comparison of the value of exosomal marker in western blotting analysis (extracted and total)
[59]	-	Comparison of the fluorescence intensity of dyed exosomes before incubation and the supernatant
[60]	-	greyscale value of all exosomal proteins in SDS-PAGE analysis
[61]	TEM/Fluorescence imaging	Surface-enhanced raman scattering (SERS) immunoassay
[62]	TEM/Fluorescence imaging	Comparison of the fluorescence intensity of Dyed exosomes before incubation and the supernatant
[63]	-	The exact efficiency is not reported. EV untargeted metabolomic profiling by UHPLC-QTOF-MS is used to compare the number and the abundance of metabolites with conventional methods.

For image capturing, samples were prepared by air-drying 50 μl of the sample onto standard glass slides (75 by 26 mm with a thickness of 1 mm).

To ensure accurate efficiency calculations, we initially built a calibration curve that establishes a direct relationship between fluorescence intensity and liposome concentration. This correlation enabled us to convert the grayscale values obtained from fluorescence images into concentration values. Subsequently, we employed this calibrated approach to calculate the efficiency using the following formula:

Efficiency=

$$\frac{\text{concentration of unprocessed liposome sampke (control system)} - \text{concentration of liposomes in suprnatent}}{\text{concentration of unprocessed liposome sampke (control system)}}$$

where the control system had a concentration of 5×10^{10} liposomes/ml.

For these efficiency measurements, 20 µl of the sample covered half the surface area of a standard glass slide (37.5 mm by 26 mm) and was shielded with a cover slip. Imaging specifics included the use of the TXRed channel with exposure settings at 765ms, gain level at low, and LED brightness set to 100%. A 20x magnification was employed, and to span the entire slide surface, it was divided into six sections, one image taken from each section (Figure 37). Three replicates were done to validate the reliability of the results.

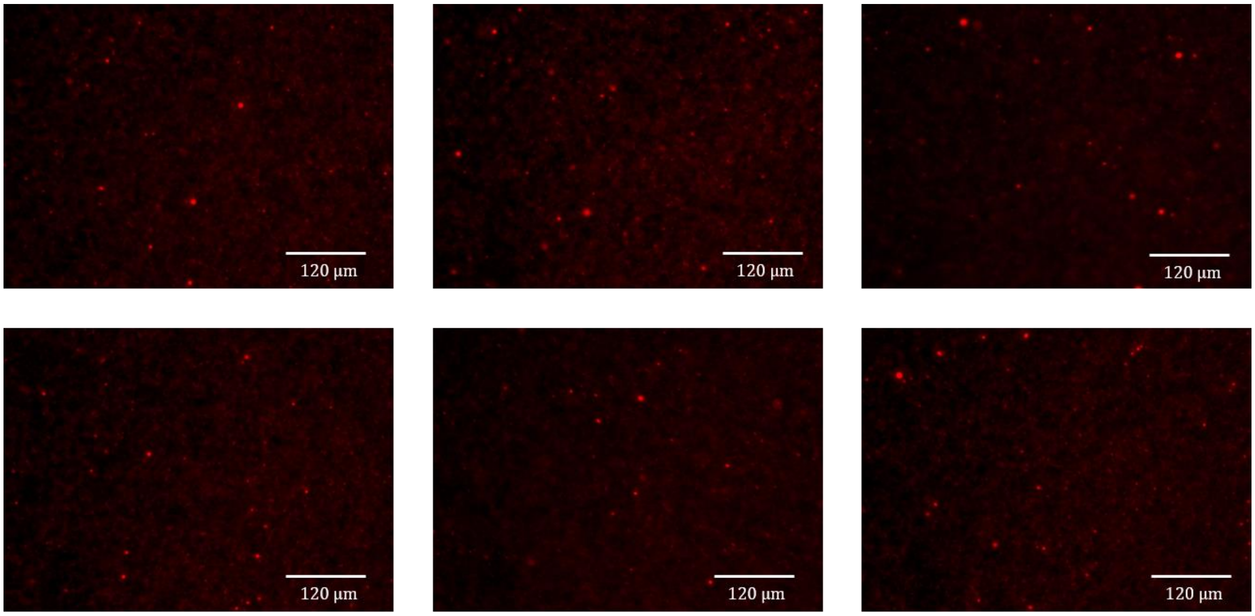

Figure 37 – Fluorescence images from one slide of sample

4.2.2 Conventional bulk approach

Defining key parameters

To evaluate the functionality of our methodology in capturing the vesicles available in the sample, we explored the impact of two major determining parameters: the amount of TiO_2 and the incubation time. The amount of TiO_2 dictates the available surface area for vesicle attachment, with greater quantities providing more binding sites and thus potentially higher adsorption capacity. Varying the amount of TiO_2 particles used in the experiment can provide insights into the capacity of TiO_2 to bind vesicles and the saturation point at which no more vesicles can be adsorbed by increasing the amount of TiO_2 particles. The incubation time (t) is the duration for which the vesicles are allowed to interact with the TiO_2 particles. The rate of exosome adsorption, as described by the kinetic models, is dependent on time. The longer the incubation time, the more time vesicles have to interact with TiO_2 particles to reach to q_e.

In this regard, we used the inherent fluorescence of our liposomes to assess the efficiency of our isolation method. The fluorescent characteristics of these liposomes enable us to monitor their presence throughout the isolation procedure. We determined the degree of attachment to the TiO_2 particles by comparing the initial fluorescence of the pre-processed liposome sample with the fluorescence observed in the post-processing supernatant (Figure 4C).

Initial factorial experimental design

As mentioned earlier, we used a constant amount of liposomes, specifically 5×10^{10}, chosen because it aligns with typical exosome concentrations found in serum, plasma, and urine samples (usually between $10^9$and 10^{12} [58]–[63], [129], [130]). In our initial experimental design, we employed a factorial approach to investigate the effects of varying the surface ratio of TiO_2

particles to liposomes (5, 10, 15, 20) and different incubation times (1, 5, 10, 20 minutes). These specific values were selected based on prior research methodologies using TiO_2, as summarized in Table 12.

As shown in the Figure 38, across all experiments conducted at a particular surface ratio and incubation time, the system eventually reaches a stabilization point. Stabilization is a limit point of time beyond which, extending the incubation time does not lead to significant improvements in efficiency. We observed that the time required for this stabilization in incubation increases as the amount of TiO_2 particles is raised. In other words, the time it takes for the system to stabilize during incubation increases as you use more TiO2 particles. For example, at a surface ratio of 5, it takes 5 minutes to stabilize, but at higher TiO2 concentrations, it takes 10 minutes for the system to stabilize. The better results were seen in the concentration range of 15 to 20, and once the incubation time reached 10 minutes, the efficiencies across all concentrations remained relatively stable with only minor variations.

In response to the observed trends, for subsequent experiments, we held the incubation time constant at 10 minutes and continued the experiments by adjusting the quantity of TiO_2 particles more precisely in the surface area ratio range around 15 to 20. This involved using surface ratios of 5, 10, 15, 18, 20, and 22 to gather more detailed data.

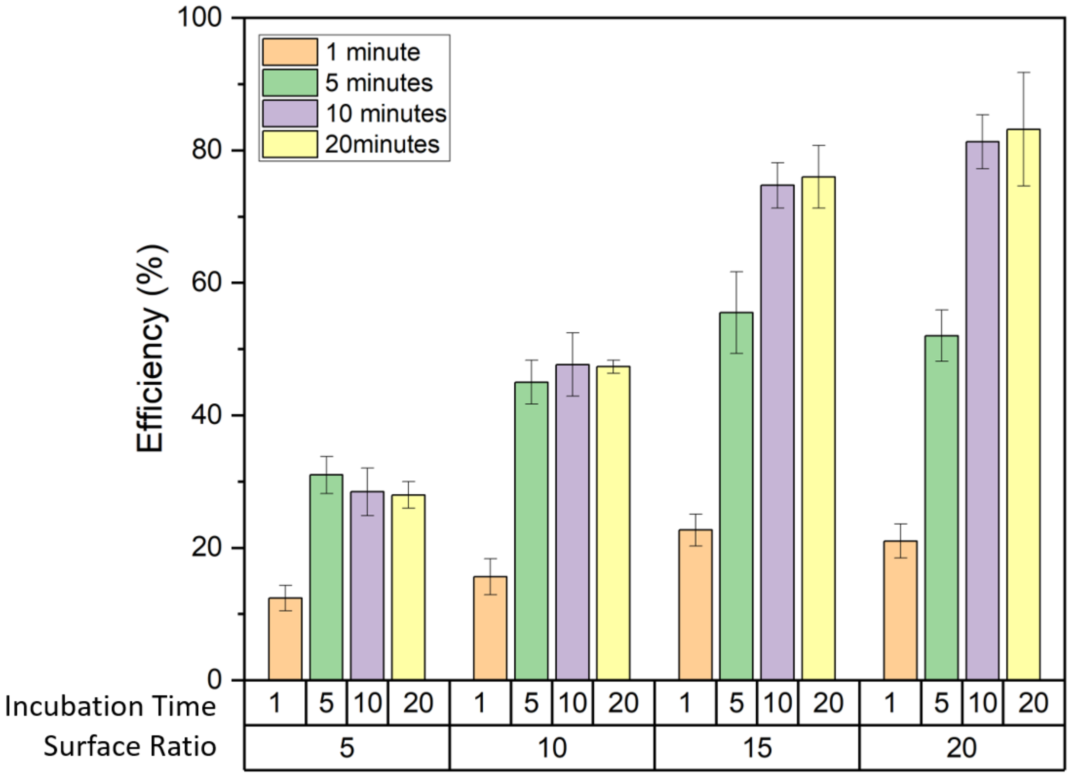

Figure 38 - Efficiency trends at different surface ratios and incubation times

Optimizing surface ratio

With a clear understanding of the influential factors gained from our Factorial Experimental Design, we now move forward into the phase of Optimizing Surface Ratio. We have chosen to first maintain a constant incubation time of 10 minutes and focus on the trend of efficiency by tuning the quantity of TiO_2 particles varying the surface ratios to 5, 10, 15, 18, 20, and 22.

As the surface ratio increased from 5 to 18 (for a 10-minute incubation), the efficiency also increased, reaching a peak of 84.3% (Figure 39). The higher quantity of TiO_2 resulted in a larger surface area, offering more potential binding sites and improved adsorption efficiency. However, exceeding this ratio led to a decrease in efficiency. This decline can be interpreted as resulting from two factors. Firstly, an excessive amount of TiO_2 could obstruct mixing, where the proximity of TiO_2 particles make it challenging for liposomes to access the binding sites. Secondly, higher quantities of TiO_2 might cause particle agglomeration because when there is an excessive amount of TiO_2 present, the particles can come into closeness to each other, leading to attractive forces between them.

The attractive forces between particles can lead to the particles sticking together or forming aggregates. When this happens, the total surface area available for adsorption (the process where substances adhere to the particle surface) decreases. This reduction in surface area can potentially hinder the adsorption process. When we have a higher quantity of TiO_2 particles, it is more likely for particle agglomeration (clumping or grouping of particles) to occur. As with the previous point, this agglomeration reduces the surface area available for adsorption, and as a result, it can potentially impede or hinder the adsorption process. Therefore, by considering these facts, we selected a surface ratio of 18 as an optimal ratio for further examination of the optimal incubation time.

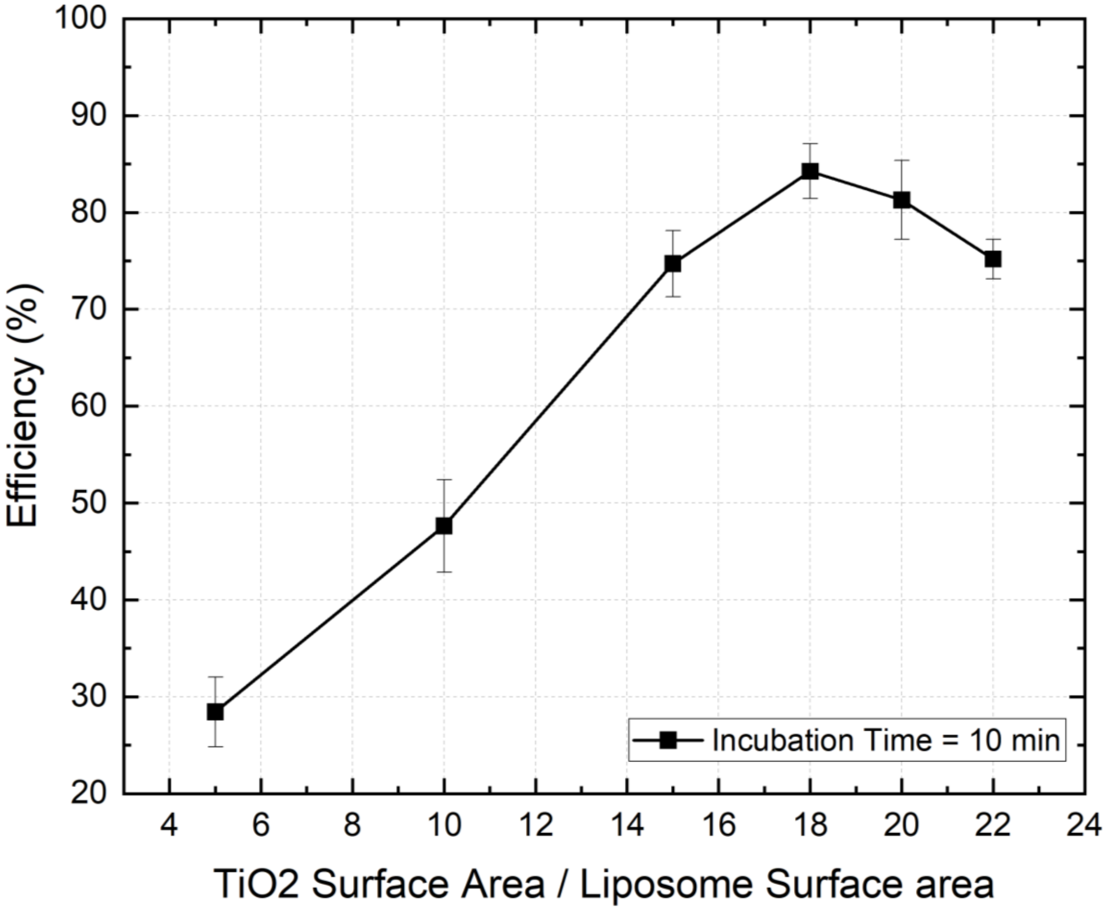

Figure 39 - Efficiency across various surface ratios (incubation time: 10 minutes)

Effect of incubation time

To see the relationship between incubation time and efficiency we fixed the surface ratio at 18. As shown in Figure 40, by extending the incubation time from 1 minute to 10 minutes, the isolation efficiency increased from 20.4% to 84.25%. This initial rise in efficiency is likely attributed to the fact that, during this period, the liposomes had enough time to interact with TiO_2 particles, occupying a significant portion of the available binding sites. When we further extended the incubation time from 10 minutes to 25 minutes, we observed only slight fluctuations, indicating that the initial 10 minutes were necessary to reach a saturation point in available binding sites.

Moreover, the observed stability and minor efficiency fluctuations beyond the initial 10 minutes, up to the maximum 25-minute duration, suggest the establishment of an equilibrium state and potential saturation of the TiO_2 surface. In this equilibrium state, additional exposure time seems to have limited impact on the binding process.

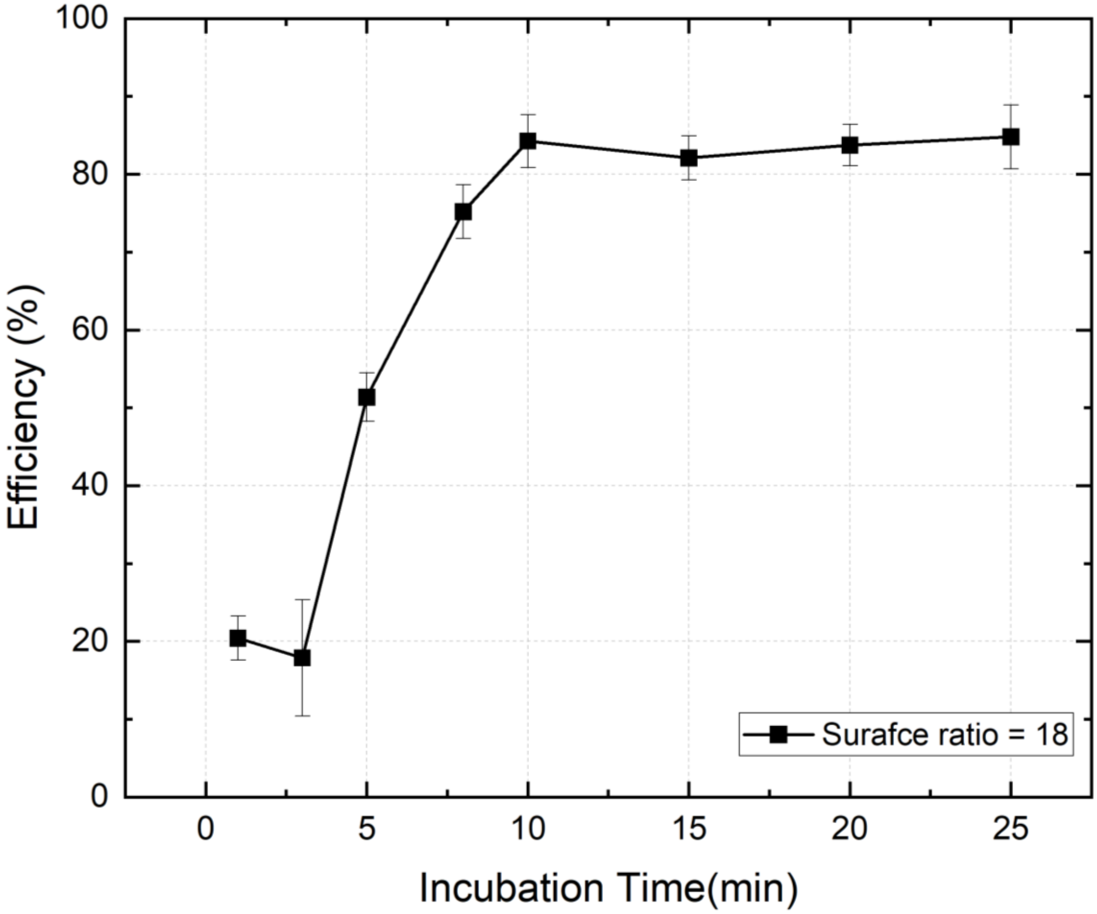

Figure 40 - Efficiency across various incubation times with a surface ratio of 18

4.2.3 Microfluidic approach

Here, we utilize the optimized conditions obtained in the previous sections to assess the effectiveness of our methodology, which involves substituting conventional bulk incubation with a microfluidic setup. The final design of micromixer discussed in Micromixer selection section (shown in Figure 20) has proven to be highly effective, in a wide range of Reynolds numbers, representative of various flow rates—both low and high. This versatility allows us to thoroughly investigate the performance of our setup for capturing liposomes using TiO_2 particles under diverse flow rate conditions, each utilizing distinct mixing mechanisms, each with its unique set of advantages and disadvantages. The results of the incubation experiments in our micromixer conducted with the mixture of TiO_2 particles and liposomes as the working sample, with a surface ratio of 18 (optimized in the Conventional bulk approach section), under varying flow rates, are presented in the Figure 41.

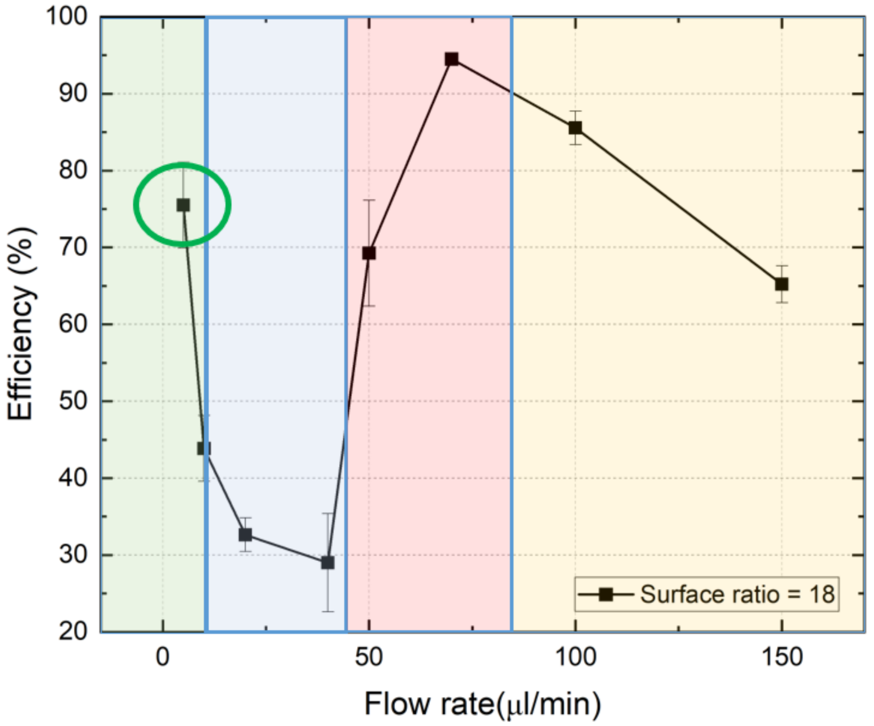

- ● High efficiency: Low flow rate (High diffusion) and high incubation time
- ● Decrease: Medium flow rate (Low diffusion and convection)
- ● Increase: High flow rate (Secondary flows and High convection)
- ● Decrease: Insufficient incubation time due to high flow rate

Figure 41 - Efficiency of microfluidic approach across various flow rates with a surface ratio of 18

In this graph we see that at low, 5 $\mu l/min$ and, high, 70 $\mu l/min$ flow rates, two peaks of high isolation efficiency were observed. This is attributed to two primary mixing mechanisms: diffusion at low (Around Re = 1) and convection at higher Reynolds numbers (Around Re = 10). During the flow rate transition period, as diffusion diminishes and convection isn't potent enough for optimal mixing, there's a decrease in efficiency between flow rates of 10 and 40 $\mu l/min$, which then rises again between 40 and 70 $\mu l/min$. At lower flow rates with parallel streamlines, mixing primarily depends on diffusion, leading to a gradual process where complete mixing is only achieved later in the channel. However, due to the low flow velocity, even when mixing occurs close to the channel's end, there is still ample time for incubation. In contrast, at higher flow rates, chaotic advection comes into play, introducing unpredictability and complexity through the creation of intricate, irregular streamlines within the flow. This occurs even within the laminar regime with specialized design of micromixers. Chaotic advection accelerates mixing, allowing it to occur earlier in the channel. Owing to the channel's length and design, samples still benefit from ample incubation time, even at these higher velocities.

Another observed trend was a decrease in efficiency after a flow rate of $70\ \mu l/min$. This is likely because, although high mixing efficiency is achieved for flow rates above $70\ \mu l/min$, there is insufficient time for effective interaction between liposomes and $\mathrm{TiO_2}$ particles due to the high flow speed.

A summary of our discussion is presented in the Table 14. It's important to note that we measured the viscosity of the samples using a viscometer, and because their viscosity values closely resembled that of water, we used the viscosity of water to calculate the Reynolds number. Similarly, the density of the samples closely matched that of water, so we used the density of water for our calculations as well. The velocity is determined for each flow rate by taking into account the dimensions of the channel, with an average width of 200 μm and a height of 100 μm.

$Re = \frac{\rho V D_h}{\mu}$ where:

ρ is density

μ is viscosity

V is velocity = $\frac{Q}{HW}$

D_h is Hydraulic Diameter = $\frac{4WH}{2\,(W+H)}$

Table 14 - Summary of efficiency trends in microfluidic approach

Flow rate range ($\mu l/min$)	5	10-40	50-70	>100
Reynolds number	0.55	1.11-4.44.	5.55-7.76	>11.1
Trend in efficiency	75.496	$\downarrow 43.87 - 29.0$	$\uparrow$ 69.25-94.49	$\downarrow 85.56 - 65.22$

4.2.4 Comparison of bulk and microfluidic approach

When comparing the results between bulk and microfluidic experiments Table 15, the microfluidic approach demonstrated superior performance with an efficiency of 94.49%, surpassing the peak efficiency of 84.3% achieved by the bulk method. Additionally, the assay time for preparing a 500μl sample decreased from 10 minutes to just 3.5 minutes.

Table 15 - Performance comparison of bulk and microfluidic approach at optimized conditions

	Conditions	Efficiency	Assay time for 500μl sample
Bulk approach	Surface ratio = 18 Incubation time = 10 min	84.3%	10 minutes
Microfluidic approach	Surface ratio = 18 Flow rate = $70\ \mu l/min$	94.49%	3.5 minutes

Chapter 5: Release of vesicles and integrity preservation and yield evaluation

5.1 Release methodology (elution)

To release the liposomes attached to the TiO_2particle surface, an NH_3H_2O alkaline buffer (the concentrated ammonium hydroxide 28% was purchased from Anachemia) is employed [131]. The liposome-bonded TiO_2 particles are first incubated with this buffer for 10 minutes at room temperature on a shaker, maximizing elution. After incubation, it's essential to rapidly replace the alkaline buffer with the primary hydration buffer. This step involves separating the magnetic TiO_2 particles from the supernatant, which contains the released liposomes using a N42 neodymium disc magnet (MagnetShop.com). This grade 42 magnet, made from an alloy comprising neodymium, iron, and boron. The magnet is plated with a triple layer of Ni-Cu-Ni (Nickel-Copper-Nickel), measuring 1/10" in diameter and 1/8" in thickness and with an approximate pull force of 1 lb. (0.5 kg) (Figure 42).

The supernatant is then transferred to a centrifugal filter system. Microcon-30kDa centrifugal filter with ultracel-30 membrane, volume of 0.5 ml and minimum final concentrate volume of 50 $\mu l$was purchased from MilliporeSigma was used.

. During each centrifugation cycle at 4500 g for 6 minutes, hydration buffer is introduced into the filter compartment, diluting the NH_3H_2O. This sequence is repeated several times to ensure the sample is thoroughly rinsed. The residual sample in the filter is preserved for subsequent studies (Figure 43).

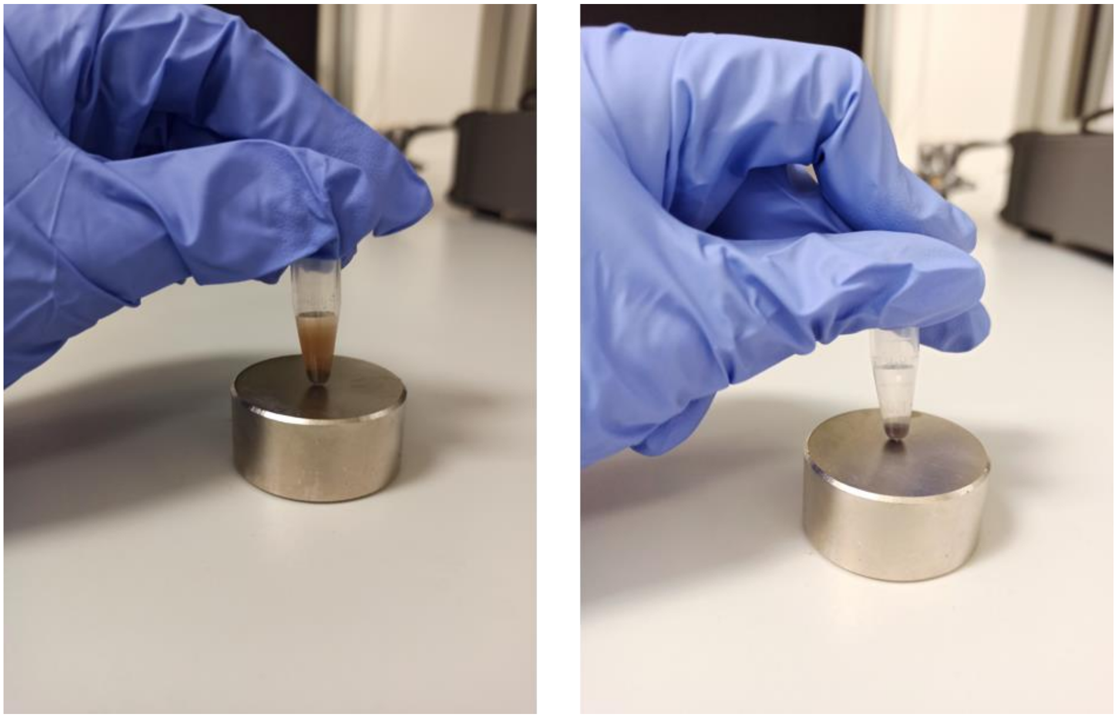

Figure 42 - Magnetically separation

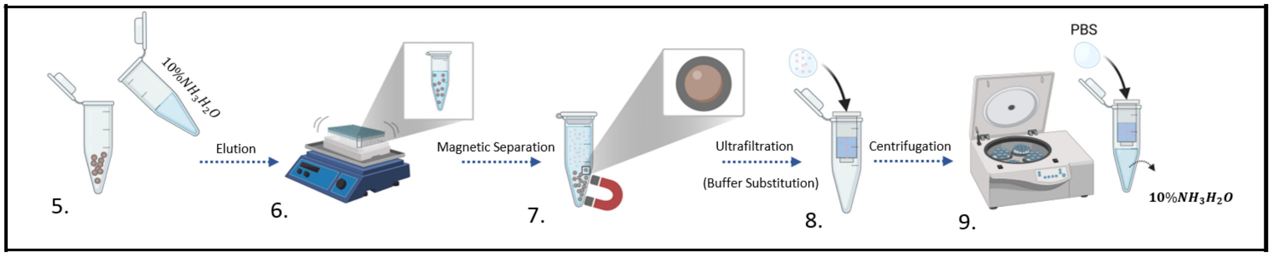

Figure 43 - Elution experimental procedure

5.2 Integrity preservation and yield evaluation

Isolated exosome characteristics are essential for various applications. One notable example is in the field of cancer research, where exosome size has been reported as a distinguishing factor [99]. Exosome size also plays a critical role in their ability to efficiently deliver therapeutic payloads to specific target tissues [132]. To ensure the reliability of our methodology and its minimal impact on the integrity of vesicles, we employed liposomes as a model system for study. Liposomes, being artificial and allowing for pre-measurements, provided a valuable means to investigate isolation effects on the size and recovery of isolated particles. This understanding is crucial for optimizing exosome-based therapies and other applications.

Here, we aim to assess the performance of our isolation methodology in preserving the integrity of the captured liposomes. To achieve this, we started with an elution step, breaking the bond between TiO_2 and liposomes using an alkaline buffer, magnetically separating the TiO_2 particles from the released liposomes, and subsequently replacing the buffer with a hydration buffer via centrifugal filtration (as depicted in the Figure 4b). In our initial evaluation, we conducted size distribution measurements on both the output samples obtained from the bulk and microfluidic approaches (with three replicates), each conducted in optimized conditions outlined in Table 16, and compared them to the preprocessed control sample (the original sample is prepared just by diluting the purchased liposome sample).

The results illustrated in the Figure 44 reveal that the TiO_2-based isolation method has not significantly altered the size distribution of particles. The modal diameter of the original sample, which measures 108 nm, remains almost the same with minimal change in both the isolated samples from both approaches. While there is a marginal 7.2% increase in the average size of the liposomes, this can likely be attributed to the rupture of a few liposomes and their subsequent reassembly into larger structures. However, this difference is minimal and may even fall within the margin of measurement error. These findings underscore the method's reliability for exosome isolation.

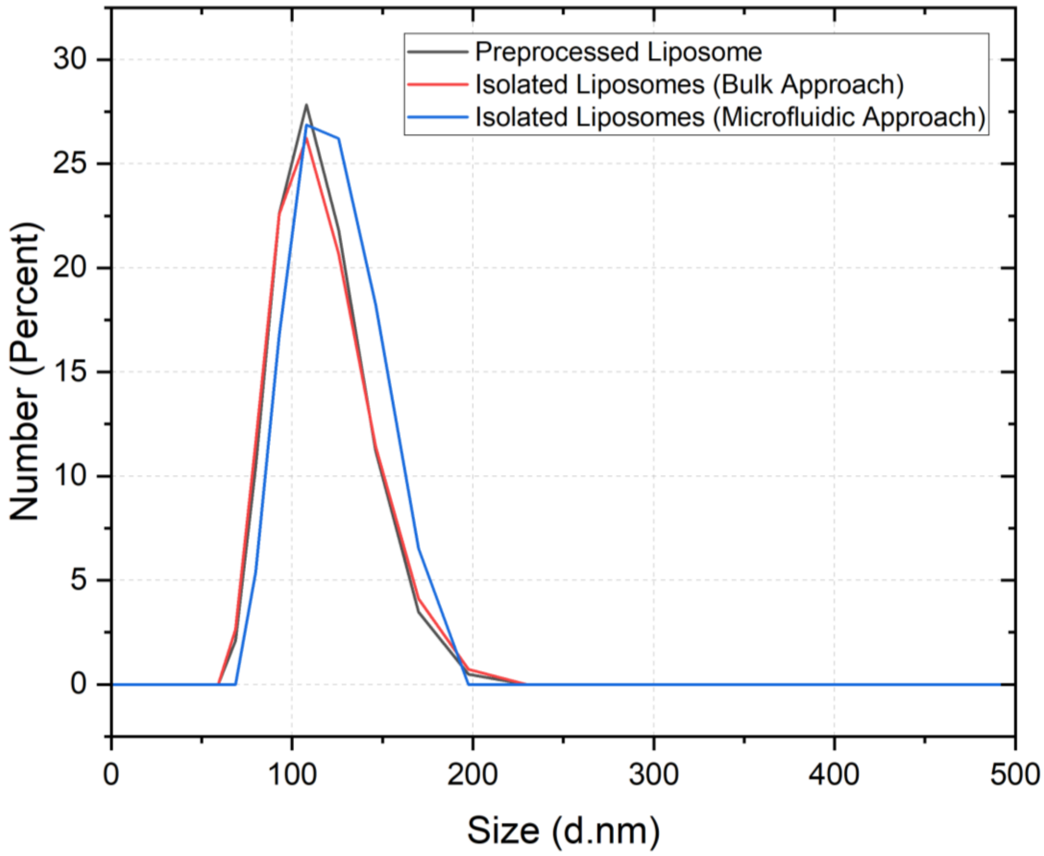

Figure 44 - Size distribution comparison of preprocessed and isolated liposomes

Table 16 - Size distribution comparison of preprocessed and isolated liposomes

	Preprocessed liposome	Isolated liposome (bulk approach)	Isolated liposome (microfluidic approach)
Modal diameter (nm)	108. 62 ± 15.2	110.49± 21.41	109 ± 22.68
Mean diameter (nm)	111.53± 21.8	111.46± 16.92	119.55± 18.17

Change in modal (%)	-	1.73 ± 3.85	0.34± 4.33
Change in mean (%)	-	-0.056 ± 4.03	7.2 ± 3.34

In our next step, our goal was to confirm whether the absence of smaller particles, which could result from particle rupture, was a consequence of losses during the filtration process. To do this, we compared the number of isolated released particles after washing with the number of captured liposomes before washing from the surface of TiO_2, as shown in (Figure 45).

In the optimized conditions, the initial quantity of liposomes bound to TiO_2 particles during the mixing process was 4.72 × 10^{10} in the microfluidic approach and 4.21 × 10^{10} in the bulk approach. After washing, the numbers reduced to 3.99 × 10^{10} and 3.71 × 10^{10}, respectively, indicating a recovery rate of 84.5% and 88.12%. This represents a 45% improvement compared to the 33% recovery rate reported for the conventional ultracentrifuge method [133].

It's worth noting that during the centrifugation filtration process, there is a possibility of some sample loss at each stage, which can affect the final results for both approaches. Another reason for the microfluidic approach can also be the adhesion of a portion of TiO_2 particles loaded with liposomes to the edges and walls of the micromixer.

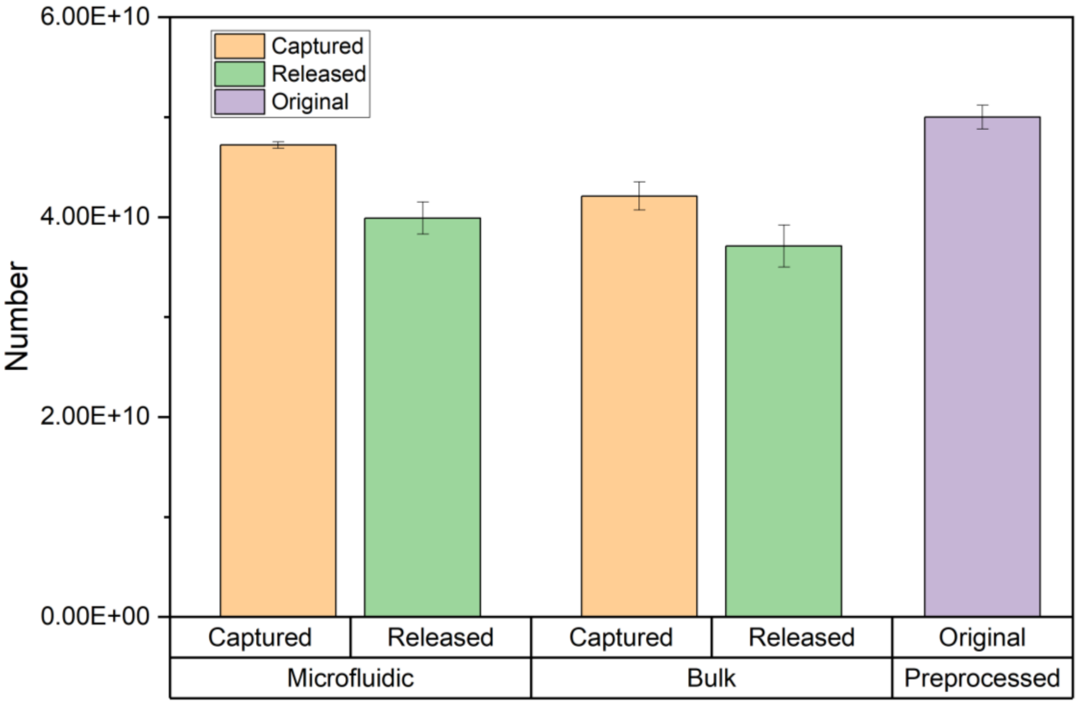

Figure 45 – Recovery rate analysis

Chapter 6: Conclusion

6.1 Summary

In our investigation, we have demonstrated the potential of the TiO_2-based isolation method in the world of exosome research and applications. To simulate exosomes, we employed liposomes, artificial vesicles with characteristics similar to exosomes, providing a controlled and pre-measured model system.

The characterization of TiO_2-liposome interaction revealed successful binding, supported by fluorescence emission and shifts in zeta potential. The size distribution analysis indicated complex formation due to liposome binding.

Evaluating the efficiency of isolation, we found that optimizing the ratio of TiO_2 surface area to liposome surface area, along with incubation time, significantly improved isolation efficiency in conventional bulk incubation, which brought about an efficiency of 88.3% in 10 minutes. The microfluidic approach emerged as particularly effective, achieving an efficiency of 93.4% and reducing assay time to just 3.5 minutes.

Importantly, our study employed liposomes as a model system to ensure the reliability of the isolation method and its minimal impact on vesicle integrity. Results confirmed minimal alteration in size distribution, highlighting the method's reliability. Furthermore, the recovery rate of isolated particles was notably improved compared to conventional methods, emphasizing the clinical relevance of this approach.

This work presents a promising TiO_2-based isolation method, particularly when implemented through microfluidic devices, as an efficient and time-saving approach for exosome isolation. The use of liposomes as a model system not only ensured the reliability of the method but also provided valuable insights into isolation effects on particle size and recovery. This research contributes to advancing exosome-related studies and opens doors to enhanced clinical applications and therapeutic strategies.

6.2 Contribution

To date, exosomes have found applications in various domains, including early disease detection and targeted drug delivery, thanks to the invaluable cargos thy carry and information they offer. Research on exosomes has paved the way for developing these applications and their associated methodologies. The isolation of exosomes serves as the foundational step for conducting such research, underscoring the utmost importance of developing efficient and user-friendly exosome isolation methods.

This study's primary contribution lies in advancing this field. Specifically, we took advantage of the potential of a microfluidic platform, a departure from conventional approaches, which not only reduces sample consumption but also treats fragile exosome samples more gently. Our work demonstrates the enhanced effectiveness of this methodology compared to bulk approaches. Additionally, by introducing a novel approach involving the use of liposome models as substitutes for exosomes in the early stages of methodology development, we've shown their suitability owing to their similarities. This innovative approach for early steps of any exosome research simplifies related research, making it more cost-effective and faster, thereby making advancements in exosome studies.

6.3 Future work

In the future work for this study, several crucial steps can be undertaken to enhance the relevance and applicability of our methodology:

- **Enhancing Sample Similarity:** The initial step should involve working with samples more closely resembling real exosome-containing biofluids. One approach is to incorporate liposome samples spiked within a serum-free media, mimicking the composition of unpurified biofluids such as serum, which contain various components other than exosomes [133]. Subsequently, the transition can be made to purified exosomes, optimizing the setup and employing suitable characterization techniques compatible with exosomes (as outlined in Table 10). Finally, the project can progress to handling unpurified exosome samples derived from sources like serum or filtered urine.

- **Integrating On-Chip Characterizations:** Shifting the working sample to exosomes may broaden the options for the characterization techniques. Alternate methods such as the analysis of exosomal markers or proteins using techniques like western blotting analysis or SDS-PAGE analysis, as well as Surface-Enhanced Raman Scattering (SERS), can be explored (Table 13). These techniques could potentially be integrated into a device or utilized for on-chip analysis.

Addressing Sample Loss: Another problem that can be tackled in future work lies in reduction sample loss caused by adhesion to the micromixer's walls and corners in the microfluidic setup. Investigating and implementing appropriate coatings on micromixer surfaces is a viable solution worth consideration and exploration.

[1] S. W. Ferguson and J. Nguyen, “Exosomes as therapeutics: the implications of molecular composition and exosomal heterogeneity,” *Journal of Controlled Release*, vol. 228, pp. 179–190, 2016.

[2] H. Shao, H. Im, C. M. Castro, X. Breakefield, R. Weissleder, and H. Lee, “New technologies for analysis of extracellular vesicles,” *Chem Rev*, vol. 118, no. 4, pp. 1917–1950, 2018.

[3] R. A. Dragovic *et al.*, “Sizing and phenotyping of cellular vesicles using Nanoparticle Tracking Analysis,” *Nanomedicine*, vol. 7, no. 6, pp. 780–788, Dec. 2011, doi: 10.1016/J.NANO.2011.04.003.

[4] E. Van Der Pol, A. G. Hoekstra, A. Sturk, C. Otto, T. G. Van Leeuwen, and R. Nieuwland, “Optical and non-optical methods for detection and characterization of microparticles and exosomes,” *Journal of Thrombosis and Haemostasis*, vol. 8, no. 12, pp. 2596–2607, Dec. 2010, doi: 10.1111/J.1538-7836.2010.04074.X.

[5] J. L. A. N. Murk *et al.*, “Endosomal compartmentalization in three dimensions: Implications for membrane fusion,” *Proc Natl Acad Sci U S A*, vol. 100, no. 23, pp. 13332–13337, Nov. 2003, doi: 10.1073/PNAS.2232379100/SUPPL_FILE/2379MOVIE2.MOV.

[6] B. T. Pan and R. M. Johnstone, “Fate of the transferrin receptor during maturation of sheep reticulocytes in vitro: Selective externalization of the receptor,” *Cell*, vol. 33, no. 3, pp. 967–978, Jul. 1983, doi: 10.1016/0092-8674(83)90040-5.

[7] P. Zhang *et al.*, “Ultrasensitive detection of circulating exosomes with a 3D-nanopatterned microfluidic chip,” *Nature Biomedical Engineering 2019 3:6*, vol. 3, no. 6, pp. 438–451, Feb. 2019, doi: 10.1038/s41551-019-0356-9.

[8] G. Raposo and W. Stoorvogel, “Extracellular vesicles: Exosomes, microvesicles, and friends,” *Journal of Cell Biology*, vol. 200, no. 4, pp. 373–383, Feb. 2013, doi: 10.1083/JCB.201211138.

[9] Y. Lee, S. El Andaloussi, and M. J. A. Wood, “Exosomes and microvesicles: extracellular vesicles for genetic information transfer and gene therapy,” *Hum Mol Genet*, vol. 21, no. R1, pp. R125–R134, Oct. 2012, doi: 10.1093/HMG/DDS317.

[10] S. Keller, M. P. Sanderson, A. Stoeck, and P. Altevogt, “Exosomes: From biogenesis and secretion to biological function,” *Immunol Lett*, vol. 107, no. 2, pp. 102–108, Nov. 2006, doi: 10.1016/J.IMLET.2006.09.005.

[11] W. Möbius *et al.*, “Immunoelectron microscopic localization of cholesterol using biotinylated and non-cytolytic perfringolysin O,” *Journal of Histochemistry and Cytochemistry*, vol. 50, no. 1, pp. 43–55, Jan. 2002, doi: 10.1177/002215540205000105/ASSET/IMAGES/LARGE/10.1177_002215540205000105-FIG5.JPEG.

[12] C. Raiborg and H. Stenmark, “The ESCRT machinery in endosomal sorting of ubiquitylated membrane proteins,” *Nature 2009 458:7237*, vol. 458, no. 7237, pp. 445–452, Mar. 2009, doi: 10.1038/nature07961.

[13] L. Urbanelli *et al.*, “Signaling Pathways in Exosomes Biogenesis, Secretion and Fate,” *Genes 2013, Vol. 4, Pages 152-170*, vol. 4, no. 2, pp. 152–170, Mar. 2013, doi: 10.3390/GENES4020152.

[14] C. Rajagopal and K. B. Harikumar, “The origin and functions of exosomes in cancer,” *Front Oncol*, vol. 8, no. MAR, p. 313913, Mar. 2018, doi: 10.3389/FONC.2018.00066/BIBTEX.

[15] M. Record, K. Carayon, M. Poirot, and S. Silvente-Poirot, “Exosomes as new vesicular lipid transporters involved in cell–cell communication and various pathophysiologies,” *Biochimica et Biophysica Acta (BBA) - Molecular and Cell Biology of Lipids*, vol. 1841, no. 1, pp. 108–120, Jan. 2014, doi: 10.1016/J.BBALIP.2013.10.004.

[16] S. Kamerkar *et al.*, “Exosomes facilitate therapeutic targeting of oncogenic KRAS in pancreatic cancer,” *Nature 2017 546:7659*, vol. 546, no. 7659, pp. 498–503, Jun. 2017, doi: 10.1038/nature22341.

[17] M. Groot and H. Lee, “Sorting Mechanisms for MicroRNAs into Extracellular Vesicles and Their Associated Diseases,” *Cells 2020, Vol. 9, Page 1044*, vol. 9, no. 4, p. 1044, Apr. 2020, doi: 10.3390/CELLS9041044.

[18] J. Chen *et al.*, “Review on Strategies and Technologies for Exosome Isolation and Purification,” *Front Bioeng Biotechnol*, vol. 9, p. 811971, Jan. 2022, doi: 10.3389/FBIOE.2021.811971/BIBTEX.

[19] C. Wittekind and M. Neid, “Cancer invasion and metastasis,” *Oncology*, vol. 69 Suppl 1, no. SUPPL. 1, pp. 14–16, 2005, doi: 10.1159/000086626.

[20] R. Kalluri and V. S. LeBleu, “The biology, function, and biomedical applications of exosomes,” *Science*, vol. 367, no. 6478, Feb. 2020, doi: 10.1126/SCIENCE.AAU6977.

[21] E. P. Diamandis, “The failure of protein cancer biomarkers to reach the clinic: why, and what can be done to address the problem?,” *BMC Med*, vol. 10, p. 87, Aug. 2012, doi: 10.1186/1741-7015-10-87.

[22] K. L. Schey, J. M. Luther, and K. L. Rose, “Proteomics characterization of exosome cargo,” *Methods*, vol. 87, pp. 75–82, Oct. 2015, doi: 10.1016/J.YMETH.2015.03.018.

[23] X. Wang, L. Tian, J. Lu, and I. O. L. Ng, “Exosomes and cancer - Diagnostic and prognostic biomarkers and therapeutic vehicle,” *Oncogenesis 2022 11:1*, vol. 11, no. 1, pp. 1–12, Sep. 2022, doi: 10.1038/s41389-022-00431-5.

[24] X. Wang, J. Huang, W. Chen, G. Li, Z. Li, and J. Lei, “The updated role of exosomal proteins in the diagnosis, prognosis, and treatment of cancer,” *Experimental & Molecular Medicine 2022 54:9*, vol. 54, no. 9, pp. 1390–1400, Sep. 2022, doi: 10.1038/s12276-022-00855-4.

[25] Y. Zhang, J. Bi, J. Huang, Y. Tang, S. Du, and P. Li, “Exosome: A review of its classification, isolation techniques, storage, diagnostic and targeted therapy applications,” *Int J Nanomedicine*, vol. 15, pp. 6917–6934, 2020, doi: 10.2147/IJN.S264498.

[26] G. K. Wang *et al.*, “Circulating microRNA: a novel potential biomarker for early diagnosis of acute myocardial infarction in humans,” *Eur Heart J*, vol. 31, no. 6, pp. 659–666, Mar. 2010, doi: 10.1093/EURHEARTJ/EHQ013.

[27] M. F. Corsten *et al.*, “Circulating MicroRNA-208b and MicroRNA-499 Reflect Myocardial Damage in Cardiovascular Disease,” *Circ Cardiovasc Genet*, vol. 3, no. 6, pp. 499–506, Dec. 2010, doi: 10.1161/CIRCGENETICS.110.957415.

[28] X. Dong, X. Gao, Y. Dai, N. Ran, and H. F. Yin, “Serum exosomes can restore cellular function in vitro and be used for diagnosis in dysferlinopathy,” *Theranostics*, vol. 8, no. 5, p. 1243, 2018, doi: 10.7150/THNO.22856.

[29] L. J. Vella, A. F. Hill, and L. Cheng, “Focus on Extracellular Vesicles: Exosomes and Their Role in Protein Trafficking and Biomarker Potential in Alzheimer’s and Parkinson’s Disease,” *International Journal of Molecular Sciences 2016, Vol. 17, Page 173*, vol. 17, no. 2, p. 173, Feb. 2016, doi: 10.3390/IJMS17020173.

[30] S. V. Yelamanchili *et al.*, “MiR-21 in Extracellular Vesicles Leads to Neurotoxicity via TLR7 Signaling in SIV Neurological Disease,” *PLoS Pathog*, vol. 11, no. 7, p. e1005032, Jul. 2015, doi: 10.1371/JOURNAL.PPAT.1005032.

[31] Z. Liu, Z. Yang, and L. He, “Effect of miR-29a-3p in exosomes on glioma cells by regulating the PI3K/AKT/HIF-1α pathway,” *Mol Med Rep*, vol. 27, no. 3, Mar. 2023, doi: 10.3892/MMR.2023.12959.

[32] A. D. Pusic and R. P. Kraig, “Youth and environmental enrichment generate serum exosomes containing miR-219 that promote CNS myelination,” *Glia*, vol. 62, no. 2, pp. 284–299, Feb. 2014, doi: 10.1002/GLIA.22606.

[33] E. J. Goetzl *et al.*, “Low neural exosomal levels of cellular survival factors in Alzheimer’s disease,” *Ann Clin Transl Neurol*, vol. 2, no. 7, pp. 769–773, Jul. 2015, doi: 10.1002/ACN3.211.

[34] L. Yang, H. Wu, Y. Zhu, X. Chen, and Y. Chen, “Plasma exosomal caveolin-1 predicts Poor Prognosis in Ovarian Cancer,” *J Cancer*, vol. 12, no. 16, p. 5005, 2021, doi: 10.7150/JCA.58762.

[35] B. Sandfeld-Paulsen *et al.*, “Exosomal Proteins as Diagnostic Biomarkers in Lung Cancer,” *Journal of Thoracic Oncology*, vol. 11, no. 10, pp. 1701–1710, Oct. 2016, doi: 10.1016/J.JTHO.2016.05.034.

[36] B. N. Hannafon *et al.*, “Plasma exosome microRNAs are indicative of breast cancer,” *Breast Cancer Research*, vol. 18, no. 1, pp. 1–14, Sep. 2016, doi: 10.1186/S13058-016-0753-X/FIGURES/6.

[37] S. Yan *et al.*, “Downregulation of circulating exosomal miR-638 predicts poor prognosis in colon cancer patients,” *Oncotarget*, vol. 8, no. 42, p. 72220, Sep. 2017, doi: 10.18632/ONCOTARGET.19689.

[38] T. Yang *et al.*, “Exosome delivered anticancer drugs across the blood-brain barrier for brain cancer therapy in Danio Rerio,” *Pharm Res*, vol. 32, no. 6, pp. 2003–2014, Jun. 2015, doi: 10.1007/S11095-014-1593-Y/METRICS.

[39] W. M. Pardridge, “Drug transport across the blood-brain barrier,” *Journal of Cerebral Blood Flow and Metabolism*, vol. 32, no. 11, pp. 1959–1972, Nov. 2012, doi: 10.1038/JCBFM.2012.126/ASSET/IMAGES/LARGE/10.1038_JCBFM.2012.126-FIG7.JPEG.

[40] J. G. Van Den Boorn, M. Schlee, C. Coch, and G. Hartmann, “SiRNA delivery with exosome nanoparticles,” *Nature Biotechnology 2011 29:4*, vol. 29, no. 4, pp. 325–326, Apr. 2011, doi: 10.1038/nbt.1830.

[41] M. C. Didiot *et al.*, “Exosome-mediated delivery of hydrophobically modified siRNA for huntingtin mRNA silencing,” *Molecular Therapy*, vol. 24, no. 10, pp. 1836–1847, Oct. 2016, doi: 10.1038/mt.2016.126.

[42] R. Kalluri and V. S. LeBleu, “The biology, function, and biomedical applications of exosomes,” *Science (1979)*, vol. 367, no. 6478, Feb. 2020, doi:

10.1126/SCIENCE.AAU6977/ASSET/F5050DD7-9124-4A75-9FBE-2BCDF3F27CD8/ASSETS/GRAPHIC/367_AAU6977_F6.JPEG.

[43] S. Lin *et al.*, “Progress in microfluidics-based exosome separation and detection technologies for diagnostic applications,” *Small*, vol. 16, no. 9, p. 1903916, Mar. 2020, doi: 10.1002/smll.201903916.

[44] M. L. Alvarez, M. Khosroheidari, R. Kanchi Ravi, and J. K. Distefano, “Comparison of protein, microRNA, and mRNA yields using different methods of urinary exosome isolation for the discovery of kidney disease biomarkers,” *Kidney Int*, vol. 82, no. 9, pp. 1024–1032, Nov. 2012, doi: 10.1038/KI.2012.256.

[45] C. Coughlan *et al.*, “Exosome Isolation by Ultracentrifugation and Precipitation: A Comparison of Techniques for Downstream Analyses,” *Curr Protoc Cell Biol*, vol. 88, no. 1, p. e110, Sep. 2020, doi: 10.1002/CPCB.110.

[46] M. Zhang *et al.*, “Methods and Technologies for Exosome Isolation and Characterization,” *Small Methods*, vol. 2, no. 9, p. 1800021, Sep. 2018, doi: 10.1002/SMTD.201800021.

[47] D. K. Jeppesen *et al.*, “Comparative analysis of discrete exosome fractions obtained by differential centrifugation,” *J Extracell Vesicles*, vol. 3, no. 1, 2014, doi: 10.3402/JEV.V3.25011.

[48] C. Théry, S. Amigorena, G. Raposo, and A. Clayton, “Isolation and characterization of exosomes from cell culture supernatants and biological fluids,” *Curr Protoc Cell Biol*, vol. Chapter 3, no. 1, Mar. 2006, doi: 10.1002/0471143030.CB0322S30.

[49] S. Gupta *et al.*, “An improvised one-step sucrose cushion ultracentrifugation method for exosome isolation from culture supernatants of mesenchymal stem cells,” *Stem*

Cell Res Ther, vol. 9, no. 1, pp. 1–11, Jul. 2018, doi: 10.1186/S13287-018-0923-0/FIGURES/6.

[50] J. Liu *et al.*, “Extracellular Vesicles in Liquid Biopsies: Potential for Disease Diagnosis,” *Biomed Res Int*, vol. 2021, 2021, doi: 10.1155/2021/6611244.

[51] P. Li, M. Kaslan, S. H. Lee, J. Yao, and Z. Gao, “Progress in Exosome Isolation Techniques,” *Theranostics*, vol. 7, no. 3, p. 789, 2017, doi: 10.7150/THNO.18133.

[52] L. He, D. Zhu, J. Wang, and X. Wu, “A highly efficient method for isolating urinary exosomes,” *Int J Mol Med*, vol. 43, no. 1, pp. 83–90, Jan. 2019, doi: 10.3892/IJMM.2018.3944/HTML.

[53] Y. Yang *et al.*, “Extracellular vesicles isolated by size-exclusion chromatography present suitability for RNomics analysis in plasma,” *J Transl Med*, vol. 19, no. 1, pp. 1–12, Dec. 2021, doi: 10.1186/S12967-021-02775-9/FIGURES/6.

[54] L. Filipović *et al.*, “Affinity-based isolation of extracellular vesicles by means of single-domain antibodies bound to macroporous methacrylate-based copolymer,” *N Biotechnol*, vol. 69, pp. 36–48, Jul. 2022, doi: 10.1016/J.NBT.2022.03.001.

[55] J. H. Byun *et al.*, “Isolation of Small Extracellular Vesicles From Human Serum Using a Combination of Ultracentrifugation With Polymer-Based Precipitation,” *Ann Lab Med*, vol. 40, no. 3, pp. 253–258, Dec. 2019, doi: 10.3343/ALM.2020.40.3.253.

[56] T. S. Martins, J. Catita, I. M. Rosa, O. A. B. Da Cruz e Silva, and A. G. Henriques, “Exosome isolation from distinct biofluids using precipitation and column-based approaches,” *PLoS One*, vol. 13, no. 6, p. e0198820, Jun. 2018, doi: 10.1371/JOURNAL.PONE.0198820.

[57] M. A. Di Bella, “Overview and Update on Extracellular Vesicles: Considerations on Exosomes and Their Application in Modern Medicine,” *Biology (Basel)*, vol. 11, no. 6, Jun. 2022, doi: 10.3390/BIOLOGY11060804.

[58] F. Gao *et al.*, “A novel strategy for facile serum exosome isolation based on specific interactions between phospholipid bilayers and TiO2,” *Chem Sci*, vol. 10, no. 6, p. 1579, Feb. 2019, doi: 10.1039/C8SC04197K.

[59] N. Zhang, N. Sun, and C. Deng, “Rapid isolation and proteome analysis of urinary exosome based on double interactions of Fe3O4@ TiO2-DNA aptamer,” *Talanta*, vol. 221, p. 121571, 2021.

[60] X. Xiang *et al.*, “A new urinary exosome enrichment method by a combination of ultrafiltration and TiO2nanoparticles,” *Analytical Methods*, vol. 13, no. 13, pp. 1591–1600, 2021, doi: 10.1039/d1ay00102g.

[61] Y. Pang, J. Shi, X. Yang, C. Wang, Z. Sun, and R. Xiao, “Personalized detection of circling exosomal PD-L1 based on Fe3O4@TiO2 isolation and SERS immunoassay,” *Biosens Bioelectron*, vol. 148, no. July 2019, p. 111800, 2020, doi: 10.1016/j.bios.2019.111800.

[62] N. Zhang, X. Hu, H. Chen, C. Deng, and N. Sun, “Specific enrichment and glycosylation discrepancy profiling of cellular exosomes using a dual-affinity probe,” *Chemical Communications*, vol. 57, no. 51, pp. 6249–6252, 2021.

[63] D. Lou, Y. Wang, Q. Yang, L. Hu, and Q. Zhu, “Ultrafiltration combing with phospholipid affinity-based isolation for metabolomic profiling of urinary extracellular vesicles,” *J Chromatogr A*, vol. 1640, Mar. 2021, doi: 10.1016/J.CHROMA.2021.461942.

[64] T. Yasui *et al.*, “Unveiling massive numbers of cancer-related urinary-microRNA candidates via nanowires,” *Sci Adv*, vol. 3, no. 12, Dec. 2017, doi: 10.1126/SCIADV.1701133/SUPPL_FILE/1701133_SM.PDF.

[65] M. Li, E. Zeringer, T. Barta, J. Schageman, A. Cheng, and A. V. Vlassov, “Analysis of the RNA content of the exosomes derived from blood serum and urine and its potential as biomarkers,” *Philosophical Transactions of the Royal Society B: Biological Sciences*, vol. 369, no. 1652, Sep. 2014, doi: 10.1098/RSTB.2013.0502.

[66] F. Gao *et al.*, “A novel strategy for facile serum exosome isolation based on specific interactions between phospholipid bilayers and TiO 2,” *Chem Sci*, vol. 10, no. 6, pp. 1579–1588, Feb. 2019, doi: 10.1039/C8SC04197K.

[67] J. Li, X. He, Y. Deng, and C. Yang, “An Update on Isolation Methods for Proteomic Studies of Extracellular Vesicles in Biofluids,” *Molecules*, vol. 24, no. 19, Sep. 2019, doi: 10.3390/MOLECULES24193516.

[68] S. Lin *et al.*, “Progress in Microfluidics-Based Exosome Separation and Detection Technologies for Diagnostic Applications,” *Small*, vol. 16, no. 9, p. 1903916, Mar. 2020, doi: 10.1002/SMLL.201903916.

[69] Y. F. Lee, K. Y. Lien, H. Y. Lei, and G. Bin Lee, “An integrated microfluidic system for rapid diagnosis of dengue virus infection,” *Biosens Bioelectron*, vol. 25, no. 4, pp. 745–752, Dec. 2009, doi: 10.1016/J.BIOS.2009.08.020.

[70] F. Jiang *et al.*, “Solvent extraction of Cu(II) from sulfate solutions containing Zn(II) and Fe(III) using an interdigital micromixer,” *Hydrometallurgy*, vol. 177, pp. 116–122, May 2018, doi: 10.1016/J.HYDROMET.2018.03.004.

[71] J. Wang, P. Ma, D. H. Kim, B. F. Liu, and U. Demirci, "Towards microfluidic-based exosome isolation and detection for tumor therapy," *Nano Today*, vol. 37, p. 101066, Apr. 2021, doi: 10.1016/J.NANTOD.2020.101066.

[72] A. Liga, A. D. B. Vliegenthart, W. Oosthuyzen, J. W. Dear, and M. Kersaudy-Kerhoas, "Exosome isolation: a microfluidic road-map," *Lab Chip*, vol. 15, no. 11, pp. 2388–2394, Jun. 2015, doi: 10.1039/C5LC00240K.

[73] M. Bayareh, M. N. Ashani, and A. Usefian, "Active and passive micromixers: A comprehensive review," *Chemical Engineering and Processing - Process Intensification*, vol. 147, p. 107771, Jan. 2020, doi: 10.1016/J.CEP.2019.107771.

[74] X. Niu and Y. K. Lee, "Efficient spatial-temporal chaotic mixing in microchannels," *Journal of Micromechanics and Microengineering*, vol. 13, no. 3, p. 454, Apr. 2003, doi: 10.1088/0960-1317/13/3/316.

[75] T. D. Luong, V. N. Phan, and N. T. Nguyen, "High-throughput micromixers based on acoustic streaming induced by surface acoustic wave," *Microfluid Nanofluidics*, vol. 10, no. 3, pp. 619–625, Mar. 2011, doi: 10.1007/S10404-010-0694-0/FIGURES/8.

[76] A. A. Deshmukh, D. Liepmann, A. P. Pisano, B. Sensor, and A. Center, "CONTINUOUS MICROMIXER WITH PULSATILE MICROPUMPS," 2000, doi: 10.31438/trf.hh2000.18.

[77] X. Niu and Y. K. Lee, "Efficient spatial-temporal chaotic mixing in microchannels," *Journal of Micromechanics and Microengineering*, vol. 13, no. 3, p. 454, Apr. 2003, doi: 10.1088/0960-1317/13/3/316.

[78] J. J. Huang, Y. J. Lo, C. M. Hsieh, U. Lei, C. I. Li, and C. W. Huang, “An electro-thermal micro mixer,” *NEMS 2011 - 6th IEEE International Conference on Nano/Micro Engineered and Molecular Systems*, pp. 919–922, 2011, doi: 10.1109/NEMS.2011.6017503.

[79] D. Nouri, A. Zabihi-Hesari, and M. Passandideh-Fard, “Rapid mixing in micromixers using magnetic field,” *Sens Actuators A Phys*, vol. 255, pp. 79–86, Mar. 2017, doi: 10.1016/J.SNA.2017.01.005.

[80] H. Tan, “Numerical study of a bubble driven micromixer based on thermal inkjet technology,” *Physics of Fluids*, vol. 31, no. 6, p. 62006, Jun. 2019, doi: 10.1063/1.5098449/982079.

[81] L. Capretto, W. Cheng, M. Hill, and X. Zhang, “Micromixing within microfluidic devices,” *Top Curr Chem*, vol. 304, pp. 27–68, 2011, doi: 10.1007/128_2011_150/FIGURES/20_150.

[82] W. Raza, S. Hossain, and K.-Y. Kim, “A Review of Passive Micromixers with a Comparative Analysis,” *Micromachines (Basel)*, vol. 11, no. 5, p. 455, Apr. 2020, doi: 10.3390/mi11050455.

[83] J. Branebjerg, P. Gravesen, J. P. Krog, and C. R. Nielsen, “Fast mixing by lamination,” *Proceedings of the IEEE Micro Electro Mechanical Systems (MEMS)*, pp. 441–446, 1996, doi: 10.1109/MEMSYS.1996.494022.

[84] H. Sadabadi, M. Packirisamy, and R. Wüthrich, “High performance cascaded PDMS micromixer based on split-and-recombination flows for lab-on-a-chip applications,” *RSC Adv*, vol. 3, no. 20, pp. 7296–7305, Apr. 2013, doi: 10.1039/C3RA40910D.

[85] T. W. Lim *et al.*, “Three-dimensionally crossing manifold micro-mixer for fast mixing in a short channel length,” *Lab Chip*, vol. 11, no. 1, pp. 100–103, Dec. 2010, doi: 10.1039/C005325M.

[86] X. Li, H. Chang, X. Liu, F. Ye, and W. Yuan, “A 3-D Overbridge-Shaped Micromixer for Fast Mixing Over a Wide Range of Reynolds Numbers,” *Journal of Microelectromechanical Systems*, vol. 24, no. 5, pp. 1391–1399, Oct. 2015, doi: 10.1109/JMEMS.2015.2403472.

[87] J. Yang, L. Qi, Y. Chen, and H. Ma, “Design and Fabrication of a Three Dimensional Spiral Micromixer,” *Chin J Chem*, vol. 31, no. 2, pp. 209–214, Feb. 2013, doi: 10.1002/CJOC.201200922.

[88] K. Liu *et al.*, “Design and analysis of the cross-linked dual helical micromixer for rapid mixing at low Reynolds numbers,” *Microfluid Nanofluidics*, vol. 19, no. 1, pp. 169–180, Jul. 2015, doi: 10.1007/S10404-015-1558-4/FIGURES/12.

[89] A. D. Stroock, S. K. W. Dertinger, A. Ajdari, I. Mezić, H. A. Stone, and G. M. Whitesides, “Chaotic mixer for microchannels,” *Science (1979)*, vol. 295, no. 5555, pp. 647–651, Jan. 2002, doi: 10.1126/SCIENCE.1066238/ASSET/D19F07E3-2F46-45C0-B700-FD95192A2FB9/ASSETS/GRAPHIC/SE0320138004.JPEG.

[90] P. B. Howell *et al.*, “A microfluidic mixer with grooves placed on the top and bottom of the channel,” *Lab Chip*, vol. 5, no. 5, pp. 524–530, Apr. 2005, doi: 10.1039/B418243J.

[91] M. Sadegh Cheri, H. Latifi, M. Salehi Moghaddam, and H. Shahraki, “Simulation and experimental investigation of planar micromixers with short-mixing-length,”

Chemical Engineering Journal, vol. 234, pp. 247–255, Dec. 2013, doi: 10.1016/J.CEJ.2013.08.067.

[92] A. Alam, A. Afzal, and K. Y. Kim, “Mixing performance of a planar micromixer with circular obstructions in a curved microchannel,” *Chemical Engineering Research and Design*, vol. 92, no. 3, pp. 423–434, Mar. 2014, doi: 10.1016/J.CHERD.2013.09.008.

[93] M. A. Ansari, K. Y. Kim, K. Anwar, and S. M. Kim, “A novel passive micromixer based on unbalanced splits and collisions of fluid streams,” *Journal of Micromechanics and Microengineering*, vol. 20, no. 5, p. 055007, Apr. 2010, doi: 10.1088/0960-1317/20/5/055007.

[94] W. Raza and K. Y. Kim, “Asymmetrical Split-and-Recombine Micromixer with Baffles,” *Micromachines (Basel)*, vol. 10, no. 12, Dec. 2019, doi: 10.3390/MI10120844.

[95] F. Schönfeld and S. Hardt, “Simulation of helical flows in microchannels,” *AIChE Journal*, vol. 50, no. 4, pp. 771–778, Apr. 2004, doi: 10.1002/AIC.10071.

[96] T. S. Sheu, S. J. Chen, and J. J. Chen, “Mixing of a split and recombine micromixer with tapered curved microchannels,” *Chem Eng Sci*, vol. 71, pp. 321–332, Mar. 2012, doi: 10.1016/J.CES.2011.12.042.

[97] A. Afzal and K. Y. Kim, “Convergent–divergent micromixer coupled with pulsatile flow,” *Sens Actuators B Chem*, vol. 211, pp. 198–205, May 2015, doi: 10.1016/J.SNB.2015.01.062.

[98] C. Y. Wu and R. T. Tsai, “Fluid mixing via multidirectional vortices in converging–diverging meandering microchannels with semi-elliptical side walls,” *Chemical*

Engineering Journal, vol. 217, pp. 320–328, Feb. 2013, doi: 10.1016/J.CEJ.2012.12.016.

[99] L. Alvarez-Erviti, Y. Seow, H. Yin, C. Betts, S. Lakhal, and M. J. A. Wood, "Delivery of siRNA to the mouse brain by systemic injection of targeted exosomes," *Nature Biotechnology 2011 29:4*, vol. 29, no. 4, pp. 341–345, Mar. 2011, doi: 10.1038/nbt.1807.

[100] B. J. Tauro *et al.*, "Comparison of ultracentrifugation, density gradient separation, and immunoaffinity capture methods for isolating human colon cancer cell line LIM1863-derived exosomes," *Methods*, vol. 56, no. 2, pp. 293–304, Feb. 2012, doi: 10.1016/J.YMETH.2012.01.002.

[101] H. Kalra *et al.*, "Comparative proteomics evaluation of plasma exosome isolation techniques and assessment of the stability of exosomes in normal human blood plasma," *Proteomics*, vol. 13, no. 22, pp. 3354–3364, Nov. 2013, doi: 10.1002/PMIC.201300282.

[102] M. Logozzi *et al.*, "Plasmatic Exosome Number and Size Distinguish Prostate Cancer Patients From Healthy Individuals: A Prospective Clinical Study," *Front Oncol*, vol. 11, p. 727317, Oct. 2021, doi: 10.3389/FONC.2021.727317/BIBTEX.

[103] W. Zhang *et al.*, "Characterization of exosomes derived from ovarian cancer cells and normal ovarian epithelial cells by nanoparticle tracking analysis," *Tumor Biology*, vol. 37, no. 3, pp. 4213–4221, Mar. 2016, doi: 10.1007/S13277-015-4105-8/METRICS.

[104] A. Zlotogorski-Hurvitz, D. Dayan, G. Chaushu, T. Salo, and M. Vered, "Morphological and molecular features of oral fluid-derived exosomes: oral cancer

patients versus healthy individuals," *J Cancer Res Clin Oncol*, vol. 142, no. 1, pp. 101–110, Jan. 2016, doi: 10.1007/S00432-015-2005-3/METRICS.

[105] D. D. Taylor, W. Zacharias, and C. Gercel-Taylor, "Exosome isolation for proteomic analyses and RNA profiling," *Methods Mol Biol*, vol. 728, pp. 235–246, 2011, doi: 10.1007/978-1-61779-068-3_15.

[106] S. Rani *et al.*, "Isolation of exosomes for subsequent mRNA, MicroRNA, and protein profiling," *Methods Mol Biol*, vol. 784, pp. 181–195, 2011, doi: 10.1007/978-1-61779-289-2_13.

[107] F. K. Alanazi, D. R. Lu, F. Shakeel, and N. Haq, "Density gradient separation of carborane-containing liposome from low density lipoprotein and detection by inductively coupled plasma spectrometry," *http://dx.doi.org/10.3109/08982104.2013.833224*, vol. 24, no. 1, pp. 53–58, Mar. 2014, doi: 10.3109/08982104.2013.833224.

[108] A. R. Beaudoin and G. Grondin, "Shedding of vesicular material from the cell surface of eukaryotic cells: different cellular phenomena," *Biochimica et Biophysica Acta (BBA) - Reviews on Biomembranes*, vol. 1071, no. 3, pp. 203–219, Nov. 1991, doi: 10.1016/0304-4157(91)90014-N.

[109] F. Wang and J. Liu, "A Stable Lipid/TiO2 Interface with Headgroup-Inversed Phosphocholine and a Comparison with SiO2," *J Am Chem Soc*, vol. 137, no. 36, pp. 11736–11742, Sep. 2015, doi: 10.1021/JACS.5B06642.

[110] Y. Liu, "Interfacing Liposomes with Metal Ions and Metal Oxides: Coordination Chemistry, Surface Forces and Membrane Integrity," Aug. 2020, Accessed: Aug. 16, 2023. [Online]. Available: https://uwspace.uwaterloo.ca/handle/10012/16256

[111] F. Wang and J. Liu, "Liposome supported metal oxide nanoparticles: interaction mechanism, light controlled content release, and intracellular delivery," *Small*, vol. 10, no. 19, pp. 3927–3931, Oct. 2014, doi: 10.1002/SMLL.201400850.

[112] R. E. Lane, D. Korbie, W. Anderson, R. Vaidyanathan, and M. Trau, "Analysis of exosome purification methods using a model liposome system and tunable-resistive pulse sensing," *Scientific Reports 2015 5:1*, vol. 5, no. 1, pp. 1–7, Jan. 2015, doi: 10.1038/srep07639.

[113] N. T. Nguyen, M. Hejazian, C. H. Ooi, and N. Kashaninejad, "Recent Advances and Future Perspectives on Microfluidic Liquid Handling," *Micromachines 2017, Vol. 8, Page 186*, vol. 8, no. 6, p. 186, Jun. 2017, doi: 10.3390/MI8060186.

[114] C. D. O'Connell *et al.*, "Development of the Biopen: A handheld device for surgical printing of adipose stem cells at a chondral wound site," *Biofabrication*, vol. 8, no. 1, 2016, doi: 10.1088/1758-5090/8/1/015019.

[115] A. Al-Halhouli, A. Alshare, M. Mohsen, M. Matar, A. Dietzel, and S. Büttgenbach, "Passive Micromixers with Interlocking Semi-Circle and Omega-Shaped Modules: Experiments and Simulations," *Micromachines 2015, Vol. 6, Pages 953-968*, vol. 6, no. 7, pp. 953–968, Jul. 2015, doi: 10.3390/MI6070953.

[116] K. Karthikeyan and L. Sujatha, "Study of Permissible Flow Rate and Mixing Efficiency of the Micromixer Devices," *International Journal of Chemical Reactor Engineering*, vol. 17, no. 1, pp. 1–15, Jan. 2019, doi: 10.1515/ijcre-2018-0047.

[117] Y.-J. Yang, "Experimental and Modeling Studies of Colloidal Suspension Stability of High-Density Particles in Aqueous Solutions," 2016.

[118] M. P. Proenca, C. T. Sousa, J. Ventura, and J. P. Araújo, “Electrochemical synthesis and magnetism of magnetic nanotubes,” *Magnetic Nano- and Microwires: Design, Synthesis, Properties and Applications*, pp. 727–781, May 2015, doi: 10.1016/B978-0-08-100164-6.00024-2.

[119] J. Stetefeld, S. A. McKenna, and T. R. Patel, “Dynamic light scattering: a practical guide and applications in biomedical sciences,” *Biophys Rev*, vol. 8, no. 4, pp. 409–427, Dec. 2016, doi: 10.1007/S12551-016-0218-6/FIGURES/1.

[120] “Dynamic Light Scattering DLS | Malvern Panalytical.” Accessed: Oct. 06, 2023. [Online]. Available: https://www.malvernpanalytical.com/en/products/technology/light-scattering/dynamic-light-scattering

[121] S. A. Markarian, L. R. Harutyunyan, and R. S. Harutyunyan, “The properties of mixtures of sodium dodecylsulfate and diethylsulfoxide in water,” *J Solution Chem*, vol. 34, no. 3, pp. 361–368, Mar. 2005, doi: 10.1007/S10953-005-3056-X/METRICS.

[122] S. Bhattacharjee, “DLS and zeta potential - What they are and what they are not?,” *J Control Release*, vol. 235, pp. 337–351, Aug. 2016, doi: 10.1016/J.JCONREL.2016.06.017.

[123] H. Zhou, C. C. Mayorga-Martinez, and M. Pumera, “Microplastic Removal and Degradation by Mussel-Inspired Adhesive Magnetic/Enzymatic Microrobots,” *Small Methods*, vol. 5, no. 9, p. 2100230, Sep. 2021, doi: 10.1002/SMTD.202100230.

[124] R. Vogel *et al.*, “High-Resolution Single Particle Zeta Potential Characterisation of Biological Nanoparticles using Tunable Resistive Pulse Sensing,” *Sci Rep*, vol. 7, no. 1, Dec. 2017, doi: 10.1038/S41598-017-14981-X.

[125] K. P. De Jong, A. J. Koster, A. H. Janssen, and U. Ziese, “Electron tomography of molecular sieves,” *Stud Surf Sci Catal*, vol. 157, pp. 225–242, 2005, doi: 10.1016/s0167-2991(05)80013-8.

[126] M. Li, E. Zeringer, T. Barta, J. Schageman, A. Cheng, and A. V. Vlassov, “Analysis of the RNA content of the exosomes derived from blood serum and urine and its potential as biomarkers,” *Philosophical Transactions of the Royal Society B: Biological Sciences*, vol. 369, no. 1652, 2014, doi: 10.1098/RSTB.2013.0502.

[127] I. M. Saadeldin, W. A. Khalil, M. G. Alharbi, and S. H. Lee, “The Current Trends in Using Nanoparticles, Liposomes, and Exosomes for Semen Cryopreservation,” *Animals 2020, Vol. 10, Page 2281*, vol. 10, no. 12, p. 2281, Dec. 2020, doi: 10.3390/ANI10122281.

[128] S. Boukouris and S. Mathivanan, “Exosomes in bodily fluids are a highly stable resource of disease biomarkers,” *Proteomics Clin Appl*, vol. 9, no. 3–4, p. 358, Apr. 2015, doi: 10.1002/PRCA.201400114.

[129] Z. Brownlee, K. D. Lynn, P. E. Thorpe, and A. J. Schroit, “A novel ‘salting-out’ procedure for the isolation of tumor-derived exosomes,” *J Immunol Methods*, vol. 407, pp. 120–126, May 2014, doi: 10.1016/J.JIM.2014.04.003.

[130] J. Chen *et al.*, “Review on Strategies and Technologies for Exosome Isolation and Purification,” *Front Bioeng Biotechnol*, vol. 9, p. 811971, Jan. 2022, doi: 10.3389/FBIOE.2021.811971/BIBTEX.

[131] T. E. Thingholm, T. J. D. Jørgensen, O. N. Jensen, and M. R. Larsen, “Highly selective enrichment of phosphorylated peptides using titanium dioxide,” *Nat Protoc*, vol. 1, no. 4, pp. 1929–1935, Nov. 2006, doi: 10.1038/NPROT.2006.185.

[132] L. Alvarez-Erviti, Y. Seow, H. Yin, C. Betts, S. Lakhal, and M. J. A. Wood, “Delivery of siRNA to the mouse brain by systemic injection of targeted exosomes,” *Nature Biotechnology 2011 29:4*, vol. 29, no. 4, pp. 341–345, Mar. 2011, doi: 10.1038/nbt.1807.

[133] R. E. Lane, D. Korbie, W. Anderson, R. Vaidyanathan, and M. Trau, “Analysis of exosome purification methods using a model liposome system and tunable-resistive pulse sensing,” *Sci Rep*, vol. 5, pp. 1–7, 2015, doi: 10.1038/srep07639.